

FOR REFERENCE ONLY

NOTTINGHAM[®]
TRENT UNIVERSITY

**Libraries and Learning Resources
SHORT LOAN COLLECTION**

Date	Time	Date	Time
20 AUG 2007	Ref 6.55pm		

Please return this item to the issuing library.
Fines are payable for late return.

THIS ITEM MAY NOT BE RENEWED

Short Loan 06

40 0706375 8



ProQuest Number: 10290308

All rights reserved

INFORMATION TO ALL USERS

The quality of this reproduction is dependent upon the quality of the copy submitted.

In the unlikely event that the author did not send a complete manuscript and there are missing pages, these will be noted. Also, if material had to be removed, a note will indicate the deletion.



ProQuest 10290308

Published by ProQuest LLC (2017). Copyright of the Dissertation is held by the Author.

All rights reserved.

This work is protected against unauthorized copying under Title 17, United States Code
Microform Edition © ProQuest LLC.

ProQuest LLC.
789 East Eisenhower Parkway
P.O. Box 1346
Ann Arbor, MI 48106 – 1346

**ENHANCEMENT OF THE LIGHT OUTCOUPLING OF
ALTERNATING CURRENT Laterally Emitting
Thin Film Electroluminescent Devices**

SARA OTERO BARROS

A thesis submitted in partial fulfilment of the requirements of
The Nottingham Trent University for the degree of doctor of
philosophy

July 2000

ABSTRACT

Brightness enhancement of Laterally Emitting Thin Film Electroluminescent (LETFL) devices is essential for polychrome display applications. Brightness values can be increased by improvement of the outcoupling efficiency. This thesis presents work carried out towards the analysis and development of the outcoupling mechanism integrated within LETFL devices. Special importance is given to the enhancement of the coupling efficiency for head mounted displays (HMD) and electrophotographic printing (EP) applications for which high brightness and narrow angular profiles are advantageous.

This research introduces a theoretical study of the light transmission within a LETFL device, based on the modal propagation theory in an optical waveguide. Losses due to surface roughness were determined and compared with previously published experimental results. Agreement between the fundamental mode attenuation loss, theoretically calculated, and the total attenuation loss, experimentally determined, demonstrated transmission is principally supported by the fundamental mode.

Based upon this result, modelling of the outcoupling efficiency in conventional devices was performed assuming outcoupling was due to surface roughness and bend radiation losses. Low outcoupling efficiency values, of the order of 4% of the generated light, were obtained. This, in addition to the inadequate broad angular profiles experimentally determined, demonstrated need for improvement.

The presented work has concentrated on the proposal of two novel outcoupling mechanisms: the surface emitting edge emitter and the etched aperture. Initial modelling of the emitted angular distribution demonstrates a Gaussian angular profile, with a characteristic width of 24° .

The feasibility of fabrication of these structures using ion milling was additionally proved. Initially, a study was undertaken of the ion milling properties of LETFL devices and associated materials. The principal parameters considered were the etching time, the acceleration voltage and the angle of incidence of the ion beam. Subsequently the fabrication and determination of the light output properties of full devices demonstrated a $\sim 2\times$ and $\sim 4\times$ enhancement of the light intensity for the etched and surface emitting edge emitter devices respectively. Additionally, the angular profile of etched devices was observed to redistribute towards narrower angles of view which introduces further enhancement of the coupling efficiency, by 12% and 5% for HMD and EP respectively. The angular distribution of surface emitting edge emitter LETFL devices was found to be in agreement with the theoretical results.

ACKNOWLEDGEMENTS

Throughout my doctoral study I have received support and assistance from multiple sources.

I am especially grateful to Professor C B Thomas for giving me the opportunity to undertake this PhD and for his genuine interest in the research involved.

Thanks are equally given to Dr R Stevens and Dr W M Cranton who supervised this thesis, for their helpful discussions, guidance and assistance in preparation of papers.

I wish to thank Dr Christos Mias for his invaluable suggestions and contributions, especially in the theoretical studies.

My special gratitude to Professor C Gomez-Reino who introduced me to research, encouraged me to undertake these studies and demonstrated constant support.

I would also like to thank G Thomas and colleagues at the Rutherford and Appleton Laboratories, Oxfordshire, UK, for the use of the ion beam milling equipment and metrology systems.

Special thanks are given to M Craven who has shown a sincere interest in my work and to which he contributed in many ways. His efficient and continuous technical help were invaluable. I also wish to thank Dr C Tsakonas and Dr R Ranson for assisting in the growth of the thin films and for the technical discussions.

Thanks are also given to all my colleagues within the Display Group for their assistance and friendly help. Special gratitude is given to Demos for his frank comments which helped the development of this work. Thanks Alan for cheering up our days with your puzzling comments!

I wish to especially thank my friend Nariman for the unforgettable times we shared. I would also like to thank all my friends, especially Phooi San for the endless talks and Sunita who taught me "work is over after 5 o'clock".

Finally my greatest gratitude goes to my family for their unconditional support.

LIST OF PUBLICATIONS

1. S O Barros, C Mias C B Thomas and R Stevens, "A Comparison of the Outcoupling Characteristics of Laterally Emitting Thin Film Electroluminescent Devices", *accepted for publication in Semiconductor Science and Technology*
2. S O Barros, R Stevens and W Cranton, "Enhancement of the LETFEL device optical outcoupling via the fabrication of novel geometry structures", *accepted for publication in Optical Engineering SPIE Journal*
3. Sara Barros, "Ion Milling of Laterally Emitting Thin Film Electroluminescent (LETFEL) Devices", *Proceedings of PREP '99 Conference, Manchester, 1999*
4. W M Cranton, C B Thomas, R Stevens, M R Craven, S O Barros, E A Mastio and P S Theng, "Laterally Emitting Thin Film Electroluminescence for Head Mounted Displays", *Proceedings of the Electronic Information Displays Conference, London, 1997*
5. S O Barros, R Stevens and W M Cranton, "Enhancement of the LETFEL Device Optical Outcoupling via the Fabrication of Novel Geometry Structures", *Proceedings of the SPIE Conference, "Flat Panel Display Technologies II", S. Jose 2000, USA*

CONTENTS

Abstract	ii
Acknowledgements	iii
List of Publications	iv
Contents	v
List of Figures	x
List of Tables	xiv
List of Abbreviations	xv
List of Variables	xvii

CHAPTER 1

INTRODUCTION	1
1.1 OVERVIEW OF THE DISPLAY TECHNOLOGY	2
1.1.1 Emissive Displays	3
1.1.2 Non Emissive Displays	5
1.1.3 Display Technology Market Sector	8
1.2 REVIEW OF THE TFEL TECHNOLOGY	11
1.2.1 Brief History	11
1.2.2 The Structure and Electrical Characteristics of TFEL Devices	11
1.3 REVIEW OF THE LETFEL TECHNOLOGY	15
1.4 SUMMARY OF THESIS	18

CHAPTER 2		
THEORETICAL MODELLING OF LIGHT TRANSMISSION IN LETFEL DEVICES		20
2.1	INTRODUCTION	21
2.2	MAXWELL EQUATIONS	22
2.2.1	The Guided Modes	27
2.2.2	The Radiation Modes	31
2.3	SCATTERING LOSSES	32
2.3.1	Statistical Description of Random Roughness	33
2.3.2	Theoretical Study of the Mode Conversion from Guided to Radiation Modes due to Surface Roughness	35
 CHAPTER 3		
THEORETICAL MODELLING OF THE OUTCOUPLING PROCESS		40
3.1	INTRODUCTION	41
3.2	THE OUTCOUPLING MECHANISM OF CONVENTIONAL NON-ETCHED LETFEL DEVICES	42
3.2.1	The Effect of Surface Roughness on the Outcoupling Efficiency	43
3.2.2	The Effect of Bend Radiation Losses on the Outcoupling Efficiency	45
3.2.3	Conclusions: Limitations of the Conventional Non-Etched LETFEL Devices	50
3.3	OUTCOUPLING MECHANISM OF ABRUPT OPEN END LETFEL DEVICES	50
3.4	THEORETICAL MODELLING OF THE OUTCOUPLING THROUGH A SMOOTH ABRUPT OPEN END	53
3.5	CONCLUSIONS	60

CHAPTER 4		
EXPERIMENTAL DETAIL	61	
4.1	DEVICE FABRICATION AND CHARACTERISATION OVERVIEW	62
4.2	FABRICATION OF THE SiO₂ MICROSTRUCTURES	67
4.3	THIN FILM DEPOSITION	68
4.3.1	Magnetron Sputtering	68
4.3.2	DC Magnetron Sputtering	69
4.3.3	RF Magnetron Sputtering	70
4.3.4	Plasma Enhanced Chemical Vapour Deposition	72
4.4	THIN FILM PATTERNING	74
4.4.1	Thin Film Deposition	75
4.4.2	Photoresist Coating	75
4.4.3	Reactive Ion Etch	75
4.4.4	Photoresist Removal	77
4.5	SHAPING THE DEVICE APERTURE USING ION MILLING	78
4.5.1	Background	78
4.5.2	Equipment	78
4.6	DEVICE CHARACTERISATION	80
4.6.1	Measurement of the Light Intensity versus Voltage Characteristic	82
4.6.2	Angular Measurement System	83
4.6.3	Device Subjected to Test	84
4.7	CONCLUSIONS	85

CHAPTER 5		
ION MILLING CHARACTERISTICS OF LETFEL DEVICES AND ASSOCIATED MATERIALS		86
5.1	INTRODUCTION	87
5.2	THIN FILM PREPARATION	88
5.3	ION MILLING CHARACTERISTICS OF LETFEL MATERIALS	89
5.3.1	Ion Milling versus the Time	89
5.3.2	Ion Milling versus the Angle of Incidence	91
5.4	THE ION MILLED ZNS:MN WALL SIDE PROFILE	94
5.4.1	Experimental Ion Milled Profiles	95
5.4.2	Modelling of the Ion Milled Profiles	97
5.4.3	Comparison Between the Experimental and the Modelled Profiles	97
5.5	CONCLUSIONS	98
CHAPTER 6		
EXPERIMENTAL DETERMINATION OF THE LIGHT OUTPUT PROPERTIES OF LETFEL DEVICES		99
6.1	INTRODUCTION	100
6.2	EXPERIMENTAL DETERMINATION OF THE LIGHT OUTPUT PROPERTIES OF THE CONVENTIONAL NON-ETCHED LETFEL DEVICE	101
6.3	FABRICATION PARAMETERS AND EXPERIMENTAL DETERMINATION OF THE LIGHT OUTPUT PROPERTIES OF ETCHED LETFEL DEVICES	103
6.3.1	Fabrication Route	103
6.3.2	Study of the Light Output Properties	105

6.4	FABRICATION PARAMETERS AND EXPERIMENTAL DETERMINATION OF THE LIGHT OUTPUT PROPERTIES OF SURFACE EMITTING EDGE EMITTER LETFEL DEVICES	108
6.4.1	Fabrication Route	109
6.4.2	Study of the Light Output Properties	110
6.5	CONCLUSIONS: COMPARISON OF THE LIGHT OUTPUT PROPERTIES OF THE DIFFERENT OUTCOUPLING PROCESSES	113
CHAPTER 7		
	CONCLUSIONS AND FUTURE WORK	115
7.1	INTRODUCTION	116
7.1.1	Theoretical Modelling of the Outcoupling Mechanism	116
7.1.2	Fabrication of the Novel Outcoupling Mechanisms	117
7.2	ACHIEVEMENTS	118
7.3	FUTURE WORK	121
7.3.1	Development of Vertical Micromirrors	121
7.3.2	Development of Microlens Array	122
	REFERENCES	123

LIST OF FIGURES

FIGURE 1.1	EMISSIVE DISPLAYS	6
FIGURE 1.2	NON-EMISSIVE DISPLAYS	7
FIGURE 1.3	TYPICAL BV CHARACTERISTIC OF A TFEL DEVICE	12
FIGURE 1.4	PERFORMANCE MECHANISM OF HIGH-FIELD ELECTROLUMINESCENCE	14
FIGURE 1.5	CROSS SECTION OF A LETFEL DEVICE	16
FIGURE 1.6	COMPARISON OF A ACTFEL, EDGE EMITTER AND LETFEL STRUCTURE	17
FIGURE 2.1	TYPICAL LETFEL WAVEGUIDE	24
FIGURE 2.2	DIFFERENT PROPAGATION REGIMES WITHIN A WAVEGUIDE	26
FIGURE 2.3	GRAPHICAL REPRESENTATION OF THE CHARACTERISTIC EQUATION	28
FIGURE 2.4	TRANSVERSE PROFILE OF THE FOUR GUIDED MODES IN LETFEL WAVEGUIDES	30
FIGURE 2.5	SURFACE ROUGHNESS	33
FIGURE 2.6	POWER LOST IN A LETFEL DEVICE DUE TO SURFACE ROUGHNESS VERSUS PROPAGATION DISTANCE	38
FIGURE 3.1	CROSS SECTION OF A CONVENTIONAL NON-ETCHED LETFEL DEVICE	42
FIGURE 3.2	SEM PHOTOGRAPH ILLUSTRATING A TYPICAL CROSS SECTION OF A CONVENTIONAL NON-ETCHED LETFEL DEVICE	43

FIGURE 3.3	ATTENUATION OF THE FUNDAMENTAL MODE DUE TO SURFACE ROUGHNESS	45
FIGURE 3.4	WAVEGUIDE BEND	46
FIGURE 3.5	POWER ATTENUATION DUE TO BEND RADIATION LOSSES	49
FIGURE 3.6	ABRUPT OPEN END LAUNCHING GUIDED LIGHT TO THE OUTSIDE	51
FIGURE 3.7	ETCHED APERTURE	52
FIGURE 3.8	SURFACE EMITTING EDGE EMITTER	52
FIGURE 3.9	FUNDAMENTAL MODE TRANSVERSE PROFILE AND FITTING GAUSSIAN DISTRIBUTION	54
FIGURE 3.10	DFT OF THE TRANSVERSE PROFILE	56
FIGURE 3.11	OUTCOUPLED SPATIAL PROFILES AT DIFFERENT PROPAGATION LENGTHS	58
FIGURE 3.12	ANGULAR DIVERGENCE OF THE EMITTED LIGHT	59
FIGURE 4.1	FABRICATION ROUTE OF LETFEL DEVICES	64
FIGURE 4.2	DC MAGNETRON SPUTTERING SYSTEM	69
FIGURE 4.3	RF MAGNETRON SPUTTER DEPOSITION SYSTEM	71
FIGURE 4.4	PECVD SYSTEM UTILISED IN THE PRESENT RESEARCH	73
FIGURE 4.5	SYSTEM USED FOR THE RIE PROCESS	76
FIGURE 4.6	ION MILLING SYSTEM	79
FIGURE 4.7	LV MEASUREMENT SYSTEM	80
FIGURE 4.8	ANGULAR MEASUREMENT SYSTEM	82

FIGURE 4.9	ANGULAR MEASUREMENT SYSTEM BUILT FOR THE PRESENT RESEARCH	82
FIGURE 4.10	CALLIBRATION OF THE ANGULAR MEASUREMENT SYSTEM	83
FIGURE 4.11	TOP SURFACE OF A TEST SAMPLE	84
FIGURE 5.1	ION MILLING RATES VERSUS TIME OF THE THIN FILM MATERIALS INDICATED	90
FIGURE 5.2	ION MILLING RATES VERSUS THE ANGLE OF INCIDENCE AT 500 Volt	93
FIGURE 5.3	ION MILLING-RATE VERSUS THE ANGLE OF INCIDENCE AT AN ACCELERATION VOLTAGE OF 400 VOLTS AND A BEAM CURRENT OF 0.450MA/C ²	94
FIGURE 5.4	SIO ₂ MASK ON ZNS:MN THIN FILM BEFORE ION MILLING	95
FIGURE 5.5	COMPARISON AMONG FABRICATED AND SIMULATED ZNS:MN PROFILES ION MILLED AT THE FOLLOWING ANGLES OF INCIDENCE: A) 0° B) 10° C) 30° D) 50°	96
FIGURE 6.1	SEM ILLUSTRATION OF A CONVENTIONAL NON-ETCHED LETFEL DEVICE	102
FIGURE 6.2	LIGHT OUTPUT PROPERTIES OF CONVENTIONAL NON-ETCHED LETFEL DEVICES	102
FIGURE 6.3	SEM ILLUSTRATION OF AN ETCHED LETFEL DEVICE	106
FIGURE 6.4	LIGHT OUTPUT CHARACTERISTICS OF ETCHED LETFEL DEVICES	106
FIGURE 6.5	COMPARISON OF THE LV CHARACTERISTICS OF A CONVENTIONAL AND AN ANNEALED DEVICE USING ION MILLING	107

FIGURE 6.6	COMPARISON OF EXPERIMENTAL AND THEORETICAL ANGULAR PROFILES FOR AN ETCHED LETFEL DEVICE	108
FIGURE 6.7	SEM ILLUSTRATIONS OF LETFEL APERTURE CROSS SECTIONS ION MILLED AT DIFFERENT ANGLES OF INCIDENCE	110
FIGURE 6.8	SEM ILLUSTRATION OF A SURFACE EMITTING EDGE EMITTER LETFEL APERTURE	110
FIGURE 6.9	LIGHT OUTPUT CHARACTERISTICS OF SURFACE EMITTING EDGE EMITTER LETFEL DEVICES	111
FIGURE 6.10	COMPARISON OF THE ANGULAR DISTRIBUTION EXPERIMENTALLY MEASURED FROM A SURFACE EMITTING EDGE EMITTER AND THE THEORETICAL RESULTS OBTAINED FOR AN ABRUPT OPEN END	112
FIGURE 6.11	LIGHT OUTPUT PROPERTIES OF CONVENTIONAL, ETCHED AND SURFACE EMITTING EDGE EMITTER LETFEL DEVICES	113

LIST OF TABLES

TABLE 1.1	DISPLAY APPLICATIONS	10
TABLE 2.1	VALUES OF THE PROPAGATION CONSTANT, β , TRANSVERSE VECTOR, κ , AND EXTINCTION COEFFICIENT, γ , FOR LETFEL WAVEGUIDES	29
TABLE 4.1	AL AND TIW DEPOSITION AND ETCH RATES	71
TABLE 4.2	PECVD PROCESS PARAMETERS	74
TABLE 5.1	AVERAGED ION MILLING RATES OF LETFEL MATERIALS	92
TABLE 6.1	COUPLING EFFICIENCY INTO HMD AND EP APPLICATIONS EXPECTED FOR THE ANGULAR DISTRIBUTIONS MEASURED FROM VARIOUS OUTCOUPLING MECHANISMS	115

LIST OF ABBREVIATIONS

wt %	percentage weight
°C	Centigrade Degree
"	inches
3D	Three Dimensional
Å	Angstroms
a.u.	Arbitrary Units
AC	Alternating Current
ACTFEL	Alternating Current Thin Film Electroluminescent
Al	Aluminium
AMD	Active Matrix Display
AMLCD	Active Matrix Liquid Crystal Display
AMPD	Active Matrix Plasma Display
Ar	Argon
Au	Gold
cm	centimeter
CMF	Central Microstructure Facility
Cr	Chromium
CRT	Cathode Ray Tube
dB	Decibels
DC	Direct Current
DMD	Digital Micromirror Diode
dpi	dots per inch
EL	Electroluminescence
EP	Electrophotographic Printing
EPSRC	Engineering, Physics and Science Research Council
eV	Electron Volt
exp	exponential
FED	Field Emission Display
fL	Foot Lamberts
h	hours
HMD	Head Mounted Display
LCD	Liquid Crystal Display
LED	Light Emitting Diode

LETFEL	Laterally Emitting Thin Film Electroluminescent
lm	lumens
LV	Light Intensity versus Voltage
min	minutes
mm	millimeter
Mn	Manganese
NTU	Nottingham Trent University
O ₂	Oxygen
PDP	Plasma Display Panel
PECVD	Plasma Enhanced Chemically Vapor Deposited
RAL	Rutherford and Appleton Laboratories
RF	Radio Frequency
RIE	Reactive Ion Etch
rms	Root Mean Square
rpm	Revolutions per minute
ccm	standard cubic centimeter per minute
Si	Silicon
Si ₃ N ₄	Silicon Nitride
SiO ₂	Silicon Dioxide
ACTFEL	Alternating Current Thin Film Electroluminescent
TFT	Thin Film Transistor
TiW	Titanium Tungsten
Torr	Torricelli
TV	Television
UV	ultraviolet
V	Volts
VFD	Vacuum Fluorescent Display
Y ₂ O ₃	Yttrium Oxide
ZnS	Zinc Sulphide
ZnS:Mn	Zinc Sulphide Manganese
μm	micrometer

LIST OF VARIABLES

φ	phaseshift
θ_i	Incident Angle
θ_t	Transmitted Angle
τ	Angle
ω	Angular Frequency
B	Correlation Length
B	Magnetic Flux Density
$C(v,z)$	Amplitude of each continuum modes
$C_v(z)$	Amplitude of each guided mode
D	Electric Flux Density
d	Half Thickness of the Waveguide
∇	Del Operator
E	Electric Field
$E(\phi)$	Etch-Rate
$E(v,x)$	Radiation Modes
ϵ	Electric Permittivity
$E_v(x)$	Guided Modes
H	Magnetic Field
h	Waveguide Thickness
$h(z)$	Surface Height
k	Wavevector
L	Percentage of Power Lost
l	Propagation Length
n_{air}	Air Refractive Index
n_f	ZnS:Mn Refractive Index
n_j	Refractive Index
n_s	Y_2O_3 Refractive Index
P	Power

$p(h)$	Probability of Any Surface Point to be at a Height $h+\delta h$
β	Propagation Constant
r	Position vector
R	Radius
ρ	Radiation Mode Constant
Ψ	Scalar Amplitude
σ	standard deviation
t	refraction coefficient
t	Time
T	Transmittance
κ	Transverse Vector
V_R	Tangential Velocity before X_r
V_{R+X_r}	Tangential Velocity beyond X_r
x_0	Characteristic Width
X_r	Distance for which light velocity in a bend exceeds the light speed
ΔP	Power Lost
α	Attenuation Coefficient
α_{bend}	Attenuation Coefficient due to Waveguide Bend
α_{scatt}	Attenuation Coefficient due to Scattering
γ	Extinction Coefficient
μ	Magnetic Permittivity
σ_a	Intensity Coupled within an angle a
σ_t	Total Coupled Intensity
τ	Radiation Mode Constant
τ_a	Coupling Efficiency
ω_0	Angular Frequency in Vacuum

INTRODUCTION

-
- 1.1 Overview of the Display Technology
 - 1.2 Review of the ACTFEL Device Technology
 - 1.3 Review of the LETFEL Technology
 - 1.4 Summary of Thesis
-

1.1 OVERVIEW OF THE DISPLAY TECHNOLOGY

The electronic-display technology began with the advent of the Cathode Ray Tube (CRT) in the late nineteenth century¹. This discovery revolutionised a wide range of technologies with its potential to display information at high speed and definition rates permitting the development of novel technologies such as the TV and the oscilloscope. Previous displays were non-emissive and non-electronic which limited the technology to high luminance ambience, low speed and large sized displays. Reminiscences of these displays are still available in current applications such as airport information panels, road signs, car clocks or counters for gas or electricity readings among many others. However, the CRT and the extensive spectrum of electronic-display technologies which subsequently emerged, soon replaced non-electronic displays in many applications and allowed the development of new display technologies for mobile phones, digital watches, hand calculators and cash dispensers.

The electronic-display technology can be divided into two main categories, the *volumetric display technology* which requires large sized devices to display information and the *flat display technology* which reduces volumetric sizes to flat and light panels. The former includes devices such as the CRT or the light bulb. The latter is constituted by multiple flat display technologies developed in the last century^{2,3} such as: the Liquid Crystal Display (LCD), Plasma Display Panel (PDP), Vacuum Fluorescent Display (VFD), Alternating Current Thin Film Electroluminescent (ACTFEL) Display, Field Emission Display (FED), Light Emitting Diode (LED) and Digital Micromirror Display (DMD).

The entire range of electronic-displays can be additionally classified according to two major categories:

- *emissive displays* which base their operation on the emission of light from a particular phosphor or semiconductor.
- *non-emissive displays* which simply permit or prevent the passage of the light supplied by an auxiliary light source

A brief overview of the emissive and non-emissive technologies is given in the following section.

1.1.1 Emissive Displays

Within the emissive display group, the CRT is the maturest technology. Its operation relies on the excitation of a phosphor screen by high-energy electrons external to the phosphor. This phenomenon is usually known as cathodoluminescence⁴. As illustrated in Figure 1.1 a, the electron beam scans, a phosphor surface which radiates visible light after the electron impact. The device cavity is maintained under vacuum at a pressure within the order of 10^{-7} Torr. A magnetic or electrostatic field is utilised to direct the electron beam across the phosphor screen. Although complex and hazardous in principle, as a result of the high voltages required ($\sim 25,000$ V), CRTs have surprisingly managed to safely cover almost the entire display market. The success of CRTs is a consequence of their exceptional attributes: high resolution⁵ ($4.5 \mu\text{m}$ -diameter particles are utilised for most high-resolution CRT screens), high brightness ($>10,000\text{fL}$), excellent contrast and broad view angles ($\sim 160^\circ$). However, a series of disadvantages such as heat dissipation, colour and image vibrations, spherical faced screens and large size and weight are associated with the CRT performance. Image and colour variations occur as a result of magnetic interference between internal and external fields and can be reduced by isolation of the CRT. Distortion of the image with the eye position has been recently improved with the use of flat-faced CRTs⁶. However, heat dissipation, large size and weight are still drawbacks of the technology.

Another type of emissive display, also based on the cathodoluminescence phenomenon is the FED. This has recently undertaken rapid development. The device incorporates independent cathodes or microtips associated to each pixel which are activated by the application of an electric field, as illustrated in Figure 1.1 b. The emitted electrons are accelerated under vacuum by the anode voltage ($500\text{-}3,000$ V) and excite the phosphor causing it to emit visible light. The primary attraction of a FED is its ability to deliver high quality images in terms of efficiency (Candescent Technology Corporation claim an efficiency of 15lm/Watt ⁷), brightness (a 8" colour display made by Raytheon achieved a brightness of $3,420 \text{fL}$ ⁷), combined with view angle capabilities comparable to the CRT. The major issue of this technology is the undesired short lifetime^{8,9}. This problem is currently under investigation and recently, Fujitsu has demonstrated FED displays with 30,000 hour lifetime⁷.

After the CRT, the next most popular emissive display technology in the market is the Plasma Display Panel (PDP). The PDP operation is based on the excitation of a phosphor by the UV light radiated from a gas discharge as illustrated in Figure 1.1 c. This is generated within a vacuum cell which is filled with a rare gas. The emission is directly transmitted through the transparent electrode. Insulator ribs are incorporated which prevent the display from optical and electrical cross talk and additionally act as spacers between neighbour pixels. PDPs are lightweight, flat devices which provide full colour capabilities, high brightness ($\sim 1,880 \text{ fL}$)¹⁰ and very wide view angles ($\sim 160^\circ$). Unfortunately PD efficiencies decrease with pixel size and as a result, become unsuitable for small panel and high-resolution applications. PDPs are currently commercialised only for large area panels (a 60" PDP panel has been recently commercialised by Plasmaco⁹). The present challenge is reduction of the manufacturing cost and enhancement of the efficiency which is currently as low as 1.5 lm/Watt for the current structures.

Existing since 1967 is the VFD technology. Their mechanism is based on low voltage cathodoluminescence where a hot cathode is responsible for the emission of electrons which are accelerated towards the anode coated with a specific phosphor. A metallic grid positioned between the cathode and anode is addressed with a positive or negative voltage leading to acceleration of the electrons towards the anode or preventing these from reaching it. The cross section of a typical assembly is illustrated in Figure 1.1 d. Collision of the electrons with the phosphor-coated anode generates phosphorescence which is directly emitted to the outside through the glass plate. High-resolution displays incorporating VFDs are inefficient since the hot cathode is dissipating power continuously across the entire display. VFDs have however, achieved considerable success as alphanumeric displays being extensively used in hi-fi, CD players, and as backlights.

Reference should also be made to the well known LED. These are solid state semiconductor devices which generate light via the radiative recombination phenomenon. Their main advantages are their great reliability, high efficiency ($\sim 20 \text{ lm/Watt}$)¹¹, wide temperature range (from -20°C to 80°C) and low drive voltages ($< 15 \text{ V}$). The major disadvantage of this technology is the complexity of assembling large arrays of individual LEDs, the high power consumption and the low efficiency demonstrated by blue emitters.

The major interest of the presented work is the ACTFEL technology. Its operation is based on the high-field electroluminescence phenomenon¹². According to this, and as illustrated in

Figure 1.1 f, on the application of a specific voltage, electrons stored at the interface states between the phosphor and insulator layers are emitted into the phosphor conduction band and accelerated towards the opposite interface. On their way, the electrons interact and excite the activator centres located within the phosphor layer which then decay to the ground state with the emission of visible light. ACTFEL technology offers advantageous properties for many display applications since these are solid state structures suitable for purposes which require light and rugged displays. Also, as a result of the high - field electroluminescence mechanism, the device luminance response is largely insensitive to temperature¹³ within the range from -20°C to 80°C . Additionally, these are flat devices which can be utilised in fixed legends or matrix displays eliminating the need for an electron gun, when compared with the CRT. ACTFEL also provide high brightness ($> 1,200 \text{ fL}$) and have demonstrated long life ($> 40,000$ hours) and high reliability¹⁴. Another important characteristic of ACTFEL devices is their wide view angle ($\sim 160^{\circ}$) which makes them specially interesting for monitor screens. Their major disadvantage is the low efficiency obtained from true blue bright phosphor devices ($< 0.1 \text{ lm/Watt}$)¹⁵ which limits the display capabilities to monochrome panels or to occluded head up applications.

1.1.2 Non Emissive Displays

Among the non-emissive technology, the most important example with the maximum impact in the presently available display market is the LCD technology. This consists of a liquid crystal sandwiched between a polariser and an analyser, each coated with a transparent electrode. The light emitted from a backlight is polarised by the polariser and directed through the liquid crystal, as illustrated in Figure 1.2 a. For typical twisted nematic LCDs, the polarisation is rotated according to the rotation of the molecular structure and transmitted by the analyser. Under an applied voltage, the molecules of the liquid crystal line up with the electric field avoiding alterations on the light polarisation. Hence, the transmission of light through the analyser is prevented. Thus, LCDs are non-emissive displays since these only allow or prevent the passage of light from the light source. This mechanism provides very inefficient devices with values as low as $\sim 2 \text{ lm/Watt}$. However, the LCD technology has provoked a great interest in the display community which has induced a fast development of the technology in the last few years. LCDs are lightweight devices with full colour capabilities which require relative low addressing voltages ($\sim 8 \text{ V}$).

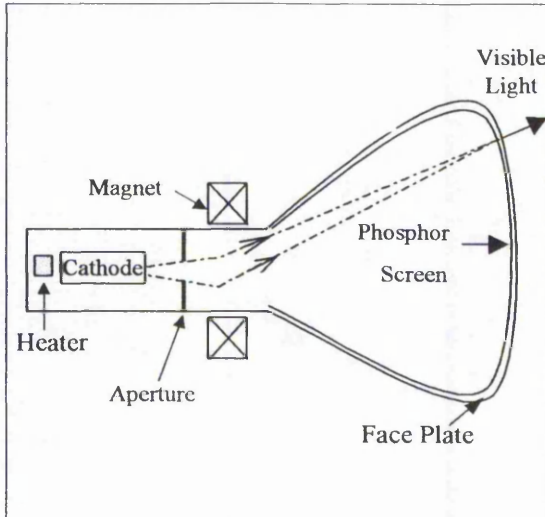


Figure 1.1a. CRT

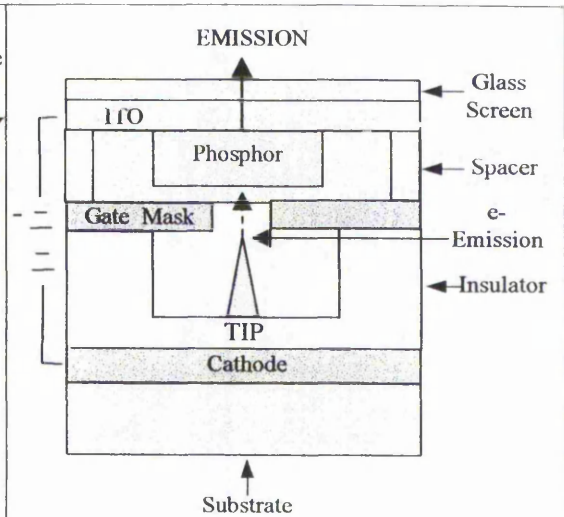


Figure 1.1b. FED

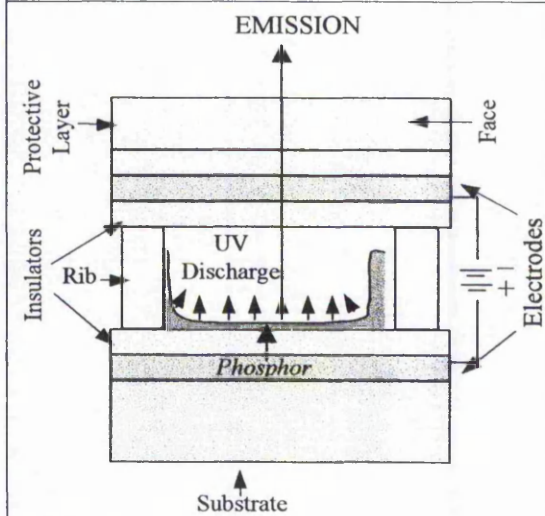


Figure 1.1 c. PDP

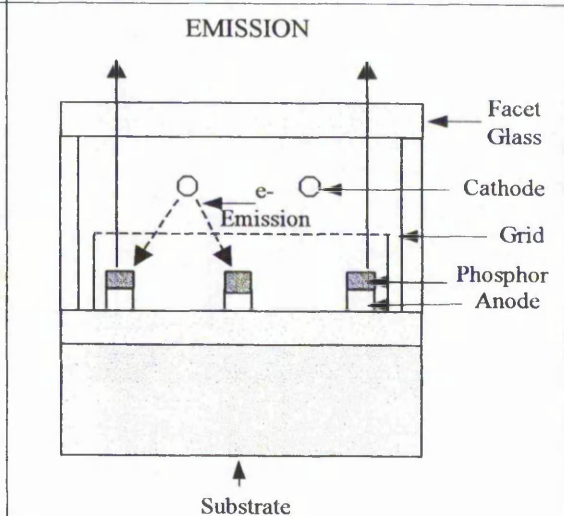


Figure 1.1 d. VFD

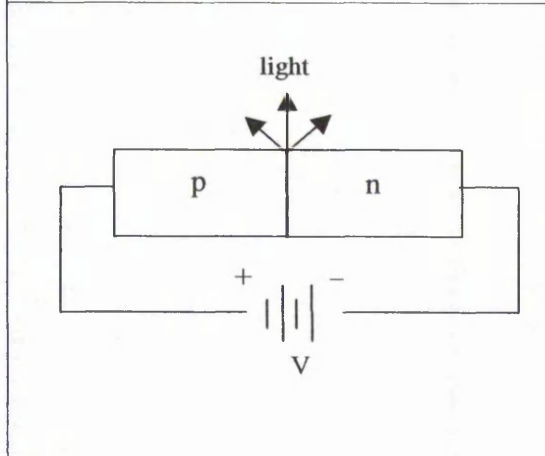


Figure 1.1 e LED

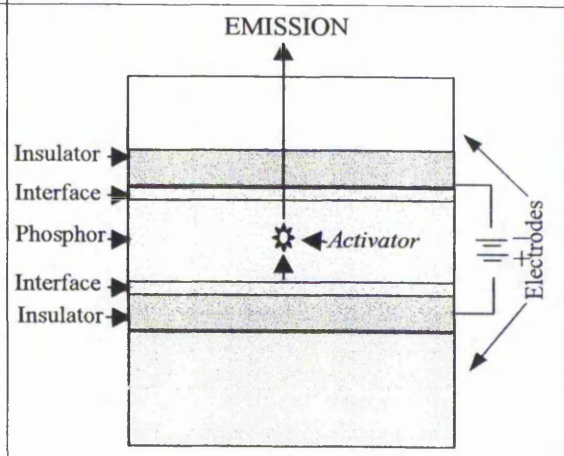


Figure 1.1 f TFEL

Figure 1.1 Emissive Displays

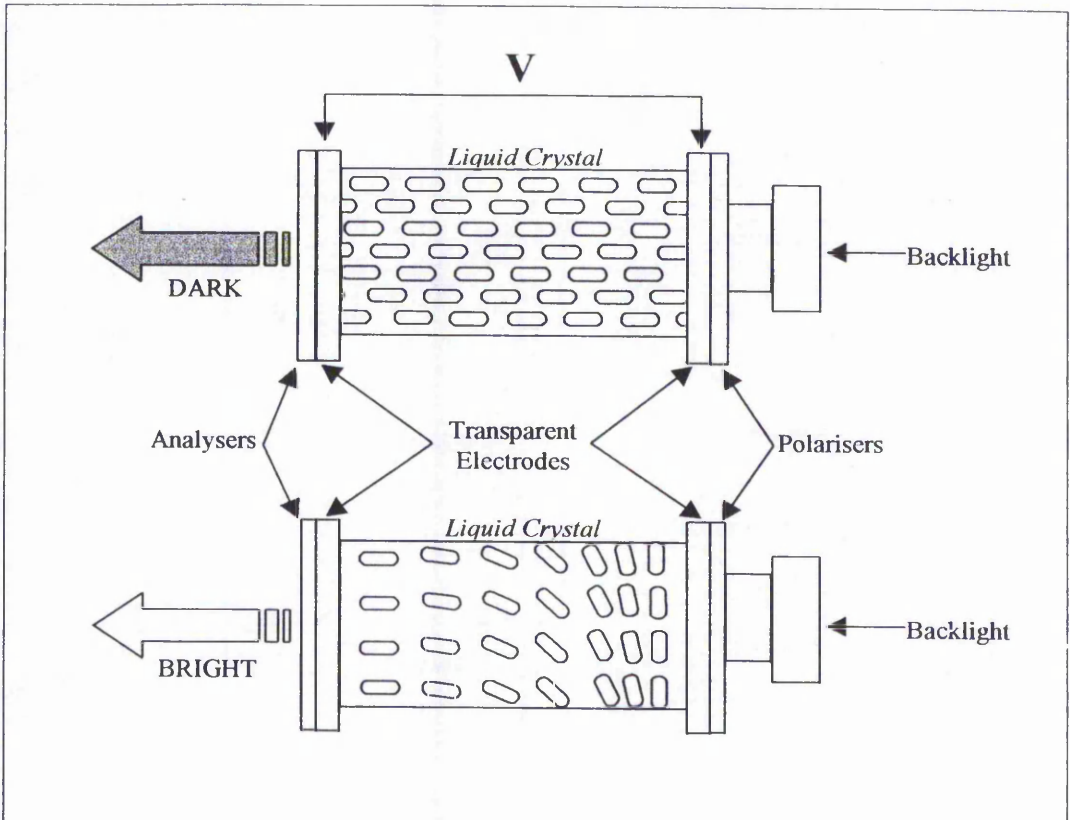


Figure 1.2 a Twisted Nematic LCD

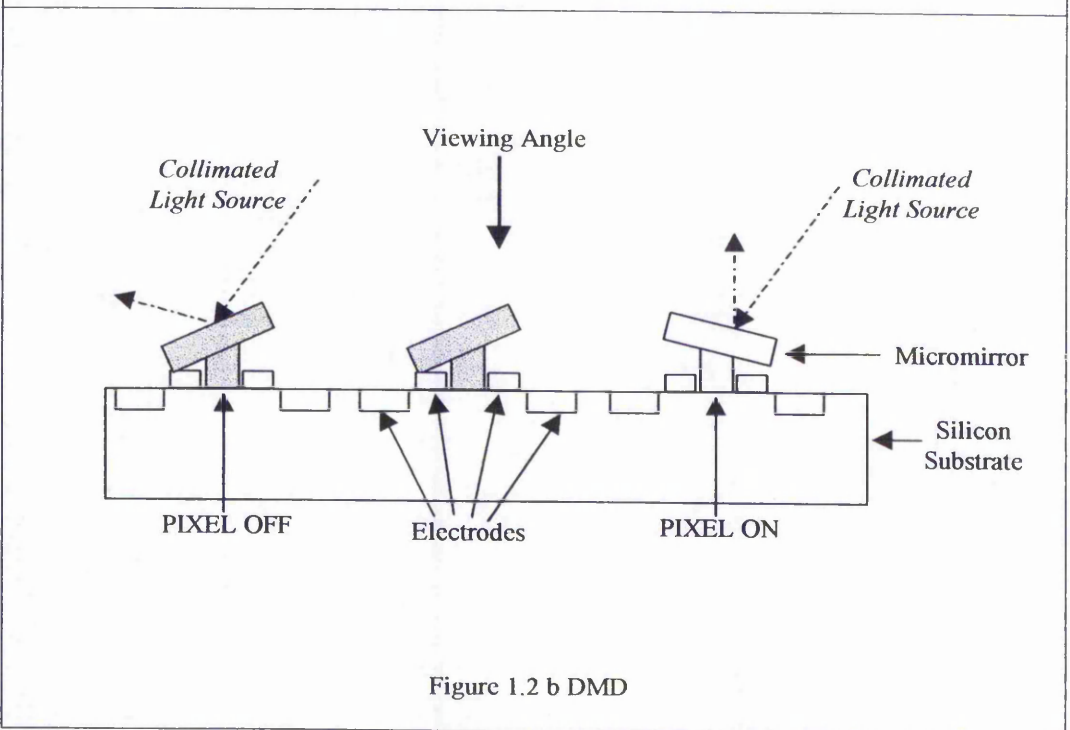


Figure 1.2 b DMD

Figure 1.2 Non-Emissive Displays

Apart from the low efficiency values, their major disadvantage is the narrow angle of view provided ($\sim 90^\circ$), which has been recently improved with the cost of further reduction of the efficiency¹⁶.

The other important non-emissive technology is the DMD. Figure 1.2 b illustrates the cross section of a typical DMD device which is made of digital micromirrors deposited onto a silicon substrate. Electrodes, placed at each side of the micromirror element, address the angle of tilt of the micromirror. As a result, the incoming light will be reflected in one or other direction. An 'on pixel' will reflect the light towards the viewing direction while an 'off pixel' will reflect the light away from the viewer position.

1.1.3 Display Technology Market Sectors

Display devices have a remarkable importance in society. The development of larger TV monitors and portable applications is undergoing fast development which significantly expands the display market. This can be classified according to two main categories: large area panels and microdisplays. Below, a brief description of large and microdisplay applications is provided as well as details of the display technologies utilised.

- *Large Area Panels*

Large area panels are generally utilised for high information content purposes such as TV screens or computer monitors. The earliest large area panel display, still dominant in the current display market, is the CRT¹⁷. To overcome the problems associated with CRTs, alternative display technologies were implemented to large area panels providing flat screens. Flat panels are slowly replacing the traditional CRTs, mostly in portable applications and in offices or public places where space is limited as a result of their smaller sizes and lighter weight. LCDs and PDPs are at present the dominant technology for large area flat panels. However, from the figures presented in Section 1.1, the former are yet to reach image qualities, in terms of high resolution and brightness, wide angle of view and low cost, comparable to the CRT. Reduction of fabrication costs is also required which permit expansion of the technology in broader markets.

- *Microdisplays*

The second main category of the display technology are the microdisplays¹⁸, usually implemented in applications such as: i) projection systems or ii) Head Mounted Displays (HMDs).

i) Projection systems¹⁹ capture the information contained in the microdisplay and magnify it to much larger sizes. These are applied in portable projectors for use in concerts and other live entertainment, and are also proposed for attractive future applications such as the electronic cinema²⁰. Microdisplays for this application must provide high resolution, brightness and contrast as well as full colour capabilities. LCDs have been found to be adequate for projection systems and have been commercialised.

ii) HMDs²¹ are optical devices attached to the head providing direct view of the information enclosed in the display. Two main categories can be distinguished: augmented and occlusive HMDs. The former superimposes the information contained in the microdisplay on the outside world while the latter occludes the viewer from external vision. Augmented HMDs are usually utilised in hardware applications such as engineering maintenance, Formula 1 drivers, and aircraft pilots. Occluded HMDs are mainly related with virtual reality applications. The lightweight and ruggedness required for most of HMD applications are facilitated by the microdisplay technology. Additionally, high brightness and contrast are required for augmented HMDs since these are usually utilised in highly illuminated ambience. Presently, LEDs and LCDs²² are commercialised for HMD applications and particularly, the solid state TFEL²³⁻²⁵ devices have demonstrated particular suitability for this application due to their exceptional ruggedness.

Furthermore, electronic-displays can be applied in electrophotographic printing (EP) applications. Successful attempts have been made in the past to address the photoreceptor with an LED image bar which is a high-resolution array of pixels²⁶. Each array element corresponds to a pixel which can be printed or not on the paper. Image bars could substitute lasers in typical electrophotographic printers²⁷. The incorporation of image bar leads to removal of various mechanical parts of laser printers which are highly responsible for device

failure and increase of printer cost. EP applications require high brightness and resolution displays which provide uniformity among the elements constituting the image bar.

In Table 1.1, the display technologies suitable for large area panels and microdisplay applications are presented.

	LARGE AREA PANELS			MICRODISPLAYS		
	COMPUTERS	TV	WALL PANELS	LAPTOPS	PROJECTION	HMDs
CRT	X	X			X	X
FED	X	X	X	X		X
PDP	X	X	X			
LED			X			X
ACTFEL				X		X
LCD		X	X	X	X	X

Table 1.1 Display Applications

The work presented in this thesis is particularly involved with the ACTFEL technology which demonstrates suitability for EP and microdisplay applications. An introductory background on the ACTFEL technology is given in the following section.

1.2 REVIEW OF THE ACTFEL DEVICE TECHNOLOGY

1.2.1 Brief History

Electroluminescence (EL) is the mechanism of light generation in ACTFEL technology. EL has been known since 1936 when Destriau²⁸ observed luminous radiation emitted from a powder material following the application of an electric field. This discovery encouraged some to initiate research of the phenomena reaching an important development of the EL powder-devices in the mid-sixties. Unfortunately, powder devices showed short lifetimes and low contrast and brightness which discouraged the commercial uptake.

In the mean time, the thin-film EL device technology was also under development. The first meaningful attempt to fabricate a thin-film EL device was carried out at the Bell Laboratories²⁹ although inefficient and unreliable devices were obtained as a result of this research. In 1974 Inoguchi et al.³⁰ published the first successful attempt to fabricate a reliable, long-lived, highly efficient thin film EL device. Soon after, renewed interest was generated in the scientific community. Thus, in the past 20 years modelling of the ACTFEL physical behaviour has been performed and increasing efforts to improve the device characteristics have been made by many research groups³¹⁻³⁶. Nowadays, various companies, amongst others Sharp and Planar International, commercialise ACTFEL displays.

1.2.2 The Structure and Electrical Characteristics of ACTFEL Devices

The ACTFEL devices presently developed maintain the basic structure initially established by Inoguchi. This is illustrated in Figure 1.1 f and consists of a phosphor thin film sandwiched between two dielectric layers. An opaque electrode is deposited onto the top dielectric and a transparent conductor is utilised as the bottom electrode. The film stack is deposited onto a glass substrate. On the application of an AC voltage, light is generated within the phosphor thin film and subsequently coupled out through the transparent electrode.

A typical Brightness versus Voltage (BV) characteristic, is illustrated in Figure 1.3 where three well defined regions can be observed:

1. The region for voltages lower than the threshold voltage V_{th} , where non-emission is observed.
2. The turn on region for voltages above the threshold voltage V_{th} , which is characterised by a high increase of brightness with voltage.
3. The saturation region where the brightness is hardly enhanced with voltage.

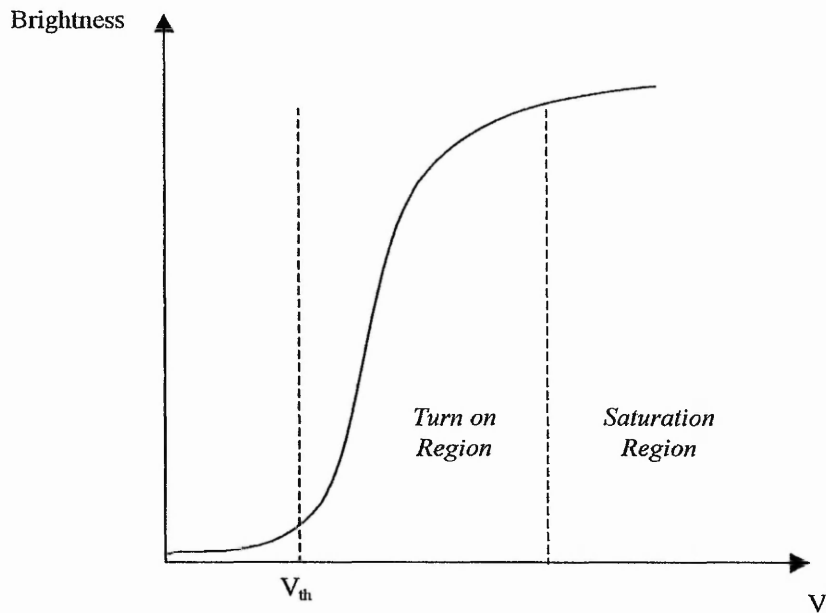


Figure 1.3 Typical BV Characteristic of a TFEL Device

This highly non-linear BV characteristic can be justified based on the physical concept of EL. This is the non-thermal conversion of electrical energy into luminous energy which can be divided into two main categories: *electron injection* and the *high-field* electroluminescence. Past investigations have established a “simple model” which explains the ZnS:Mn ACTFEL operation in terms of high-field electroluminescence^{37,38}. Based on this model, high-field electroluminescence can be described as the sequence of four main steps: *electron injection, electron acceleration, impact excitation and light emission* as illustrated in Figure 1.4.

1. *Electron injection* has been generally accepted to be the result of a high field assisted tunnelling of electrons from the disordered interface between the insulator and the phosphor film into the conduction band of the phosphor thin film.
2. *Electron acceleration* occurs on travelling through the phosphor layer as a result of the generated high electric field, typically around $1.5 \cdot 10^6 \text{ Vcm}^{-1}$ for ZnS:Mn.
3. *Impact excitation* takes place when the injected electrons acquire enough energy, around 2.4 eV, and excite a Mn^{2+} ion.
4. *Light emission* follows the radiative Mn^{2+} decay with a lifetime of approximately 1 ms.

The impinging electron travels through the phosphor layer towards the opposite interface. This causes polarisation of the charge which eventually generates a “clamping” effect on the electric field. This explains the saturation region of the BV characteristic. If reversed polarisation of the external field is applied the field is unclamped and the high field electroluminescent process is reverted and results in light emission.

Notice that two threshold voltages require distinction: the *tunnel threshold voltage* which is the minimum voltage required to tunnel inject an electron from the interface states into the ZnS:Mn conduction band; and the *radiative threshold voltage* which is the minimum voltage required for the electrons to gain enough energy to excite the Mn^{2+} centres. From this point forward threshold voltage will refer to the radiative threshold voltage unless stated otherwise.

The ACTFEL device efficiency can be divided into radiative efficiency and outcoupling efficiency. The former relies on the efficiency of the four processes previously described: electron injection, electron acceleration, impact excitation and light emission. The latter is responsible for the coupling of light out of the device.

The radiation efficiency is dependent on the interface nature and the phosphor properties^{39,40}. To be efficient, the luminescent centre must have a large impact cross-section and the host-dopant combination must be stable at high electric fields. For ACTFEL devices, ZnS:Mn has been demonstrated to be the most efficient combination ($\sim 3 \text{ lm/Watt}$)⁴¹. A typical ZnS:Mn spectrum provides a maximum emission at a wavelength of 585 nm with a FWHM of

approximately 50 nm. Consequently, ACTFEL displays incorporating ZnS:Mn are seen by the viewer as a yellow monochrome display. A full colour display requires the use of a white phosphor in combination with a filter which selects the colour of the emitted light. Full colour ACTFEL devices can be also achieved by the incorporation of alternative host-dopant combinations. Up to date, green and blue phosphor emitters have demonstrated low efficiencies ($\sim 1.3 \text{ lm/Watt}$)⁴², which are too small for this aim.

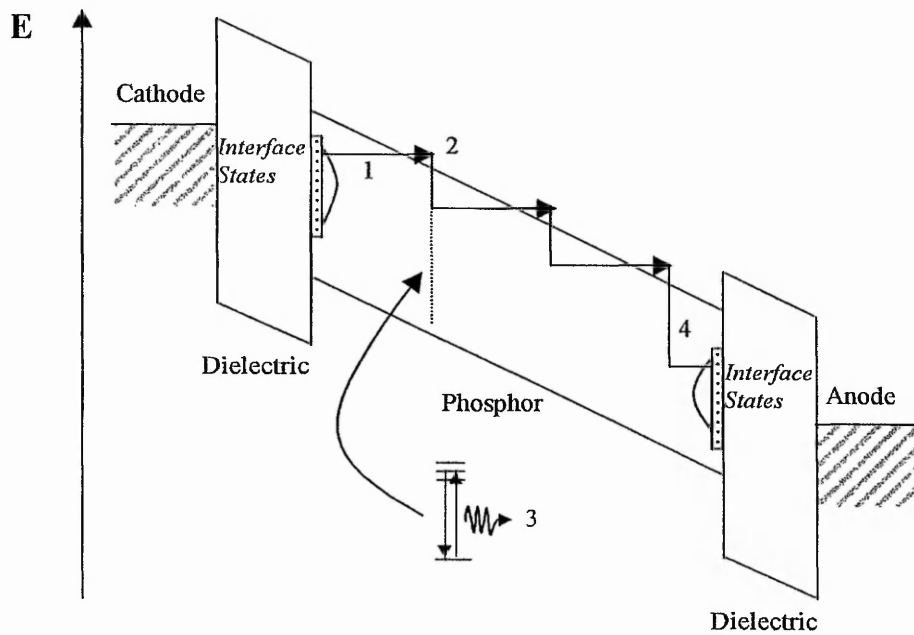


Figure 1.5 Schematic diagram showing the performance mechanism of high-field electroluminescence

The outcoupling efficiency is mainly dependent on the nature of the internally generated light and the outcoupling process. In ACTFEL devices light is coupled out through the transparent electrode surface. From geometric optics and assuming perfect smooth interfaces, only 10% of the generated light is coupled out of the device. Thus, the rest is waveguided within the thin film structure. The high difference in the refractive index between the phosphor and the dielectric film accounts for the waveguiding of light within the structure. This low efficiency value reveals the opportunity for improvement of the total device efficiency by overcoming the restrictions of the outcoupling efficiency.

A variant of the ACTFEL structure is the electroluminescent edge emitter which has been developed in the past as light source for EP applications⁴³. As illustrated in Figure 1.6, edge emitters substitute the transparent electrode by an opaque electrode and consequently laterally outcoupled the propagated light through the cleaved edge. This structure enhances the outcoupling efficiency when compared with typical ACTFEL devices however, it becomes unsuitable for applications such as panel displays.

The Display Group at the Nottingham Trent University has been involved with the development of electroluminescent devices⁴⁴⁻⁴⁶ in recent years and has introduced a novel structure known as the Laterally Emitting Thin Film Electroluminescent Display (LETFEL) device⁴⁷. This is the device of interest in the presented research and details on this technology are given in the following section.

1.3 REVIEW OF THE LETFEL TECHNOLOGY

The LETFEL device is a novel configuration of ACTFEL technology and has shown to further improve the device brightness⁴⁸. The concept of the LETFEL device structure is shown in Figure 1.5 . It consists of a phosphor thin film sandwiched between two dielectric layers. An opaque electrode is deposited onto the top dielectric layer and a Si substrate is utilised as the bottom electrode. On the application of an AC voltage, light is generated within the phosphor film, as in a conventional ACTFEL device. Due to the different refractive indexes between insulator and phosphor layers, the light is partly waveguided within the ZnS:Mn film and partially outcoupled at the emitting aperture, where the top electrode has been removed.

LETFEL are a recently developed technology which combines the laterally waveguiding performance typical of edge emitters with the top surface emission characteristic of Thin Film Electroluminescent (ACTFEL) flat panel display devices, in an attempt to achieve brightness enhancement. Figure 1.6 illustrates a comparison of typical ACTFELs, LETFELs and electroluminescent edge emitters. In ACTFEL devices light outcoupling occurs along the entire pixel surface throughout the transparent electrode. In edge emitters this electrode is opaque and light is laterally outcoupled through the cleaved edge. LETFEL devices combine the use of opaque electrodes, with surface emission at the aperture locations where

outcoupling occurs. The LETFEL outcoupling mechanism, differs from other outcoupling technologies since it simultaneously optimises the light outcoupling efficiency and converts the laterally waveguided light into surface emission. Light outcoupling occurs at the device aperture regions which need to be designed in order to optimise the light output properties. As the major applications of LETFEL devices, i.e. HMDs and EP, provide small acceptance angles, the light output must provide high brightness and low divergence.

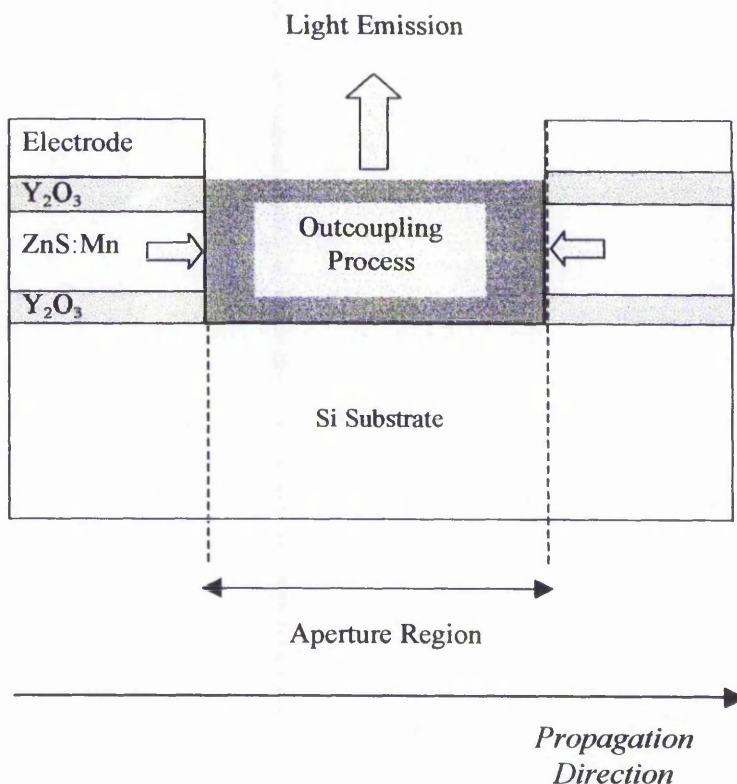
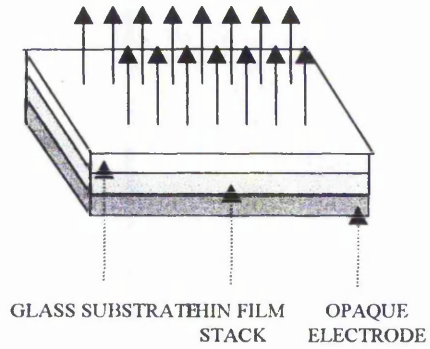


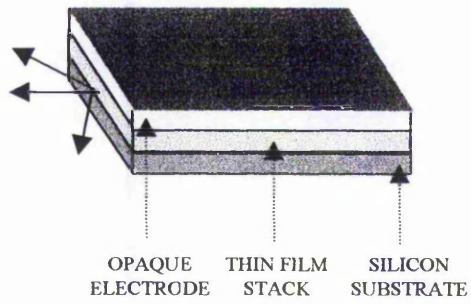
Figure 1.5 Diagram illustrating a cross section of a LETFEL device

Currently, the LETFEL outcoupling mechanism incorporates microstructures which bend the waveguide at the aperture regions and introduce scattering and bend radiation losses which are utilised as outcoupled light. For ease of fabrication, this outcoupling technology has been utilised up to now and we will refer to it as the conventional non-etched LETFEL structure. No theoretical or experimental determination has been performed on the light output properties of these structures. As a result, a study of the conventional non-etched LETFEL devices and potential solutions to the encountered limitations are required.

TFEL



EDGE EMITTER



LETFEL

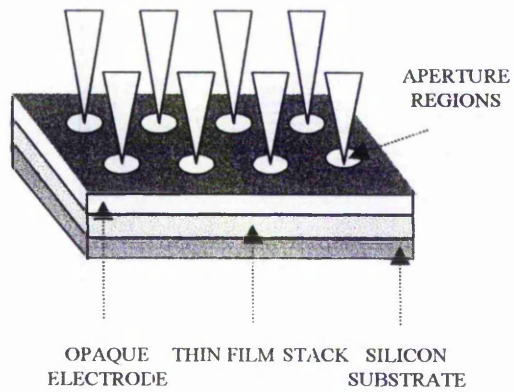


Figure 1.6 Comparison of a TFEL, Edge emitter and a LETFEL structure.

1.4 SUMMARY OF THESIS

Research on the outcoupling mechanism of LETFEL devices has been carried out within the Display Group at the Electrical and Electronic Engineering Department at the Nottingham Trent University. The aim is to enhance the outcoupling efficiency and to improve the angular distribution of the emitted light. A primary theoretical study of the waveguide transmission and losses within the devices has been performed. This has been followed by an analysis of the outcoupling properties of the mechanism currently utilised which emphasises the limitation of this technique. Two alternative mechanisms are proposed which theoretically demonstrate improvement of the angular profile. A fabrication route to generate the outcoupling mechanism is presented which incorporates ion milling, a sputter etch technology. A calibration of the milling parameters for the LETFEL thin films was undertaken. The two proposed outcoupling mechanisms were fabricated and the resultant light outputs were determined and compared with the theoretical results and the conventional device properties. Below is a summary of each chapter.

CHAPTER 2

THEORETICAL MODELLING OF LIGHT TRANSMISSION IN LETFEL DEVICES

This chapter describes the character of light transmission in LETFEL devices. It starts with a general study of modal propagation in the LETFEL waveguide and the radiation losses due to surface roughness. Subsequent comparison between the theoretical losses and previously published experimental results leads to the significant conclusion that the generated light is mainly transmitted within the LETFEL waveguide as the fundamental mode.

CHAPTER 3

THEORETICAL MODELLING OF THE OUTCOUPLING MECHANISM OF LETFEL DEVICES

A theoretical study of the outcoupling mechanism of the current LETFEL structures is performed which provides low outcoupling efficiency values. As a result, two alternative mechanisms are proposed the etched aperture and the surface emitting edge emitter LETFEL device. Theoretical simulations of the outcoupling are performed which determine an improvement in the angular profile of the emitted light.

CHAPTER 4

EXPERIMENTAL DETAIL

Reliable fabrication of the device is required. In this chapter, a successful route for fabricating etched devices using ion milling is presented for the first time. A full description of the equipment and processes used is given. Details on the instrumentation required to characterise the output properties are also provided.

CHAPTER 5

ION MILLING CHARACTERISTICS OF LETFEL DEVICES AND ASSOCIATED MATERIALS

The ion milling etch-rates of LETFEL thin films are determined for various process parameters. The effect of ion milling on the etched walls is also studied and comparison with theoretical modelling of the process provides explanation of the milling operation.

CHAPTER 6

EXPERIMENTAL DETERMINATION OF THE LIGHT OUTPUT PROPERTIES OF LETFEL DEVICES

This chapter presents experimental data, including fabrication conditions, light intensity and angular distributions, of LETFEL devices incorporating the traditional and novel outcoupling mechanisms. A comparison among the various techniques is presented

CHAPTER 7

CONCLUSIONS

A summary of the work and achievements obtained is provided as well as a brief description of future work to be developed.

**THEORETICAL MODELLING OF LIGHT
TRANSMISSION IN LETFEL DEVICES**

-
- 2.1 Introduction
 - 2.2 Maxwell Equations
 - 2.3 Scattering Losses
-

2.1 INTRODUCTION

The phenomena of light transmission can be generally described by the electromagnetic theory of light postulated by James Clerk Maxwell (1831-1879)⁴⁹. This allows a unique determination of the electromagnetic field from a given distribution of current and charges in the propagation media. According to this theory, arbitrary light waveforms propagating within an optical guiding structure can be represented by the combination of guided and radiation modes. The former are found to be quantified into a discrete set of guided modes⁵⁰ since from the continuum of rays within the limit of total reflection, only a discrete number are allowed to be guided within the structure. These satisfy the condition of constructive interference when they superimpose upon themselves after successive reflections at the sidewalls. The rest of the propagating angles will interfere destructively and will not provide a self-consistent field distribution.

The electromagnetic theory of light in guiding structures has been utilised in this chapter to study the transmission behaviour of the light generated within a LETFEL device. This device can be compared to a symmetrical slab optical waveguide where the ZnS:Mn layer behaves as the core and the Y₂O₃ constitutes the claddings. Maxwell equations have been solved for this particular case providing the corresponding guided mode expressions. Taking into account these expressions and previous results published by Marcuse⁵¹, the scattering losses due to surface roughness were calculated. Note that this initial study is merely related to the intrinsic nature of the LETFEL waveguide and is independent of the particular electromagnetic field existing within the structure. If an electromagnetic field is considered, partial coupling might occur into the guided modes. To determine the corresponding coupling power, formulation of the field expression is required. As in LETFEL devices light is produced at the Mn²⁺ centers distributed along the entire phosphor layer, the description of the electromagnetic field is complex. Alternatively, this chapter provides a description of the coupling power of the generated light into the guided modes from comparison of theoretical attenuation constants with previously published experimental results. Agreement between the empirical and theoretical studies is observed which introduces a general understanding of light transmission within LETFEL devices and indicates the suitability of the theoretical model.

2.2 MAXWELL EQUATIONS

Maxwell equations in a linear and isotropic media assumed to be non-magnetic and charge free with low losses can be expressed as:

$$\nabla \times \mathbf{E} = -\partial \mathbf{B} / \partial t \quad 2.1$$

$$\nabla \times \mathbf{H} = \partial \mathbf{D} / \partial t \quad 2.2$$

$$\nabla \cdot \mathbf{D} = 0 \quad 2.3$$

$$\nabla \cdot \mathbf{B} = 0 \quad 2.4$$

denoting t as the time, $\nabla = (\partial / \partial x)\hat{\mathbf{i}} + (\partial / \partial y)\hat{\mathbf{j}} + (\partial / \partial z)\hat{\mathbf{k}}$ is the del operator, \mathbf{E} is the electric field, \mathbf{H} is the magnetic field, and \mathbf{D} and \mathbf{B} are the electric and magnetic flux densities. The field amplitudes, \mathbf{E} and \mathbf{H} are related to the flux densities \mathbf{D} and \mathbf{B} , by the equations:

$$\mathbf{D} = \epsilon \cdot \mathbf{E} \quad 2.5$$

$$\mathbf{B} = \mu \cdot \mathbf{H} \quad 2.6$$

taking ϵ as the electric permittivity and μ the magnetic permeability. For a linear medium, ϵ and μ are independent of the electric and magnetic field amplitudes and depend exclusively on the nature of the medium.

Equations 2.1-2.4 are first-order differential equations, which can be transformed into a single second-order differential equation known as the wave equation. Taking the curl of Equation 2.1:

$$\nabla \times \nabla \times \mathbf{E} = \nabla \times \left(-\partial \mathbf{B} / \partial t \right) \quad 2.7$$

and from Equation 2.6 and assuming that μ is independent of time and position:

$$\nabla \times \nabla \times \mathbf{E} = \nabla \times \left(-\partial \mu \mathbf{H} / \partial t \right) = -\mu \left(\nabla \times \partial \mathbf{H} / \partial t \right) \quad 2.8$$

Since the functions are continuous, the order of the curl and the derivative can be reversed. If Equation 2.2 and 2.5 are considered:

$$\nabla \times \nabla \times \mathbf{E} = -\mu \frac{\partial}{\partial t} (\nabla \times \mathbf{H}) = -\mu \frac{\partial}{\partial t} \left(\frac{\partial \mathbf{D}}{\partial t} \right) = -\mu \epsilon \frac{\partial^2 \mathbf{E}}{\partial t^2} \quad 2.9$$

Using the identity:

$$\nabla \times \nabla \times \mathbf{E} = \nabla(\nabla \cdot \mathbf{E}) - \nabla^2 \mathbf{E} \quad 2.10$$

and since:

$$\nabla \mathbf{D} = \nabla(\epsilon \cdot \mathbf{E}) = (\nabla \epsilon) \cdot \mathbf{E} + \epsilon \cdot (\nabla \cdot \mathbf{E}) = 0 \quad 2.11$$

and assuming the gradient of the electrical permittivity, $\nabla \epsilon$, negligible, solves $\nabla \cdot \mathbf{E} = 0$. As a result, the wave equation reduces to:

$$\nabla^2 \mathbf{E} - \mu \epsilon \frac{\partial^2 \mathbf{E}}{\partial t^2} = 0 \quad 2.12$$

If in Equation 2.7 the curl of Equation 2.2 is taken, a wave equation can be obtained for the magnetic field from similar calculations to [2.8-2.11]:

$$\nabla^2 \mathbf{H} - \mu \epsilon \frac{\partial^2 \mathbf{H}}{\partial t^2} = 0 \quad 2.13$$

Consider the symmetric waveguide illustrated in Figure 2.1 where the refractive index of the core layer is $n_f=2.35$, and the surrounding materials have a refractive index $n_s=1.9$. A Cartesian coordinate system can be selected where the guiding layer has a thickness of $h=0.8 \mu\text{m}$ along the x-axis and the cladding thickness is assumed to be infinity. The direction of light propagation is along the z-axis and the waveguide is assumed to be infinitely long along the y-axis which permits a one-dimensional analysis.

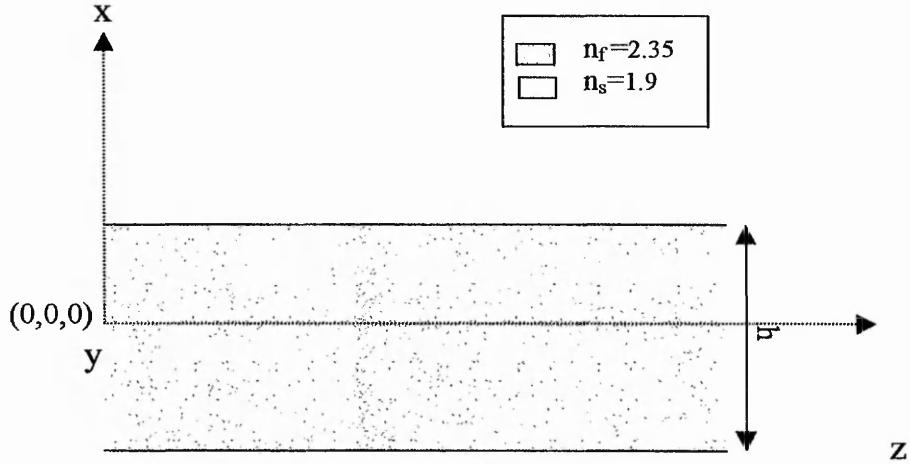


Figure 2.1 Typical LETFEL waveguide

The scalar wave equation can be defined as:

$$\nabla^2 \Psi_i - \mu \epsilon \frac{\partial^2 \Psi_i}{\partial t^2} = 0 \quad 2.14$$

for Ψ the amplitude of either the electric or magnetic field in each direction $i = x, y, z$. Solutions to these equations can be found using the method of variable separation:

$$\Psi(r, t) = \Phi(r) \cdot \Theta(t) = \Phi_0 e^{ikr} e^{i\omega t} + c.c. \quad 2.15$$

assuming a complex exponential dependence on time where Φ_0 is the amplitude, k is the wavevector, ω is the angular frequency. For the TE mode, which is polarised along the y axis, and assuming a sinusoidal wave with angular frequency ω_0 , where $k_0 = \omega_0/c$, and the refractive index $n_j = \sqrt{\mu_j \epsilon_j}$, the spatial wave Equation 2.14 for the electric field becomes:

$$\nabla^2 E_y + k_0^2 n_j^2 E_y = 0 \quad 2.16$$

where n_j can be $n_f=2.35$ or $n_s=1.9$ depending on the medium where the equation is evaluated. A trial solution for this spatial equation is:

$$E_y(x,z) = E_y(x) \cdot e^{-i\beta z} \quad 2.17$$

where β is known as the propagation constant. Substituting this solution into Equation 2.16 leads to:

$$\frac{\partial^2 E_y(x)}{\partial x^2} + (k_0^2 n_i^2 - \beta^2) E_y(x) = 0 \quad 2.18$$

The general solution of this equation depends on the relative value of β with respect to $k_0 n_i$. For the interval where $|\beta| < k_0 n_i$, the solution has an oscillatory form, i.e.:

$$E_y(x) = E_0 \exp(\pm i \sqrt{k_0^2 n_i^2 - \beta^2} x) \quad 2.19$$

For the region where $|\beta| > k_0 n_i$, the solution has an exponentially decaying form, i.e.:

$$E_y(x) = E_0 \exp(-\sqrt{\beta^2 - k_0^2 n_i^2} x) \quad 2.20$$

When the β values fall within the interval $0 < |\beta| < k_0 n_s$, oscillatory solutions are generated within both the core and the cladding regions, as illustrated in Figure 2.2. These solutions constitute a continuum set of modes, known as the radiation modes, which fail to confine the energy over finite distances from the guiding film. When β falls within the interval $k_0 n_s < |\beta| < k_0 n_f$, an oscillatory profile is generated within the guiding film and an exponential decaying distribution is produced in the claddings. These solutions form a discrete set of orthogonal modes, known as the guided modes, which confine the energy within a finite distance to the core.

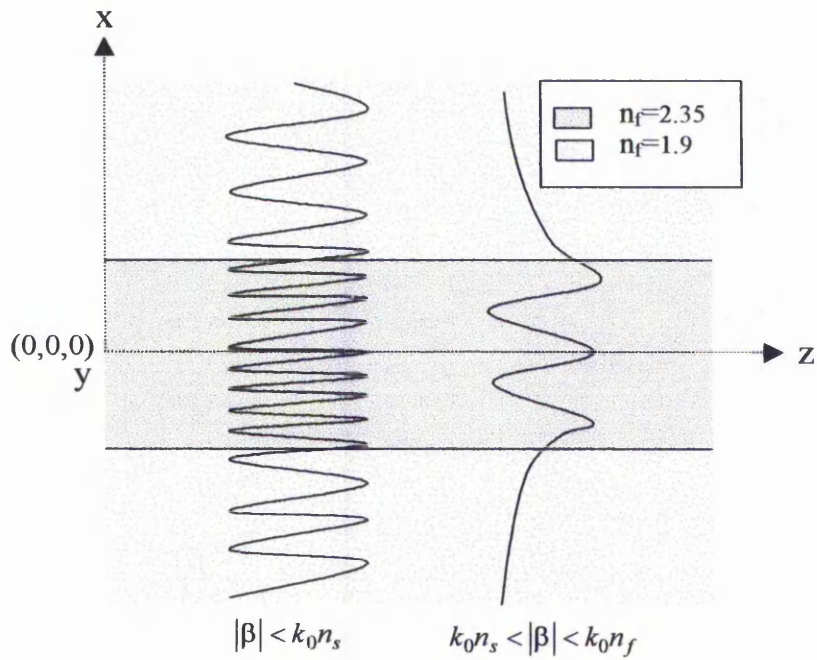


Figure 2.2 Different propagation regimes within a waveguide

The guided modes together with the radiation modes form a complete set of orthogonal modes, which permits the description of any field distribution, which is solution of the wave equation as the expansion:

$$E_y(x) = \sum_{v=1}^n C_v(z) E_v(x) + \int_0^{\infty} C(v,z) E(v,x) dv \quad 2.21$$

where the summation extends to n which is the discrete number of guided modes $E_v(x)$, and the integral to the continuum of radiation modes, $E(v,x)$. $C_v(z)$ constitutes a discrete set of n continuous functions of z representing the amplitudes of each guided mode v . $C(v,x)$ is a continuous function of v , and z , and represents the amplitude of the continuum spectrum of radiation modes. A general description of both guided and radiation modes is provided in the following sections.

2.2.1 The Guided Modes

As previously mentioned, the guided modes satisfy the condition $k_0 n_s < |\beta| < k_0 n_f$ and for the particular case of a symmetric planar waveguide as the illustrated in Figure 2.1, these are described by the following field distributions⁵²:

$$E_y(x) = E_0 e^{-\gamma(x-h/2)} \quad x \geq h/2 \quad 2.22 \text{ a}$$

$$E_y(x) = E_0 \frac{\cos(\kappa x)}{\cos(\kappa h/2)} \quad \text{or} \quad E_y(x) = E_0 \frac{\sin(\kappa x)}{\sin(\kappa h/2)} \quad -h/2 < x < h/2 \quad 2.22 \text{ b}$$

$$E_y(x) = \pm E_0 e^{-\gamma(x+h/2)} \quad x \leq -h/2 \quad 2.22 \text{ c}$$

where E_0 is an arbitrary unknown constant and:

$$\gamma = \sqrt{\beta^2 - (k_0 n_s)^2} \quad 2.23 \text{ a}$$

$$\kappa = \sqrt{(k_0 n_f)^2 - \beta^2} \quad 2.23 \text{ b}$$

are the extinction coefficient and the transverse wavevector respectively. Due to the symmetric character of the waveguide, guided modes with even or odd symmetry can be excited. A cosine or a sine distribution describes the corresponding electric field distributions in Equation 2.22 b.

Taking into account the boundary conditions which impose continuity of the tangential components of \mathbf{E} and \mathbf{H} at the interface, the characteristic eigenvalue equations for the TE modes result in⁵²:

$$\tan(\kappa h/2) = \gamma / \kappa \quad \text{for even modes} \quad 2.24 \text{ a}$$

$$\tan(\kappa h/2) = -\kappa / \gamma \quad \text{for odd modes} \quad 2.24 \text{ b}$$

These equations are graphically illustrated in Figure 2.3, for the particular case of the LETFEL waveguide, where the intersection between the left and right hand side curves represent allowed values of κ .

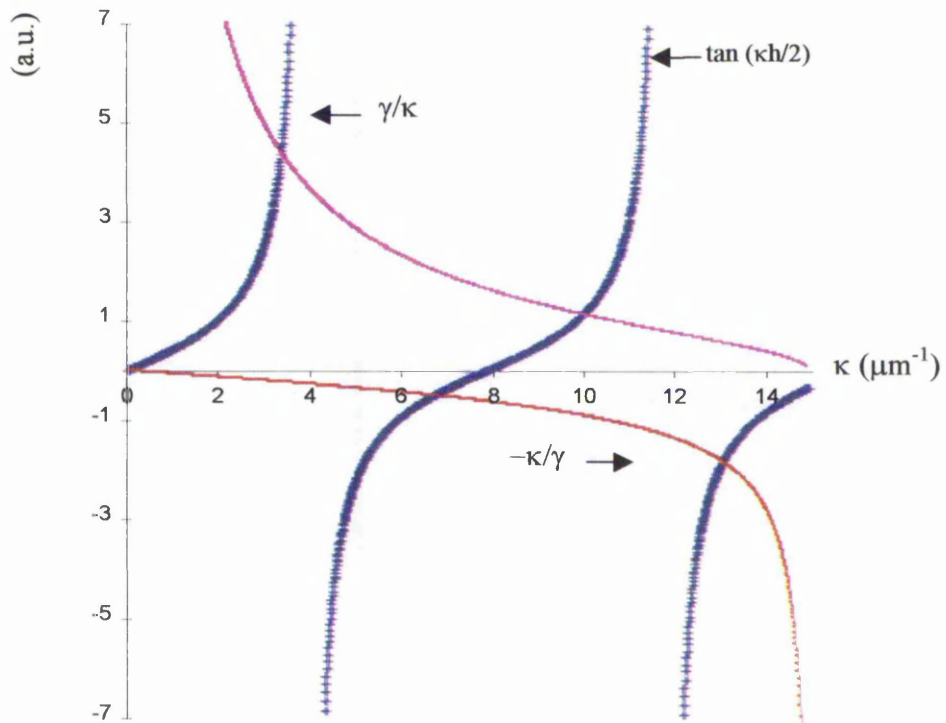


Figure 2.3 Characteristic equation for LETFEL waveguides

These values have been numerically calculated using Matlab[®] by determining the zeros of the functions 2.25 a and 2.25 b:

$$y_1 = \tan(\kappa h / 2) - \gamma / \kappa \quad \text{for even modes} \quad 2.25 \text{ a}$$

$$y_2 = \tan(\kappa h / 2) + \kappa / \gamma \quad \text{for odd modes} \quad 2.25 \text{ b}$$

The four allowed values of κ are included in Table 2.1 which represent the four guided modes within the waveguide. The values of γ and β , obtained from expressions 2.23 a and 2.23 b are included in Table 2.1.

	Mode 0	Mode 1	Mode 2	Mode 3
β (μm^{-1})	25.0160	24.3338	23.1980	21.6160
κ (μm^{-1})	3.3570	6.6866	9.9466	13.0320
γ (μm^{-1})	1.4468	1.3263	1.1031	7.1264

Table 2.1 Values of the propagation constant, β , transverse vector, κ , and extinction coefficient, γ , for LETFEL waveguides

The time averaged power, P , per unit length along the z -axis carried by each mode is given by the expression⁵²:

$$P = \frac{1}{2} \left(\frac{\beta}{2\omega\mu} \right) \int_{-\infty}^{+\infty} |E_y(x)|^2 dx \quad 2.26$$

and the normalisation condition, $P=1$, leads to a field amplitude value of⁵³:

$$E_0^2 = \frac{2\omega\mu}{\beta h + \beta/\gamma} \quad 2.27$$

The normalised spatial guided mode distributions for this particular LETFEL waveguide have been calculated and are illustrated in Figure 2.4. The fundamental mode, with the highest value of β , has even symmetry and a maximum centered in the middle of the core layer. Higher order modes have alternating even and odd symmetry. Note that although energy is confined within the structure, there is an evanescent tail extending in the cladding which becomes wider, the higher the order of the mode.

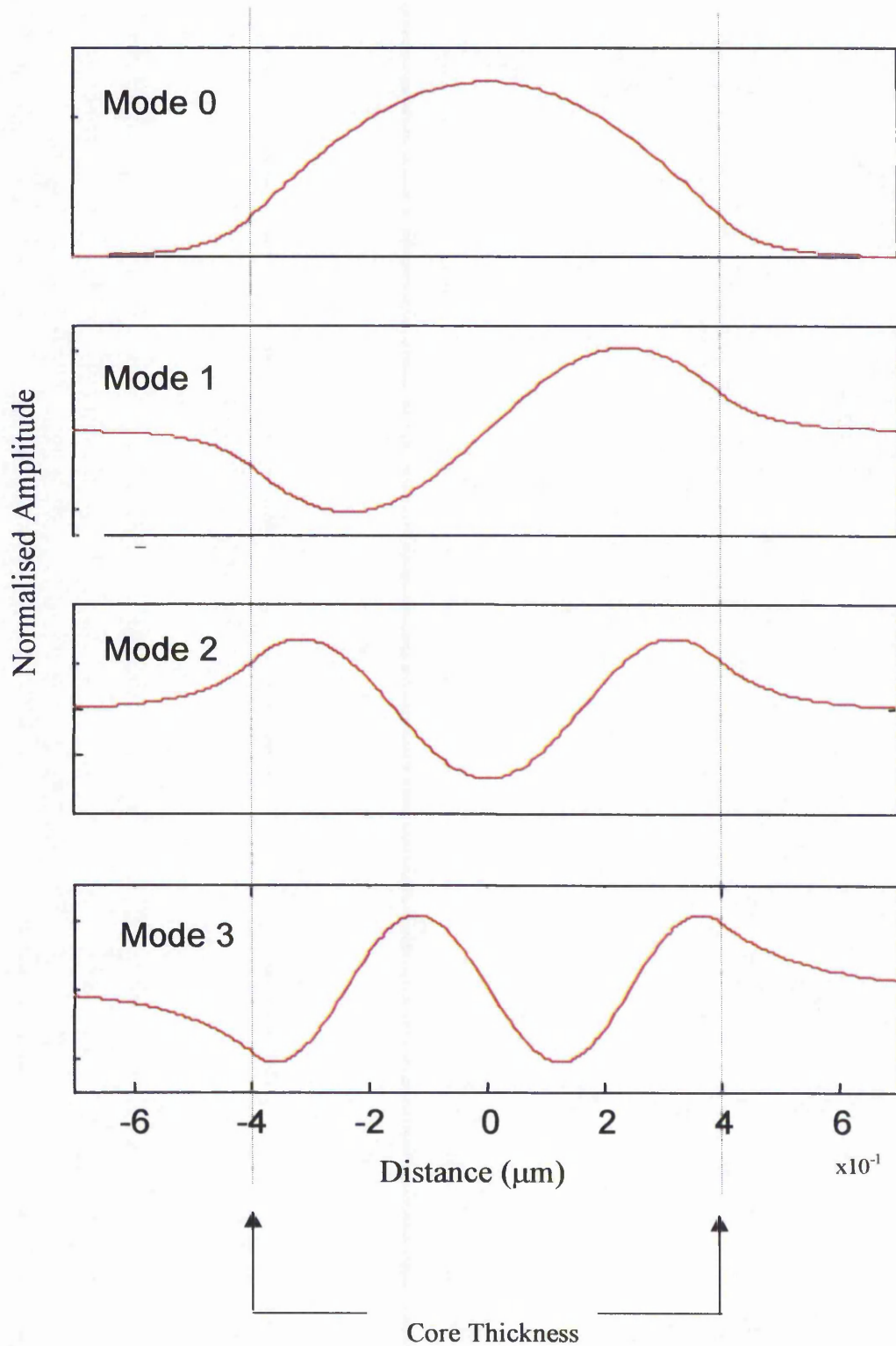


Figure 2.4 Transverse profile of the four allowed guided modes in LETFEL waveguides

2.2.2 The Radiation Modes

The radiation modes are solutions of the wave equation presented in Equation 2.18 when the propagation constant values belong to the interval:

$$0 \leq |\beta| \leq n_s k$$

These constitute a continuum set of modes which provide oscillatory field distributions within the cladding and core layers. The electric field is given by⁵¹:

$$E_y = B_1 \cos(\eta x) \quad \text{for } |x| \leq d \quad 2.28 \text{ a}$$

$$E_y = B_2 \sin(\eta x)$$

$$E_y = C_1 e^{i\rho x} + D_1 e^{-i\rho x} \text{ for even symmetry} \quad \text{for } |x| \geq d \quad 2.28 \text{ b}$$

$$E_y = C_2 e^{i\rho x} + D_2 e^{-i\rho x} \text{ for odd symmetry}$$

with:

$$\rho = \sqrt{(n_s^2 k^2 - \beta^2)} \quad 2.29 \text{ a}$$

$$\eta = \sqrt{(n_f^2 k^2 - \beta^2)} \quad 2.29 \text{ b}$$

being the radiation mode constants.

$$C_1 = \frac{1}{2} B_1 e^{-i\rho d} \left(\cos(\eta d) + i \frac{\eta}{d} \sin(\eta d) \right) \quad 2.30 \text{ a}$$

$$C_2 = \frac{1}{2} B_2 e^{-i\rho d} \left(\sin(\eta d) + i \frac{\eta}{d} \cos(\eta d) \right) \quad 2.30 \text{ b}$$

with $D_1=C_1^*$ and $D_2=C_2^*$, $d=h/2$, and from normalization of the power P , B_1 and B_2 become:

$$B_1^2 = \frac{2\omega\mu P}{\pi\beta \left(\cos^2(\eta d) + \frac{\sigma^2}{\rho^2} \sin^2(\eta d) \right)} \quad 2.31 \text{ a}$$

$$B_2^2 = \frac{2\omega\mu P}{\pi\beta \left(\sin^2(\eta d) + \frac{\sigma^2}{\rho^2} \cos^2(\eta d) \right)} \quad 2.32 \text{ b}$$

Under the assumption of infinite cladding thickness, the radiation modes have an oscillatory transversal profile inside and outside the core. As a result, energy confinement does not occur within a finite distance from the core but light propagates to the infinity, within the entire dimensions of the cladding regions. The assumption of infinite cladding dimensions together with the oscillatory character results in low energy values carried within the core when compared to the energy propagating within the claddings.

In practice, the cladding dimensions are always finite and this differentiates the real propagation behaviour of the radiation modes from theoretical expectations. In a LETFEL device the cladding thicknesses are limited to 3000Å. Beyond this point, is an opaque metal which is assumed to absorb the energy carried by the radiation modes. As a result, losses in a waveguide are directly related to the radiation modes.

Imperfections within a waveguide can induce coupling from guided modes into radiation modes and vice-versa which consequently subjects an imperfect waveguide to energy losses. A major source of imperfections within LETFEL waveguides is the surface roughness at the interface between the core and the cladding layers, which leads to scattering of the propagating light. A study of the propagation losses due to scattering has been performed and is detailed in the following section.

2.3 SCATTERING LOSSES

The effect of rough plane boundaries on wave light propagation has been studied in the past by several authors⁵³⁻⁵⁵. Particularly, in the work published by Marcuse⁵¹, the perturbation theory was applied to study the conversion efficiency from guided to radiation modes in a

slab waveguide due to surface roughness at the core-cladding interface. These results have been utilised in the present work as a method to determine the LETFEL attenuation constant due to interface roughness. In this study the conversion power from guided to radiation modes depends on the character of the surface roughness. As a result, the LETFEL core-cladding interface has been inspected and is described by a statistical treatment in the following section.

2.3.1 Statistical Description of Random Roughness

A rough surface can be defined as that which scatters the energy of an incident plane wave into various directions. The random rough surface is usually described in terms of its deviation from a smooth reference surface and by the correlation length⁵⁶. As illustrated in Figure 2.5, the surface can be represented by the function $h(z)$ where h is the height of the surface from the reference surface and z is the position vector on the reference surface.

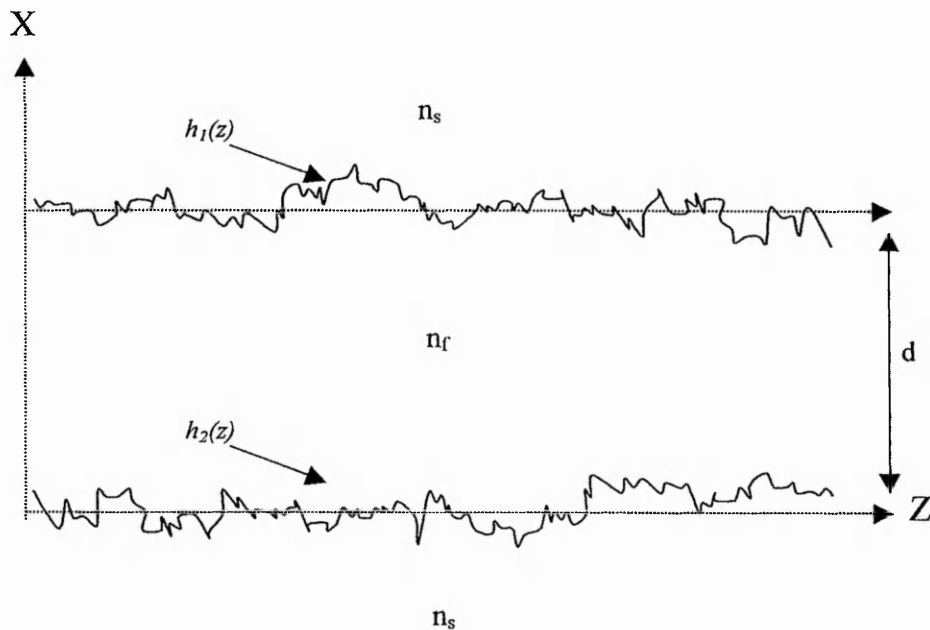


Figure 2.5 Surface roughness described as a function $h(z)$

The distribution of surface heights is described by the statistical height distribution, $p(h)$, where $p(h)\delta h$ is the probability of any surface point to be at a height between h and $h + \delta h$ away from the reference surface. Ensuring that $\langle h \rangle_s = 0$ is satisfied, the spatial average of heights can be defined as:

$$\langle h^2 \rangle_s = \int_{-\infty}^{+\infty} h^2 p(h) dh \quad 2.33$$

and the standard deviation, σ , can be consequently defined as the root mean square (rms) height of the surface:

$$\sigma = \sqrt{\langle h^2 \rangle_s} \quad 2.34$$

The other parameter which completes the description of a random rough surface is the correlation function, $C(Z)$, which is given by:

$$C(Z) = \frac{\langle h(z) \cdot h(z + Z) \rangle}{\sigma^2} \quad 2.35$$

For random surfaces, this is usually assumed to follow a Gaussian distribution given by:

$$C(Z) = e^{\left(-\frac{Z^2}{B^2}\right)} \quad 2.36$$

which decays to 0 as Z increases and the decay rate is dependent on the distance over which points become uncorrelated. The correlation length B is defined as the distance over which the correlation function, $C(Z)$, falls in amplitude by $1/e$.

From inspection of SEM figures, the values of the standard deviation, σ , and the correlation length, B , of the ZnS:Mn - Y_2O_3 interface were considered to be $\sigma=1 \mu\text{m}$ and $B=0.8 \mu\text{m}$.

2.3.2 Theoretical Study of the Mode Conversion from Guided to Radiation Modes due to Surface Roughness

An imperfect interface as illustrated in Figure 2.5 can be described by a variation of the refractive index as:

$$n^2(x, z) = n_0^2(x, z) + \Delta n^2(x, z) \quad 2.37$$

where

$$n_0^2(x, z) = \begin{cases} n_f^2 & |x| < d \\ n_s^2 & |x| > d \end{cases} \quad 2.38$$

and

$$\Delta n^2 = \begin{cases} \begin{cases} x < d & \text{if } d < f(z) \\ x < f(z) & \text{if } d > f(z) \\ x > f(z) & \text{if } d < f(z) \\ x > d & \text{if } d > f(z) \end{cases} \\ \begin{cases} -(n_f^2 - n_s^2) & f(z) < x < d & \text{if } d > f(z) \\ n_f^2 - n_s^2 & d < x < f(z) & \text{if } d < f(z) \end{cases} \end{cases} \quad 2.39$$

As a result, the wave Equation 2.16 can be expressed as:

$$\nabla^2 E_y + k_0^2 (n_0^2 + \Delta n^2) E_y = 0 \quad 2.40$$

and any field distribution which is solution of this equation can be described as the expansion presented in Equation 2.21, where $n=4$, the number of guided modes. Notice that the coefficients $C_v(z)$ and $C(v, z)$ are both functions of z which reflects the capacity of light coupling from guided to radiation modes during propagation.

Substituting Equation 2.21 into Equation 2.40 and through the various calculations⁵¹, the following differential equations for the coefficients $C_v(z)$ and $C(v, z)$ are obtained as:

$$\frac{\partial^2 C_v(z)}{\partial z^2} - 2i\beta_v \frac{\partial C_v(z)}{\partial z} = F_v(z) \quad 2.41$$

$$\frac{\partial^2 C(v,z)}{\partial z^2} - 2i\beta \frac{\partial C(v,z)}{\partial z} = G(v,z) \quad 2.42$$

with $F_v(z)$ and $G(v,z)$ given by the first order approximations:

$$F_v(z) = -\frac{\beta_v k^2}{2\omega \mu P} (n_f^2 - n_s^2) \left\{ \begin{array}{l} [h_1(z) - d] E_0(d,z) E_v^*(d,z) - \\ [h_2(z) + d] E_0(-d,z) E_v^*(-d,z) \end{array} \right\} \quad 2.43$$

$$G(v,z) = -\frac{\beta k^2}{2\omega \mu P} (n_f^2 - n_s^2) \left\{ \begin{array}{l} [h_1(z) - d] E^*(v,d,z) E_0(d,z) - \\ [h_2(z) + d] E^*(v,-d,z) E_0(-d,z) \end{array} \right\} \quad 2.44$$

The first order perturbation theory has been applied assuming $C_v(0)$ instead of $C_v(z)$ and $C(v,0)$ instead of $C(v,z)$. Both, $h_1(z)$ and $h_2(z)$ describe the top and bottom core-cladding interfaces which are assumed to be randomly distorted with no correlation between the distortions. In this case the mode conversion efficiency doubles the value obtained from only one wall being distorted. As a result and in order to simplify the discussion, the total mode conversion efficiency is obtained by doubling the mode conversion efficiency obtained under the assumption of $h^2(z)+d=0$.

Since solutions of Equations 2.41 and 2.42 contain waves travelling in the positive and negative z direction, the coefficients C_v and $C(v,z)$ can be described as:

$$C_v(z) = C_v^+(z) + C_v^-(z) \quad 2.45$$

$$C(v,z) = C^+(v,z) + C^-(v,z) \quad 2.46$$

being C_v^+ and $C^+(v,z)$ the coefficients associated to the waves travelling in the positive z direction and C_v^- and $C^-(v,z)$ the waves travelling in the negative z direction. Reference⁵¹ affirm that, ΔP , the power lost from the incident mode to radiation modes is given by:

$$\frac{\Delta P}{P} = \sum \int_0^{\infty} \left[|C^+(v, L)|^2 + |C^-(v, 0)|^2 \right] dv \quad 2.47$$

which states that the converted power is due to conversion from the incident mode in radiation modes travelling in the positive direction escaping at $z=L$, the end of the waveguide, and radiation modes travelling in the negative direction escaping at $z=0$.

From this, the power lost, ΔP_i of a guided mode, i , due to mode conversion into radiation modes due to a random rough interface is determined by the equation⁵¹:

$$\left(\frac{\Delta P}{P_0} \right)_i^{scat} = \frac{\sigma^2 k^4 l}{2\pi B} (n_f^2 - n_i^2)^2 \int \frac{n_i k}{-n_i k} \frac{\rho \cos^2 \kappa_i d}{((\beta_i - \beta)^2 + \frac{1}{B^2})(\beta_i d + \frac{\beta_i}{\gamma_i})} \left(\frac{\cos^2 \eta d}{\rho^2 \cos^2 \eta d + \eta^2 \sin^2 d} + \frac{\sin^2 \eta d}{\rho^2 \sin^2 \eta d + \eta^2 \cos^2 d} \right) d\beta \quad 2.48$$

where σ is the rms deviation of the interface from perfect flatness, B is the correlation length, l is the propagation length, k_0 is the wavelength vector module, n_f and n_s are the core and cladding refractive index respectively, β_i , γ_i and κ_i are the propagation constant, the extinction coefficient and the transverse vector for the four guided modes, β is the propagation constant of the radiation modes, d is half the thickness of the core layer and ρ and η are the radiation mode constants defined in Equation 2.29

The attenuation coefficient due to scattering, α^{scat} , can be described as:

$$\alpha_i^{scat} = \frac{-\ln \left(1 + \frac{\Delta P_i}{P_0} \right)}{l} \quad 2.49$$

The attenuation coefficient has been calculated making use of Equations 2.48 and 2.49 and using parameters listed in Table 2.1 for the LETFEL waveguide. This results in attenuation values of $\alpha_0=0.0039\text{dB } \mu\text{m}^{-1}$, $\alpha_1=0.0555\text{dB } \mu\text{m}^{-1}$, $\alpha_2=0.0649\text{dB } \mu\text{m}^{-1}$ and $\alpha_3=0.1477\text{dB } \mu\text{m}^{-1}$ from the fundamental mode to the mode 3 respectively.

The transmitted power, P_i , for each guided mode i , versus the propagation length, z , follows the exponential relation:

$$P_i = P_0^i e^{-\alpha_i^{scat} z} \quad 2.50$$

and this relation is graphically illustrated in Figure 2.6. From these results it may be concluded that the energy carried within the modes 1, 2 and 3 is highly attenuated when compared to the energy carried by the fundamental mode. Thus, the energy carried by modes 1, 2, and 3 is reduced to a $1/e$ of its initial value within distances of $25 \mu\text{m}$, $20 \mu\text{m}$ and $10 \mu\text{m}$ respectively while the fundamental mode is reduced to this value in the much longer distance of $150 \mu\text{m}$.

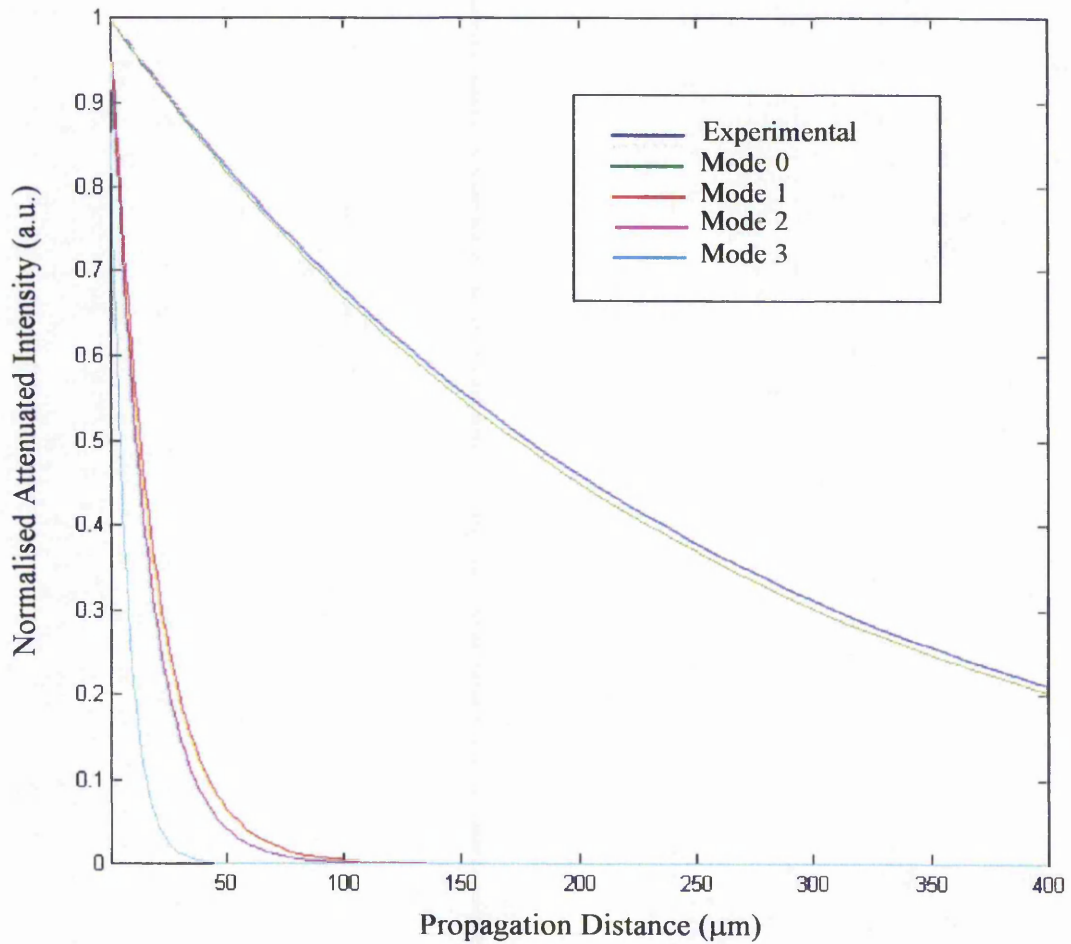


Figure 2.6 Power associated with each guided mode in a LETFEL waveguide after interface scattering, versus the propagation distance.

As a result, the attenuation undertaken by the light propagating within the LETFEL waveguide strongly depends on the percentage of energy carried by each guided mode. If the generated light couples principally into the fundamental mode, propagation will be subjected to significantly lower losses than if coupling occurs into higher order modes. Therefore, to determine the total attenuation undertaken by the light propagating within the LETFEL waveguide, information about the fraction of energy carried by each individual mode is required.

Figure 2.6 illustrates experimental results previously published⁴⁸ of the attenuation of the light propagating within the LETFEL waveguide versus the propagation length. In these experiments, the attenuation constant was determined from measurements of the edge-emitted light for different waveguide lengths. These data are therefore related to the attenuation undertaken by the total energy propagating within the waveguide.

Comparison of this experimental result with the theoretically determined attenuation demonstrates that the former coincides with the attenuation undertaken by the fundamental mode. This is a significant result which demonstrates that the fundamental mode is the main one responsible for energy transport in LETFEL waveguides. If higher order modes contributed to energy transport, the experimentally measured attenuation would be expected to be higher than the fundamental mode value. As a result, the energy coupled into higher order modes can be considered negligible. This result simplifies future theoretical study of the outcoupling process in LETFEL waveguides. Thus, the outcoupling theory presented in Chapter 3 has assumed that the generated light is totally coupled into the fundamental mode.

**THEORETICAL MODELLING OF THE
OUTCOUPLING PROCESS**

-
- 3.1 Introduction
 - 3.2 Outcoupling Mechanism of Conventional Non-Etched LETFEL Devices
 - 3.3 Outcoupling Mechanism of Abrupt Open End LETFEL Devices
 - 3.4 Theoretical Modelling of the Outcoupling Through a Smooth Abrupt End
 - 3.5 Conclusions
-

3.1 INTRODUCTION

Waveguide outcoupling can be defined as the process of energy conversion from a guided wave propagating within a guiding structure into an outgoing beam. The fraction of energy emitted from the waveguide is defined by the outcoupling efficiency.

The mechanism utilised for outcoupling is known as the waveguide coupler⁵⁷. Waveguide couplers can be divided into transverse or longitudinal couplers. Transverse couplers directly extract the propagating light through an exposed cross-section, while longitudinal couplers extract the incident light obliquely to the waveguide surface.

Usually, the coupler is selected after analysis of the character of the electromagnetic field and the required output characteristics. For the particular case of LETFEL waveguides, the electromagnetic field generated within the phosphor has been demonstrated to propagate as the fundamental mode. Additionally, the two most important light output characteristics are the emitted angular distribution and the degree of optical cross talk between emitting apertures. On one hand, the angular distribution should be a narrow profile centered perpendicular to the device surface. As discussed in Chapter 1, this optimises the coupling efficiency of the two main LETFEL applications which are HMDs and EP. On the other hand, the optical cross talk must be low in order to improve contrast. A successful outcoupler should consequently satisfy these requirements.

The choice of a suitable outcoupling mechanism is also determined by its fabrication feasibility. Since fabrication of optical couplers generally involves photolithography, deposition and etching technologies, a design which requires intricate structures and complicated routes is easily subjected to failure. This aspect of the outcoupling design is not intended to be studied in this chapter but will be analysed in future chapters.

The objective of this chapter is to theoretically determine the outcoupling process in LETFEL devices. The outcoupling mechanism of non-etched LETFEL devices is theoretically analysed and a study of the limitations of this technique is provided. Subsequently, two alternative outcouplers are proposed and the light output properties expected from theoretical modelling are detailed.

3.2 THE OUTCOUPLING MECHANISM OF CONVENTIONAL NON-ETCHED LETFEL DEVICES

This section presents a theoretical study of the outcoupling mechanism of conventional non-etched LETFEL devices. This study has been performed under the assumption that outcoupling occurs at the aperture regions as a result of:

1. surface roughness
2. waveguide bending

As illustrated in Figure 3.1, the SiO_2 microstructures underlying the LETFEL thin films at the aperture regions curve the waveguide and enlarge the distance of propagation along the aperture. The former generates energy coupling due to bend radiation losses and the latter enhances the scattering losses due to surface roughness.

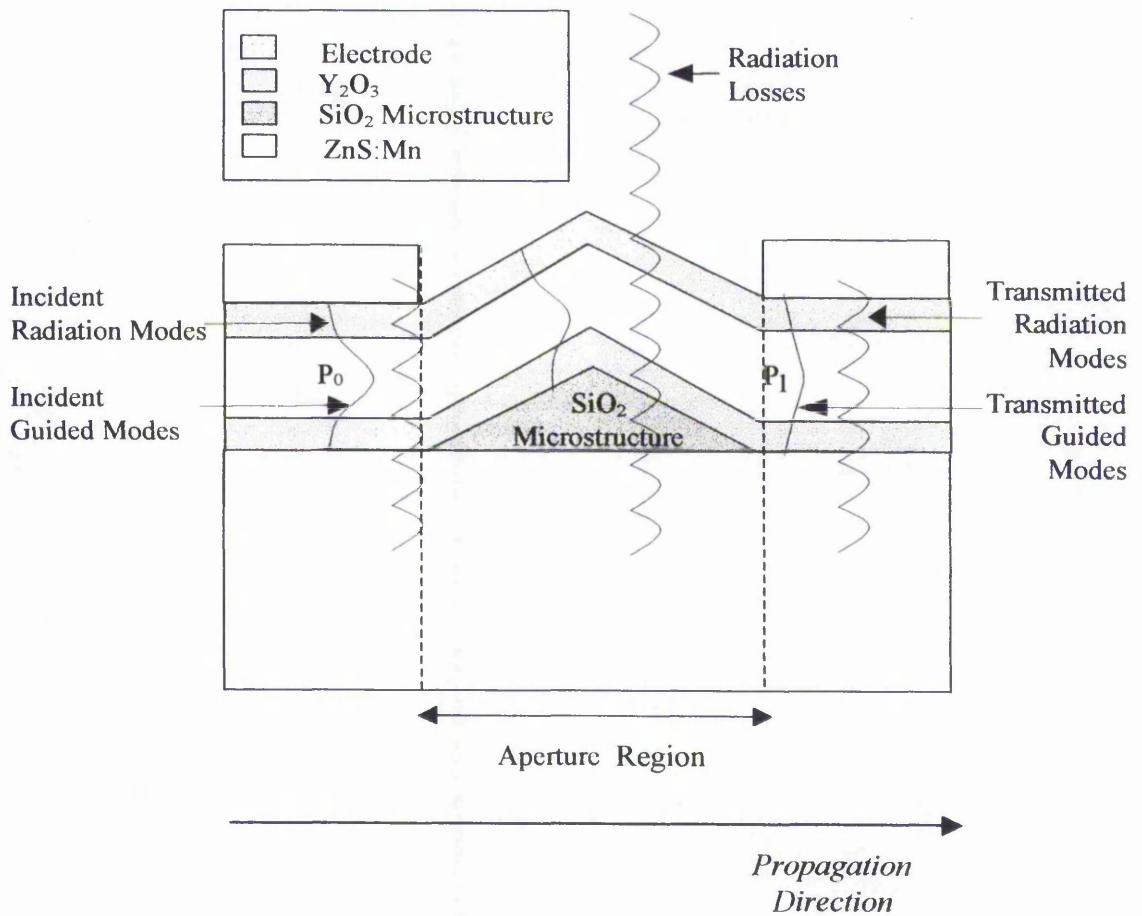


Figure 3.1 Cross section of a conventional non-etched LETFEL device

To analyse the outcoupling efficiency, the coupling power from guided to radiation modes due to surface roughness and waveguide bending has been studied. The light generated within the waveguide has been assumed to totally couple to the fundamental mode from the results presented in Chapter 2. The light coupled into radiation modes has been considered to be lost to the outside of the waveguide and to contribute to the outcoupled light.

Sections 3.2.1 and 3.2.2 present a theoretical prediction of the outcoupling efficiency due to surface roughness and waveguide bending.

3.2.1 The Effect of Surface Roughness on the Outcoupling Efficiency

The outcoupling efficiency of conventional non-etched LETFEL devices is partly derived from the mode conversion efficiency from guided to radiation modes due to surface roughness at the interface between Y_2O_3 and ZnS:Mn. Whereas surface roughness has been demonstrated to be detrimental for light waveguiding in LETFEL devices, it contributes to the outcoupling efficiency.

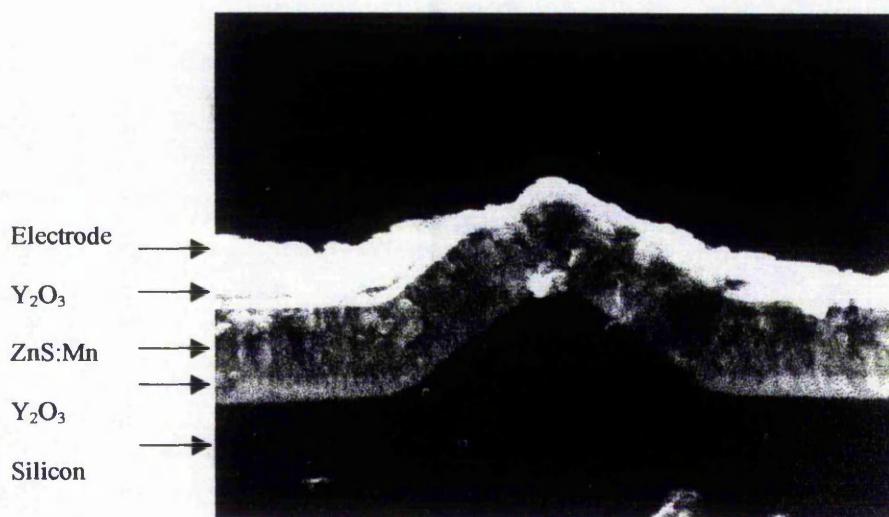


Figure 3.2 SEM photography illustrating a typical cross section of a conventional non-etched LETFEL device outcoupling aperture

Along the active length, the energy carried by the radiation modes is considered to be absorbed by the overlying opaque metal electrode. However, this electrode is removed at the aperture regions which in turns permits energy to be radiated to the outside. This contributes to the total outcoupled radiation.

To calculate the power lost, L , due to surface roughness at the aperture region, let P_0 be the power reaching the aperture as illustrated in Figure 3.1 and P_1 , the transmitted power at a distance l . As a result, $L=(1-P_1/P_0) \cdot 100$ can be defined as the percentage of power lost in a distance l . From the SEM picture illustrated in Figure 3.2, the core thickness along the bend can be considered constant and as a result, the power transmitted versus the propagating distance along the device aperture can be described according to Equation 2.50.

Typical LETFEL aperture sizes are within the order of a few microns. An aperture width of $10 \mu\text{m}$ is sufficient to clearly show the losses introduced by surface scattering within the LETFEL waveguide. Based on Equation 2.50, the losses introduced to the energy carried by the fundamental to the mode 3 respectively are:

$$L_0 = 4\% \qquad L_1 = 43\% \qquad L_2 = 48\% \qquad L_3 = 77\%$$

This demonstrates that a very high percentage of the energy carried by the mode 3 is converted into radiation modes within the selected aperture length. Lower order modes acquire lower attenuation values and a very small percentage of the light carried by the fundamental mode is converted to radiation modes within the aperture dimensions.

Since the energy carried by modes 1, 2 and 3 can be consider negligible when compared with the fundamental mode, the losses introduced by surface roughness at the aperture can be approximated to the losses undertaken by the fundamental mode. Consequently, only 4% of the energy reaching a $10 \mu\text{m}$ aperture is coupled out due to surface roughness.

Figure 3.3 illustrates the transmitted power versus the propagation distance, l , for the energy carried by the fundamental mode. It can be observed that aperture sizes within the order of $150 \mu\text{m}$ are required to obtain significant outcoupling efficiency values of approximately $1/e$ the initial power.

Unfortunately, such aperture dimensions are too large for the resolution values required for LETFEL devices (~500 dpi). As a result, it may be concluded that surface roughness is not an efficient mechanism to outcouple the light generated in LETFEL devices since the device apertures have small sizes to maintain the required resolution values.

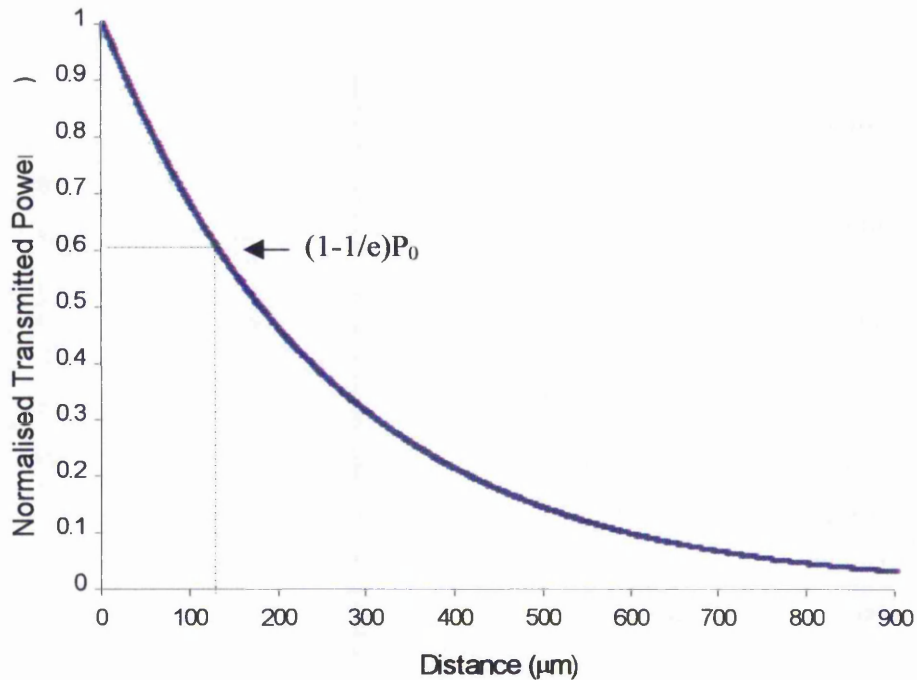


Figure 3.3 Attenuation of the Fundamental Mode due to Surface Roughness

3.2.2 The Effect of Bend Radiation Losses on the Outcoupling Efficiency

Modal guidance within a straight dielectric waveguide can be affected by the introduction of directional changes in the propagation path^{58,59}. These changes can provoke energy conversion from guided to radiation modes, the latter introducing radiation losses to the guided light.

As illustrated in Figure 3.2, non-etched LETFEL devices benefit from waveguide directional changes by incorporating microstructures, with 1.5 µm high and 45° wall sided triangular cross-sections, underlying the thin films at the aperture locations. The microstructures curve the waveguide and consequently introduce a change on the straight directional character. As a

result, radiation losses are generated which contribute to the outcoupling efficiency of the device.

A way of understanding the radiation losses generated due to waveguide bending is provided by Marcatili studies⁶⁰ where the dissipative loss generated due to conversion from guided to radiation modes is analysed. This study assumes an arbitrary profile of a guided mode travelling through a bend in a waveguide as illustrated in Figure 3.4. The evanescent tail decays exponentially until infinite distances in the x direction within the cladding regions. The energy in the evanescent tail must travel at different velocities to maintain the equiphase front through the bend with radius R. The longer the distance from the center of the waveguide the higher the speed. For some distance $X > R + X_r$, this velocity must exceed the light speed and as a result the fraction of energy contained at $X > R + X_r$ is not any longer guided but is assumed to be radiated.

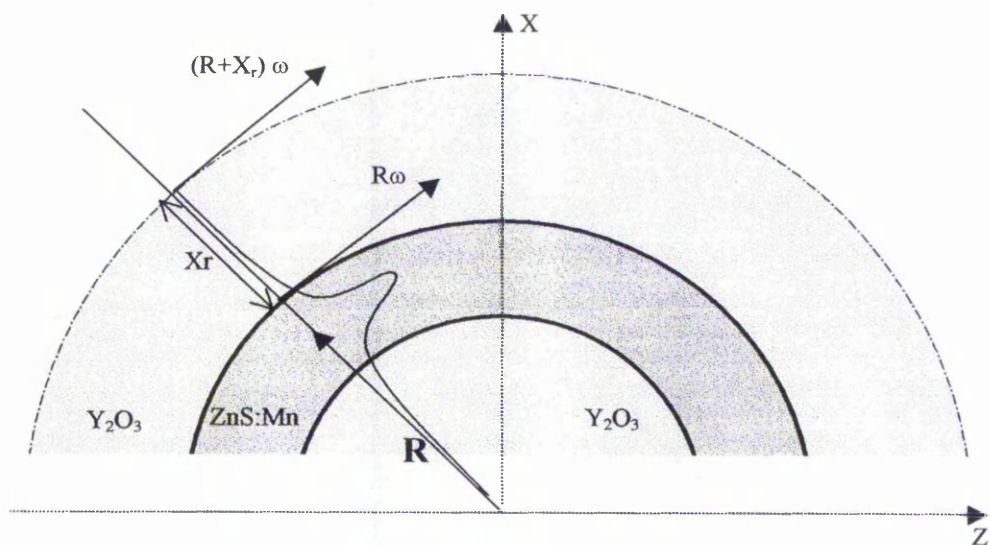


Figure 3.4 Attenuation due to Bend Radiation Losses

The threshold value, X_r , can be determined from the tangential velocity expressions before and beyond X_r as:

$$V_R = R \frac{d\theta}{dt} = \frac{\omega}{\beta} \quad 3.1$$

$$V_{R+X_r} = (R + X_r) \frac{d\theta}{dt} = \frac{\omega}{k_0} \quad 3.2$$

where R is the radius of the circular bend, β is the propagation constant of the guided mode within the waveguide and k_0 is the wavevector module for unguided light outside the core. Therefore:

$$X_r = \frac{\beta - k_0}{k_0} R \quad 3.3$$

Note that although the energy propagating in the bend beyond $R+X_r$ becomes unguided it remains collimated within a given distance in the near-field region along the propagation direction. This distance can be approximated by the value Z_c ⁶¹ as:

$$Z_c = \frac{h^2}{2\lambda_s} \quad 3.4$$

where h is the transverse field width within the waveguide and λ_s the wavelength in the medium. Z_c represents the distance from an abrupt open end of a waveguide along which the radiated beam remains collimated.

The fraction of energy lost in the bend per unit length can be quantified by the attenuation coefficient, α^{bend} , defined as:

$$\alpha^{\text{bend}} = \frac{-1}{P(z)} \frac{dP(z)}{dz} \quad 3.5$$

where z is the propagation distance and $P(z)$ the power transmitted at a distance z . If the lost power versus the total power is given by the ratio P_{lost}/P_T , where P_{lost} is the power propagating at distances $X > X_r$ and P_T is the total power, and under the assumption that the loss occurs for longitudinal distances higher than Z_c , the attenuation coefficient can be defined as⁶²:

$$\alpha^{bend} = \frac{1}{P_T} \frac{P_{lost}}{Z_c} \quad 3.6$$

Considering the electric field expressions for the symmetric waveguide given in Equations 2.22, P_{lost} and P_T can be calculated as:

$$P_{lost} = \int_{x_r}^{\infty} E_y^2(x) dx = \frac{E_0}{2\gamma_i} \cos^2(\kappa_i h / 2) e^{-2\gamma_i(x_r - \frac{h}{2})} \quad 3.7$$

$$P_T = \int_{-\infty}^{\infty} E_y^2(x) dx = E_0 \left[\frac{h}{2} + \frac{1}{2\kappa_i} \sin(\kappa_i h) + \frac{1}{\gamma_i} \cos^2\left(\frac{\kappa_i h}{2}\right) \right] \quad 3.8$$

where κ_i and γ_i are the transverse vector and the extinction coefficient of the guided modes for each mode $i=0,1,2,3$, h is the core thickness, E_0 is the field amplitude. The attenuation constant in a bend results in:

$$\alpha_i^{bend} = \frac{\frac{1}{2} \cos^2\left(\frac{\kappa_i \times h}{2}\right) \exp\left(\frac{-2\gamma_i R(\beta_i - k_0)}{k_0}\right) 2\lambda_0 e^{h\gamma}}{\gamma_i h^2 \left[\frac{h}{2} + \frac{\sin(\kappa_i \times h)}{2\kappa_i} + \frac{1}{\gamma_i} \cos^2\left(\frac{\kappa_i \times h}{2}\right) \right]} \quad 3.9$$

where λ_0 is the light wavelength in the medium surrounding the waveguide and R the radius of the bend.

From this expression the attenuation coefficient related to the guided modes in a LETFEL waveguide can be calculated. The wavelength is $\lambda_0=0.585 \mu\text{m}$, $k_0=10.74 \mu\text{m}^{-1}$ and the γ_i and κ_i values are included in Table 2.1. The radius of the bend has been extracted from the SEM picture presented in Figure 3.2. This illustrates the typical bend radius dimensions to be $R = 0.9 \mu\text{m}$.

Substituting these values in Equation 3.9, the attenuation coefficients result: $\alpha_0^{bend} = 3.5869 \cdot 10^{-13} \mu\text{m}^{-1}$, $\alpha_1^{bend} = 1.7229 \cdot 10^{-11} \mu\text{m}^{-1}$, $\alpha_2^{bend} = 6.0007 \cdot 10^{-9} \mu\text{m}^{-1}$ and $\alpha_3^{bend} = 1.7229 \cdot 10^{-5} \mu\text{m}^{-1}$ and expressed in units of $\text{dB}\mu\text{m}^{-1}$ are: $\alpha_0^{bend} = 15.89 \cdot 10^{-13} \text{dB}\mu\text{m}^{-1}$, $\alpha_1^{bend} = 7.63 \cdot 10^{-11} \text{dB}\mu\text{m}^{-1}$, $\alpha_2^{bend} = 26.58 \cdot 10^{-9} \text{dB}\mu\text{m}^{-1}$ and $\alpha_3^{bend} = 7.63 \cdot 10^{-5} \text{dB}\mu\text{m}^{-1}$.

As the fundamental mode is assumed to carry the entire propagating energy, the total losses due to radiation at the bend can be approximated by the losses of the fundamental mode. As a result, the radiation losses due to directional changes can be described by the attenuation constant value of $15.89 \cdot 10^{-6} \text{ dB}\mu\text{m}^{-1}$. This value is small and can be considered negligible when compared with the attenuation constant value of $0.0039 \text{ dB}\mu\text{m}^{-1}$ obtained for surface roughness.

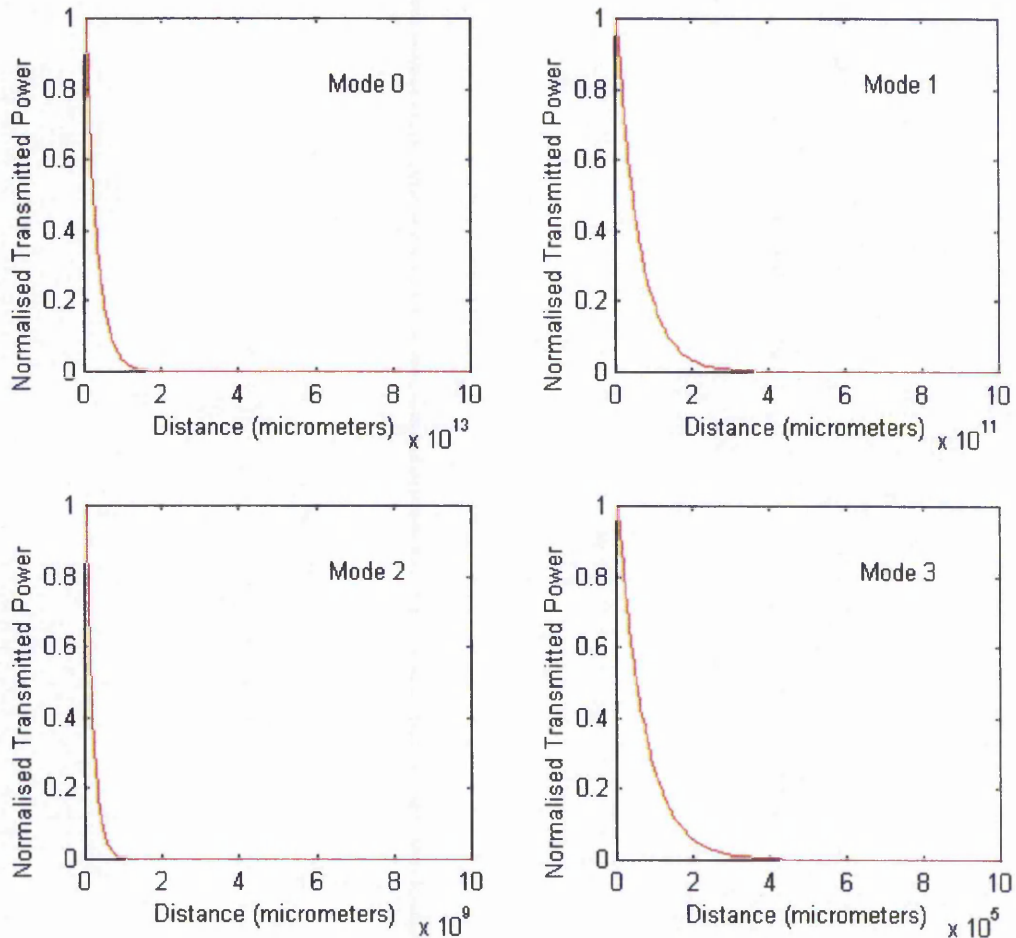


Figure 3.5 Power transmitted after undergoing attenuation due to bend radiation losses

The exponential relation between the transmitted power due to bend radiation losses and the propagation distance can be obtained from Equation 2.50 and is illustrated in Figure 3.5. It can be observed that although the attenuation loss increases with the propagating length, very long distances are required to achieve a significant loss. As an example, it can be determined

from the data in Figure 3.5 that attenuation losses of the order of $1/e$ times the incident power require the bend to extend for distances of the order of 10^{13} μm .

3.2.3 Conclusions: Limitations of the Conventional non-etched LETFEL Devices

From the theoretical results presented in Sections 3.2.1 and 3.2.2 one can conclude that the outcoupling mechanism incorporated by conventional non-etched LETFEL devices provides poor efficiency values. Approximately 96 % of the waveguided light fails to outcouple through a $10\ \mu\text{m}$ aperture and is partially absorbed and partially waveguided beyond the aperture region contributing to the emission of neighbouring pixels. Surface roughness and waveguide bending are therefore insufficient to extract high fractions of the generated energy and do not eliminate cross talk between pixels. As a result, alternative mechanisms are proposed in the next section, which are included under the category of abrupt open-end LETFEL devices as a consequence of their aperture geometry.

3.3 OUTCOUPLING MECHANISM OF ABRUPT OPEN END LETFEL DEVICES

The outcoupling mechanism of abrupt open end LETFEL devices can be generally described as that of an abrupt open end waveguide which launches guided light into free space. As illustrated in Figure 3.6, this mechanism generates lateral emission which needs to be converted into surface emission. The process through which this is accomplished can vary depending on the outcoupling mechanism. In this work, two main mechanisms are proposed, the etched aperture and the surface emitting edge emitter.

Etched apertures and surface emitting edge emitters constitute two different methods to theoretically generate analogous light output characteristics. Both couple light through an open edge although they differ in the conversion method utilised from lateral to surface emission.

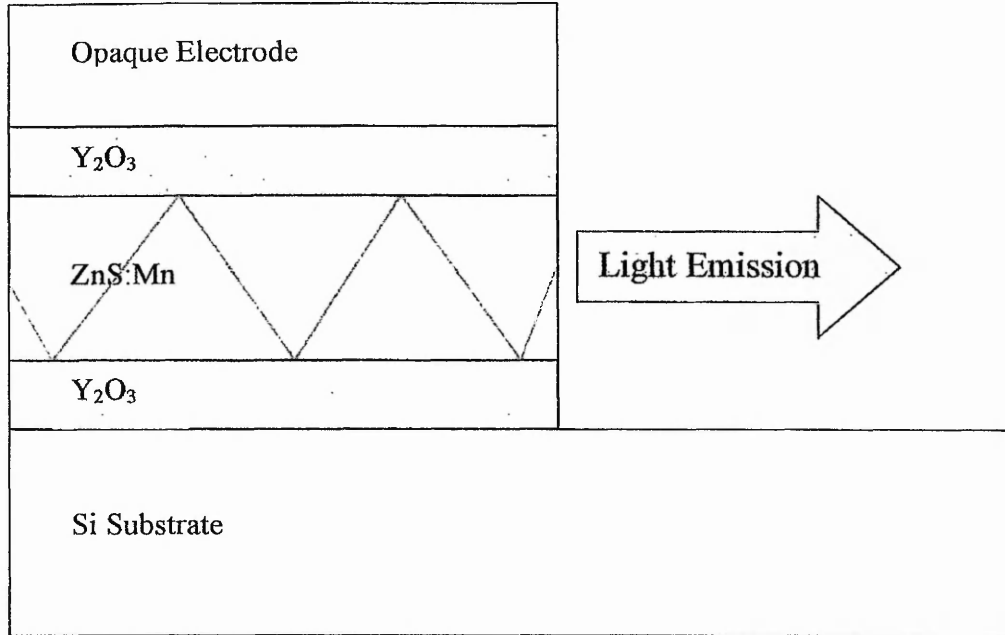


Figure 3.6 Open end launching guided light to the outside media

The etched aperture combines the abrupt open end with a micromirror structure as illustrated in Figure 3.7. The internally propagating light is coupled out through the edge emitter and subsequently converted into surface emission via reflection with the micromirror. Distortion and losses of the incoming profile can occur due to mirror imperfections and transmission of the light through this beyond the aperture regions.

The alternative mechanism, the surface emitting edge emitter, combines bending and edge faceting of the waveguide structure as illustrated in Figure 3.8. Light propagates along the bend with low attenuation as demonstrated in the Section 3.2 and is subsequently emitted through the edge perpendicularly to the surface

The light output characteristics of these devices has been generally determined by modelling of the inner light outcoupling through a smooth edge. This modelling has been performed according to the results obtained in Chapter 2 which demonstrate light generated within the phosphor layer couples and propagates as the fundamental mode within the structure.

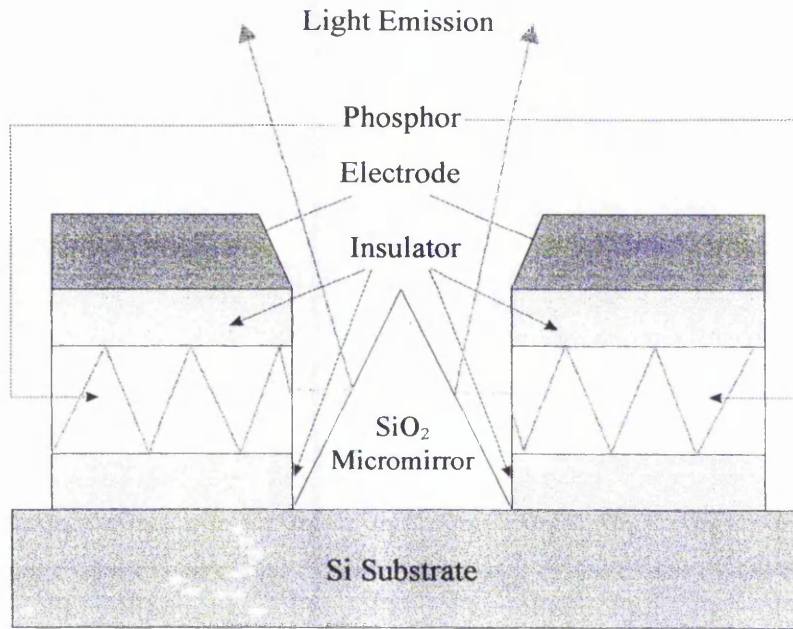


Figure 3.7 Etched Aperture LETFEL Device

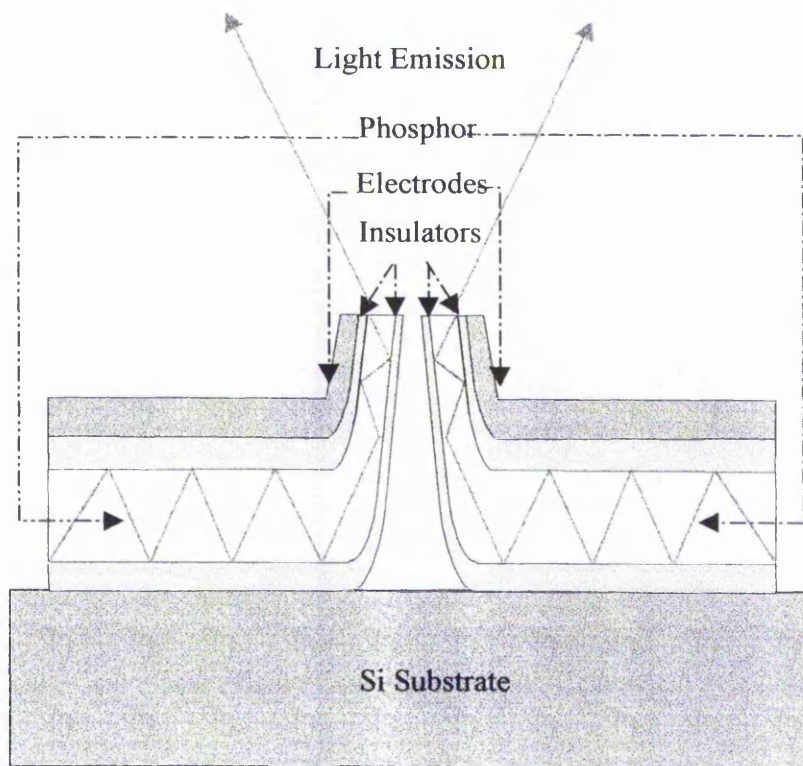


Figure 3.8 Surface Emitting Edge Emitter

The light guided within the waveguide diverges once outside in the free propagation media. To determine the spatial profile after the light distribution has passed through the abrupt open end, the internal spatial profile is expanded as a superposition of plane waves making use of the Fourier Transform. These are subsequently propagated through the waveguide edge considering the Fresnel equations and the Snell law which defines the refracted angles. Using the inverse Fourier Transform, the spatial profile outside the waveguide is obtained from superposition of the transmitted plane waves.

3.4 THEORETICAL MODELLING OF THE OUTCOUPLING THROUGH A SMOOTH ABRUPT END

The Gaussian distribution from Equation 3.10 has been selected to represent the normalised transversal profile of the fundamental mode propagating within the LETFEL waveguide:

$$E_y(x) = e^{-x^2/x_0^2} \quad 3.10$$

with characteristic width $x_0=0.3536 \mu\text{m}$. Both, the transverse profile and the Gaussian distribution are graphically represented in Figure 3.9,

A periodic spatial profile can be generally described as a Fourier series expansion given by:

$$E_y(x) = \sum_{n=-\infty}^{+\infty} E_y(n) e^{i2\pi n k_0 x} \quad 3.11$$

where k_x is the x component of the wavenumber k and $E_y(k_x)$ is given by:

$$E_y(n) = \frac{1}{T} \int_{-\frac{T}{2}}^{\frac{T}{2}} E_y(x) e^{-i2\pi n k_0 x} dx \quad 3.12$$

being T the period of the function.

This describes a function as the superposition of a finite number of plane waves with weighted amplitudes. Each plane wave component propagates in a different direction and has a different phase and amplitude which is represented by the complex number $E_y(k_x)$.

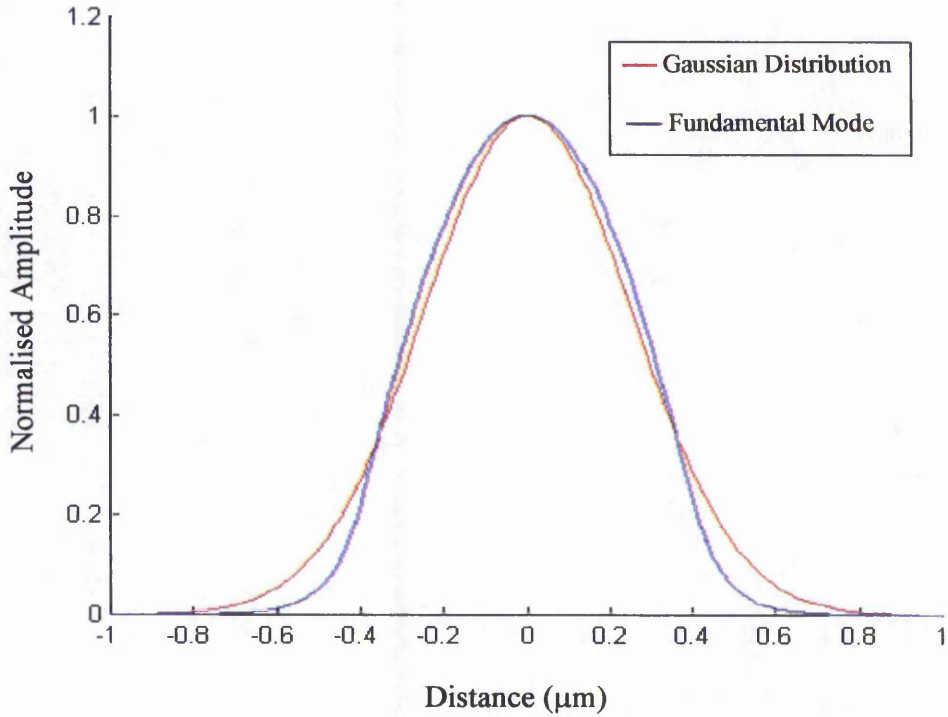


Figure 3.9 Fundamental mode transverse profile and fitting Gaussian distribution

The equivalent form for sampled data is obtained from the Discrete Fourier Transform (DFT) expressions. The DFT of a N-point array, E_s , is given by⁵²:

$$E_s = \frac{1}{\sqrt{N}} \sum_{r=1}^N E_r e^{i2\pi(s-1)(r-1)/N} \quad 3.13$$

which is another N-point array, E_r , where E_s and E_r are the N-numbers describing the spatial amplitude and the amplitude and phase of each plane wave respectively. The symbols r and s represent the data point index on the spatial and DFT domain respectively.

The DFT of the Gaussian distribution from Equation 3.10 was numerically calculated using Matlab. The profile was sampled and considered as if it repeated periodically in the spatial

domain. As a result, a limit to the sampled profile has to be introduced. This limit will be referred to as the sampling domain and it will be represented as D .

Figure 3.9 was initially inspected. The distribution decays asymptotically to zero extending to infinity and one can assume that the mode amplitude is negligible for distances beyond $0.6 \mu\text{m}$ from the core axis. Therefore a distance of $10 \mu\text{m}$ can be considered a safe choice for the sampling domain, D , and this was selected for the numerical calculations.

The x component of the wavevector associated with each plane wave is given by:

$$k_x = 2\pi(s - 1) / D \quad 3.14$$

where D is the limit of the spatial domain.

The Gaussian profile was sampled at 300 equally spaced points from $-5 \mu\text{m}$ to $+5 \mu\text{m}$ as illustrated in Figure 3.10a), and the DFT of the 300 point array was calculated and provided a 300 point complex array according to Equation 3.13. The real part represents the amplitude of the plane waves and is illustrated versus the array index s in Figure 3.10. It can be observed that the magnitude is high for very low and very large values of the s index however, the magnitude is negligible for s indices in the middle region. Values of s higher than 150, for instance $s-1=299$, represent the complex conjugated of $s-1=1$. Therefore the term $s=299$ corresponds to $s=-1$. Therefore very high and very low values of s represent small k_x values. The former generates planewaves travelling with a positive inclination and the latter with a negative inclination.

Thus, since:

$$k_x = \sqrt{k^2 - k_z^2} \quad 3.15$$

only plane waves travelling at small angles with the z direction contribute to the spatial profile.

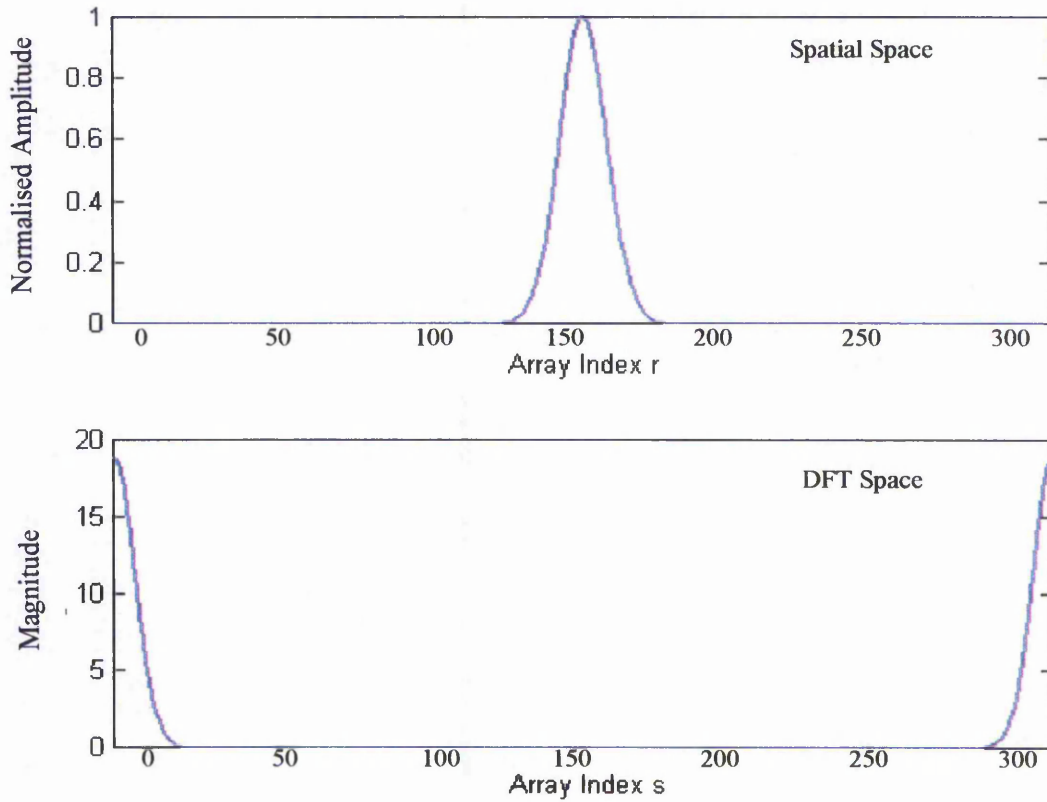


Figure 3.10 a) Sampled Profile of the Gaussian distribution propagating within the waveguide b) DFT of the Gaussian distribution represented in Figure 3.10a

The plane waves comprising the spatial profile have to be propagated across the open end and beyond it in the external media. This is achieved by inserting in the expression of each plane wave the appropriate phaseshift. The open end affects the incident plane wave in two ways: on one hand it varies the transmission angle according to Snell law and on the other hand it limits the transmitted energy according to the Fresnel equations⁶³.

In relation to the former, bear in mind that the angle of propagation of each plane wave respect to the axis z , is given by:

$$\theta_i = \arcsin\left(\frac{k_x}{n_f k_0}\right) \quad 3.16$$

where $k_0 = 2\pi/\lambda$. Therefore the Snell law can be applied to each propagating plane wave at the interface so that the transmitted angle is determined by:

$$\theta_t = \arcsin\left(\frac{n_f}{n_{air}} \sin\theta_i\right) \quad 3.17$$

In relation to the latter, the transmittance T_s was calculated in order to determine the fraction of energy transmitted to the outside⁶³ where:

$$T_s = \left(\frac{n_{air} \cos\theta_t}{n_f \cos\theta_i}\right)^2 \quad 3.18$$

and t is the refraction coefficient given by Fresnel equations.

After the plane wave is transmitted through the open end it propagates in the outside space. The phaseshift acquired by a plane wave travelling a distance l is given by:

$$\varphi_s = \frac{nk_0 l}{\cos\theta_t} = nk_0 l \left[1 + \frac{k_x^2}{2r^2 k_0^2}\right] = nk_0 l \left[1 + \frac{\lambda^2}{2D^2} (s-1)^2\right] \quad 3.19$$

As a result, the total phase, φ_t , of the plane wave after crossing the open end and travelling a distance l in the air is given by the expression:

$$\varphi_t = \varphi_s + \text{Angle}(E_y(k)) \quad 3.20$$

where $\text{Angle}(E_y(k))$ represents the phase of the planewave before propagation. The final plane wave expression is given by:

$$E_y^{out}(k) = T \cdot \text{Magnitude}(E_y(k)) e^{i\varphi_t} \quad 3.21$$

From this expression, the resultant spatial profile emitted from the waveguide edge can be calculated using the inverse Fourier Transform:

$$E_y^{out}(x) = \frac{1}{2\pi} \int_{-\infty}^{\infty} E_y(k_x) e^{ik_x x} dk_x$$

3.22

Figure 3.11 illustrates the final spatial profile for different distances $L=1, 2$ and $5 \mu\text{m}$, from the open end.

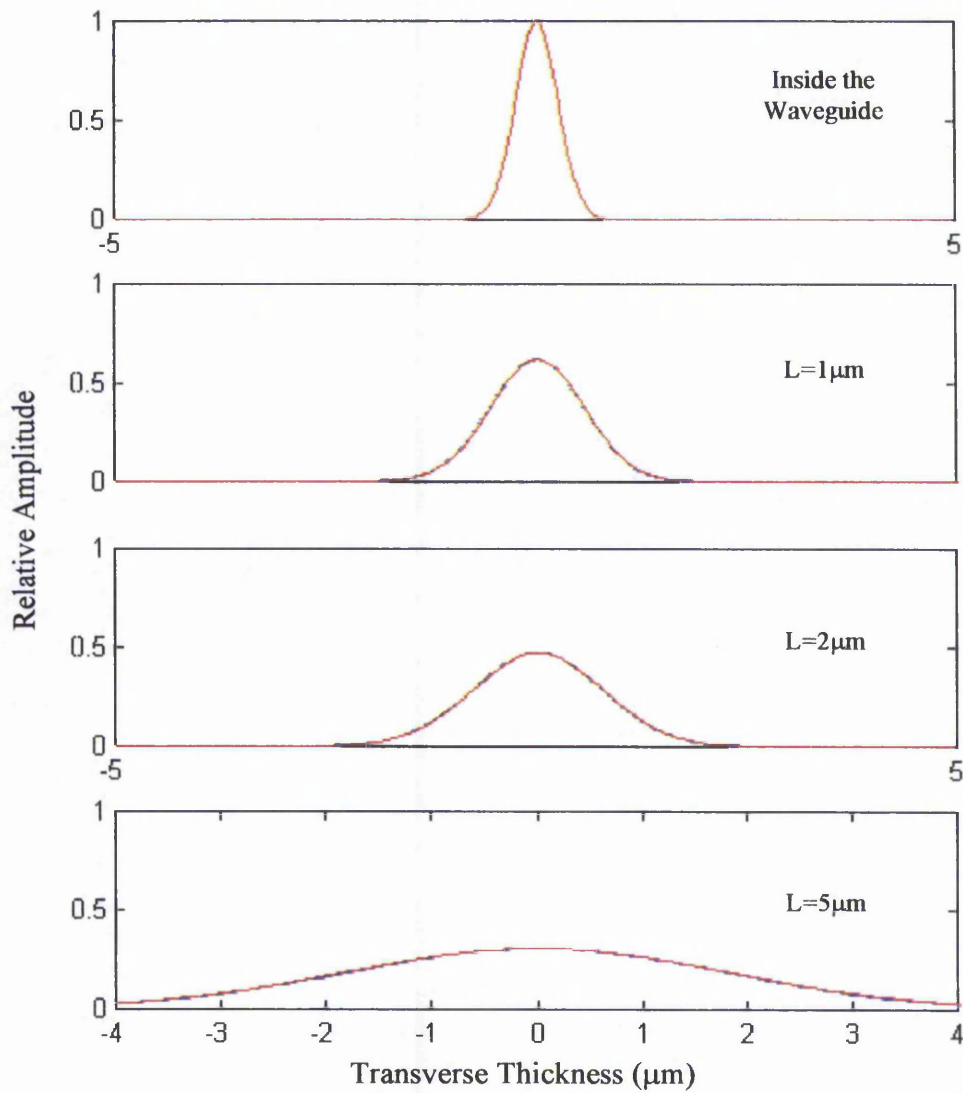


Figure 3.11 Spatial profiles at different propagation lengths

It can be observed how the Gaussian distribution diverges with the distance. This figure also illustrates the following Gaussian distributions:

$$E_{gauss}^1 = e^{-0.48-2.5x^2} \quad 3.23$$

$$E_{gauss}^2 = e^{-0.75-0.85x^2} \quad 3.24$$

$$E_{gauss}^5 = e^{-1.18-0.15x^2} \quad 3.25$$

which have been determined to fit each spatial profile.

Evaluation of these profiles provides the angular divergence of the outcoupled electromagnetic field in the free propagation media. This is represented in Figure 3.12 and corresponds to a Gaussian distribution with characteristic width $x_0=24^\circ$. Comparison of this result with the experimental data are provided in Chapter 6.

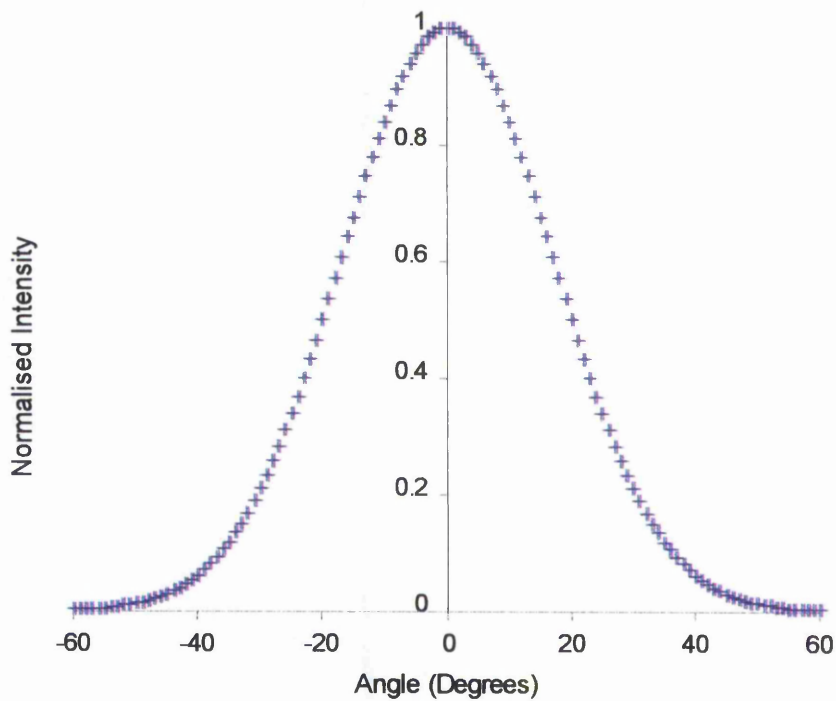


Figure 3.12 Angular Divergence of the Emitted Light

3.5 CONCLUSIONS

Conventional non-etched LETFEL devices incorporate a longitudinal outcoupling mechanism where light is coupled to the outside media via surface roughness and bend radiation losses. From the theoretical modelling, a low outcoupling efficiency of the order of 4% of the internally generated light has been determined for an aperture width of 10 μm . As a result, two novel mechanisms are proposed, the etched aperture and the surface emitting edge emitter, which constitute transverse outcouplers to the LETFEL waveguide. Both mechanisms are classified under the common group of abrupt open end devices since both incorporate an abrupt open end launching the guided light to the outside. A model of this outcoupling process has been accomplished using Fourier Transform of the spatial profile. This study provided the angular divergence of the emitted field to be a Gaussian distribution with a characteristic width of 24° .

EXPERIMENTAL DETAIL

-
- 4.1 Device Fabrication and Characterisation Overview
 - 4.2 Fabrication of the SiO₂ Microstructures
 - 4.3 Thin Film Deposition
 - 4.4 Thin Film Patterning
 - 4.5 Shaping the Device Aperture using Ion Milling
 - 4.6 Device Characterisation
 - 4.7 Conclusions
-

4.1 DEVICE FABRICATION AND CHARACTERISATION OVERVIEW

The process of LETFEL device fabrication involves a wide range of technologies for patterning and thin film deposition⁶⁴. The use of vacuum systems, typically located in clean rooms, is generally required and leads to high production costs and limitation of the device size to the dimensions of the equipment. High resolution technologies, capable to resolve pattern sizes less than 1 μ m, are particularly desired for fabrication of LETFEL devices. This limits the range of suitable technologies and further increases the production cost.

In this section the process route utilised for the fabrication of LETFEL devices is provided as well as an overview of the operating mechanism of the applied technologies and associated systems. Initially, the fabrication route consisted of three main stages⁶⁵:

1. Fabrication of 45° SiO₂ microstructures on the Si substrate
2. Deposition of the thin film stack
3. Thin film patterning of the top electrode using photoresist

This generated the non-etched conventional LETFEL devices introduced in Chapter 3 and restricted the production of alternative outcoupling mechanisms leading to potential enhancement of device brightness⁴⁷.

In this research a more elaborated route which allows reshaping of the device aperture is proposed in an attempt to increase the device brightness. This route has been successfully developed as part of this work and consists of the following four main stages:

1. Fabrication of 45° SiO₂ microstructures on the Si substrates
2. Deposition of the thin film stack
3. Thin film patterning including deposition of dielectric materials
4. Shaping the thin films at the aperture regions using ion milling

Stages 1 and 2 are identical to the initial route however, the incorporation of stages 3 and 4 required a thorough study of the technologies and materials to be used. This study is presented in this chapter along with the results of the calibration performed of the effect of the selected technologies on the device structure and associated materials.

Figure 4.1 represents the sequential steps leading to the fabrication of a LETFEL device according to the four stage fabrication route previously presented. Below is a brief description of the route and the processes involved in each stage.

Stage 1 Fabrication of SiO₂ microstructures on the Si substrates: Figure 4.1.1

The process commences at Figure 4.1.1 with cleaning of a 100 mm n+ Si wafer and deposition and etch of the SiO₂ microstructures at the aperture regions, by Plasma Enhanced Chemically Vapour Deposition (PECVD) and Reactive Ion Etch (RIE) respectively.

Stage 2 Thin Film Deposition: Figure 4.1.[2-5]

The following four steps represented in Figure 4.1.[2-5] constitute the deposition of the electroluminescent thin films. This section starts with the consecutive deposition of a 3000 Å Y₂O₃, an 8000 Å ZnS:Mn and a 3000 Å Y₂O₃ layer using rf magnetron sputtering. To conclude the deposition stage, 1500Å / 2500 Å / 1500Å of TiW/ Al/TiW electrode is DC sputtered on the top Y₂O₃ thin film.

Stage 3 Thin Film Patterning: Figure 4.1.[6-11]

This stage starts with the deposition of a 2 µm SiO₂ mask by PECVD. Patterning of the top electrode and the dielectric coating is then required to enable light emission at the aperture locations. This is achieved by means of high resolution photolithography and RIE which allows removal of both the electrode and the SiO₂ layers at the aperture locations.

Stage 4 Shaping the Thin Films at the Aperture Regions using Ion Milling: Figure 4.1.12

The last stage involves partial or total ion milling of the Y₂O₃ and ZnS:Mn thin films leading to the formation of the desired aperture. The aperture geometry depends on the ion milling conditions and an arbitrary shape is illustrated in Figure 4.1.12.

The fabrication processes involved in every stage are explained in more detail below, including descriptions of the equipment, the operating mechanisms and the applied process conditions.

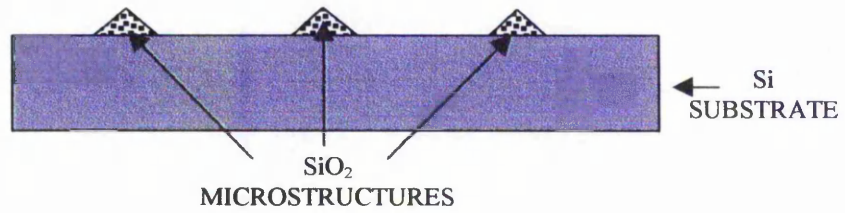


Figure 4.1.1 Step 1: Fabrication of SiO₂ Microstructures on Si

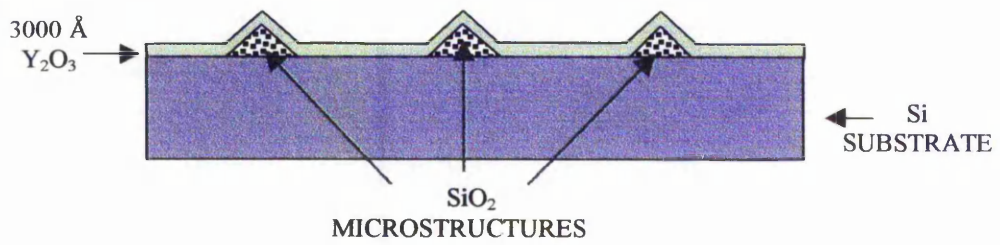


Figure 4.1.2 Step 2: Deposition of the Bottom 3000Å Y₂O₃ using rf Magnetron Sputtering

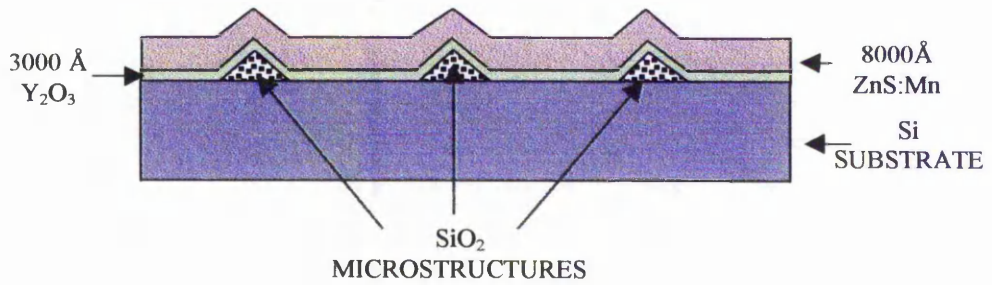


Figure 4.1.3 Step 3: Deposition of 8000Å of ZnS:Mn using RF Magnetron Sputtering

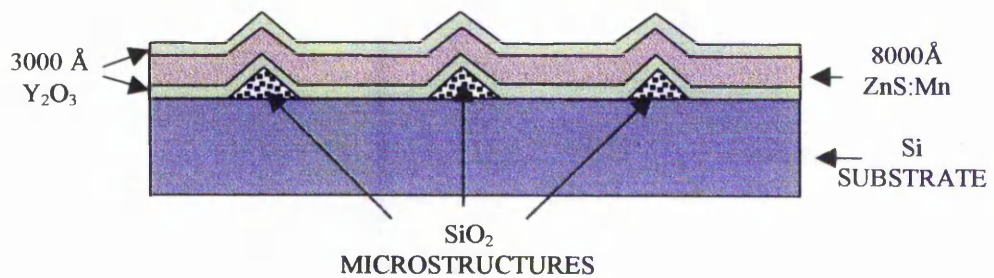


Figure 4.1.4 Step 4: Deposition of the Top 3000Å Y₂O₃ Using rf Magnetron Sputtering

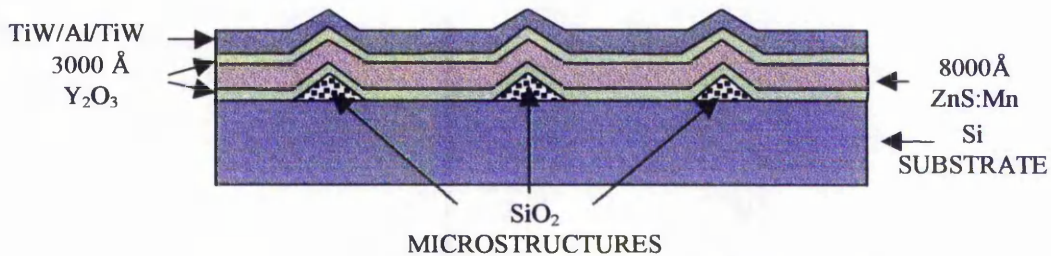


Figure 4.1.5 Step 5: Deposition of the [2500/1500/2500] Å TiW/Al/TiW Electrode using DC sputtering

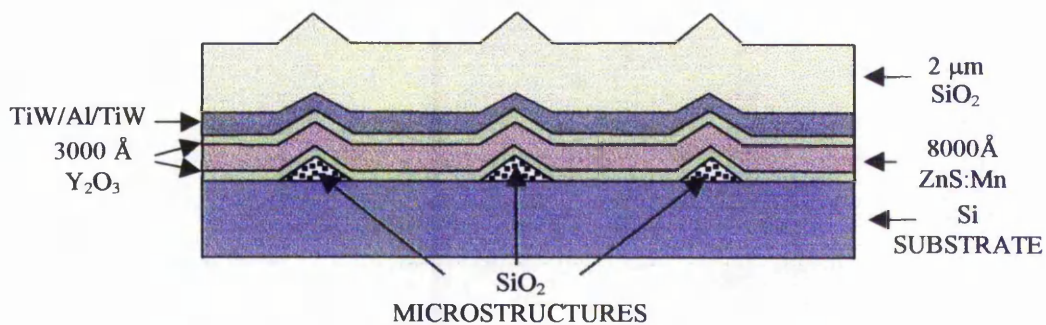


Figure 4.1.6 Step 6 : Deposition of the SiO₂ Mask using PECVD

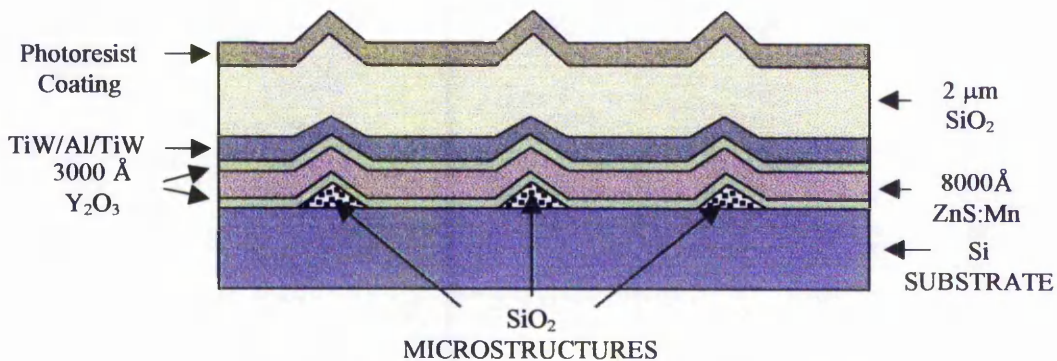


Figure 4.1.7 Step 7: Spinning of the Photoresist Coating

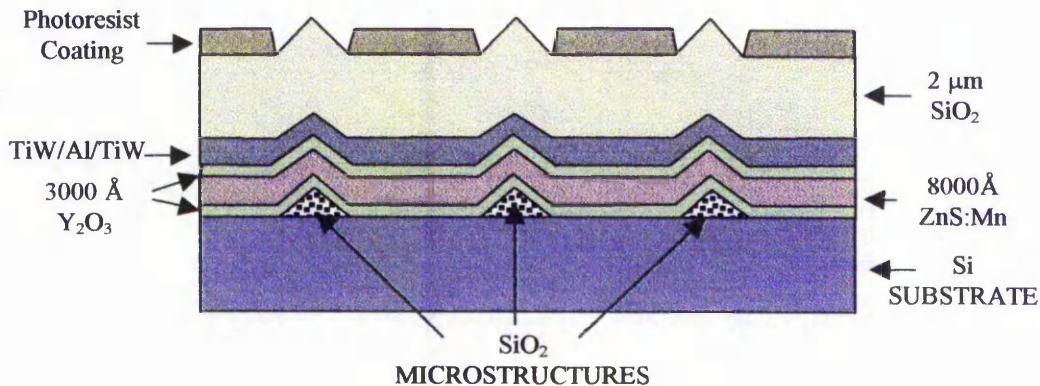


Figure 4.1.8 Step 8: Exposure and Development of Photoresist

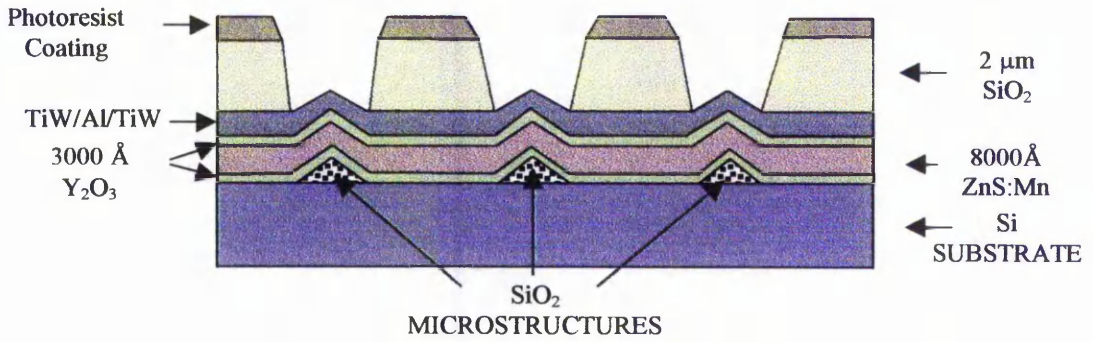


Figure 4.1.9 Step 9: Etching of the Dielectric Mask using RIE

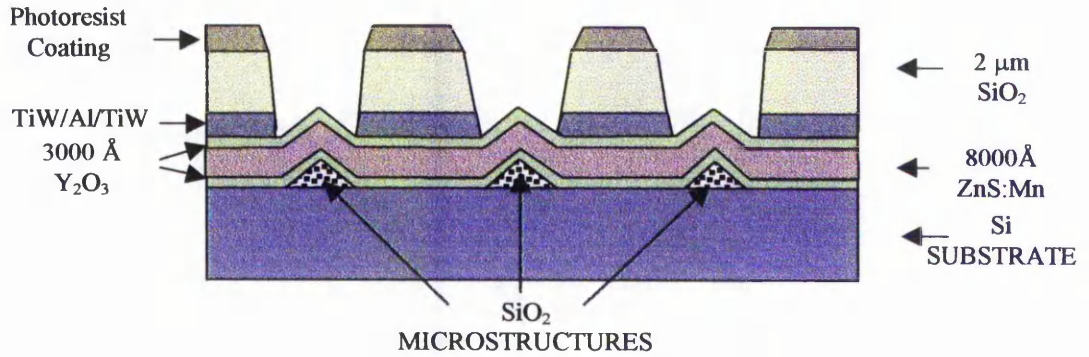


Figure 4.1.10 Step 10: Etching of the TiW/Al/TiW Electrode using RIE

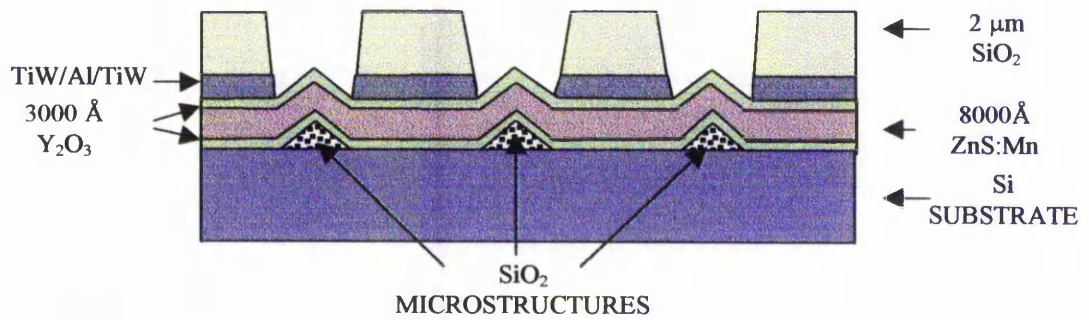


Figure 4.1.11 Step 11: Removal of the Unetched Photoresist

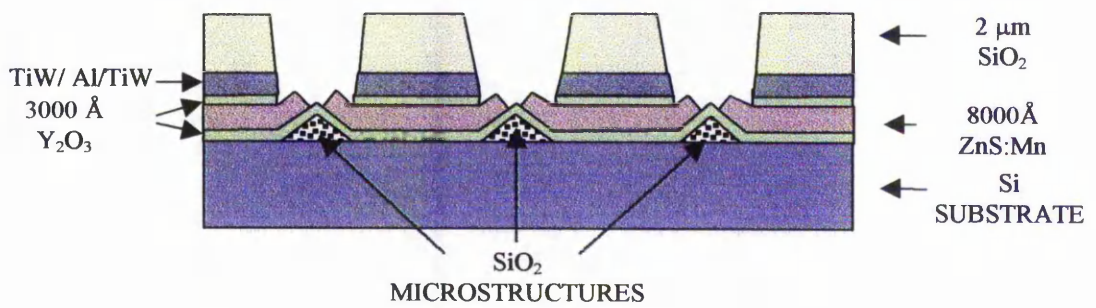


Figure 4.1.12 Step 12: Shaping of the Device Aperture using IM

4.2 FABRICATION OF THE SiO₂ MICROSTRUCTURES

LETFEL devices incorporate SiO₂ microstructures underlying the thin films at the aperture locations which lead to enhancement of the device outcoupling efficiency. These microstructures have been fabricated by NMRC at Cork, Ireland, according to the following route:

1. Deposition of SiO₂ thin film on Si by PECVD.
2. Photoresist masking of the SiO₂ thin film accomplished by coating of the thin film with photoresist, UV illumination of the photoresist through an adequate mask and developing of the resist.
3. Etching of the SiO₂ thin film by RIE in Ar and CHF₃.
4. Removal of the photoresist in an O₂ plasma.

NMRC provided n+ Si wafers coated with polyhedron geometries with different base shapes and 45° wall sided triangular cross sections with a width of 3 μm and a height of 1.5 μm. The entire range of devices studied in this research have been fabricated on these substrates.

Etched devices are advantageous with 45° wall side micromirrors however, surface emitting edge emitter devices require vertical walls to provide an optimised angular profile. In this work surface emitting edge emitter devices have been exclusively fabricated on 45° microstructures since the main aim of the present research is limited to:

1. Demonstrate the feasibility of fabrication of apertures incorporating surface emitters
2. Study of the light output characteristics and comparison with other technologies

Surface emitting edge emitters on 45° microstructures have permitted comparison of the brightness measured from the various outcoupling mechanisms developed. It has also allowed comparison with the theoretical results presented in Chapter 3. The fabrication of adequate vertical wall microstructures is left as future work.

4.3 THIN FILM DEPOSITION

As previously discussed, the fabrication of LETFEL devices involves various deposition technologies. Y_2O_3 and ZnS:Mn are usually deposited by rf magnetron sputtering. The process utilised in the deposition of the TiW / Al / TiW electrode is DC sputtering and the deposition technology applied for the dielectric thin films is PECVD. Below, general background on the technologies involved and the particular deposition conditions utilised for the fabrication are detailed.

4.3.1 Magnetron sputtering

In sputter deposition⁶⁶, the term sputter refers to the acceleration of ions towards a given target causing the emission of atoms from the target surface via momentum transfer. Sputter deposition starts with the conversion of a low pressure gas into a plasma by the application of an ionising electric field. This is applied between two electrodes, the lower electrode being the target plate and coupled to a power supply, and the top electrode being connected to the chamber walls and grounded. The generated plasma consists of positive ions and electrons moving within the vacuum chamber driven by the applied voltage. Typically, high energy ions strike the target plate, the cathode of the system, where the material to be deposited is located. These sputter off both surface atoms, which are directed and deposited on the substrate, and secondary electrons which are redirected towards the plasma and contribute to ionise more neutral atoms.

In magnetron sputtering⁶⁶, a series of magnets incorporated behind the target create a magnetic field which contains the plasma electrons within a volume above the target. This method intends to enhance the ionisation efficiency which in turns increases the sputtering rate. The magnetic field also reduces damage to the substrate surface due to bombardment of electrons from the plasma.

Sputtering techniques range from DC sputtering which limits the use to conductive targets, to rf sputtering which can incorporate conductive or insulating targets.

4.3.2 DC Magnetron Sputtering

Figure 4.2 illustrates a diagram of a typical DC sputter system, particularly the Oxford Plasmalab System 400 utilised in this work for the deposition of the TiW /Al / TiW electrode, at RAL. The process begins with loading the wafer in the process chamber. The vacuum chamber is evacuated down to a base pressure of 10^{-6} Torr by a cryo pump and a given flow of Ar gas is injected. The process pressure is controlled by a gate valve fitted between the chamber and the cryo pump and is maintained at 5 mTorr. DC power is applied to the cathode which is the target plate while the chamber walls and the wafer table are grounded. An Ar plasma discharge is produced consisting of electrons and Ar^+ ions. The positive ions are accelerated towards the target and sputter off neutral atoms which are deposited on the substrate. By switching between the two metal targets, the three thin films are consecutively deposited without breaking the vacuum conditions. The process conditions are detailed in Table 4.1. Finally the chamber is vented and the wafer is unloaded.

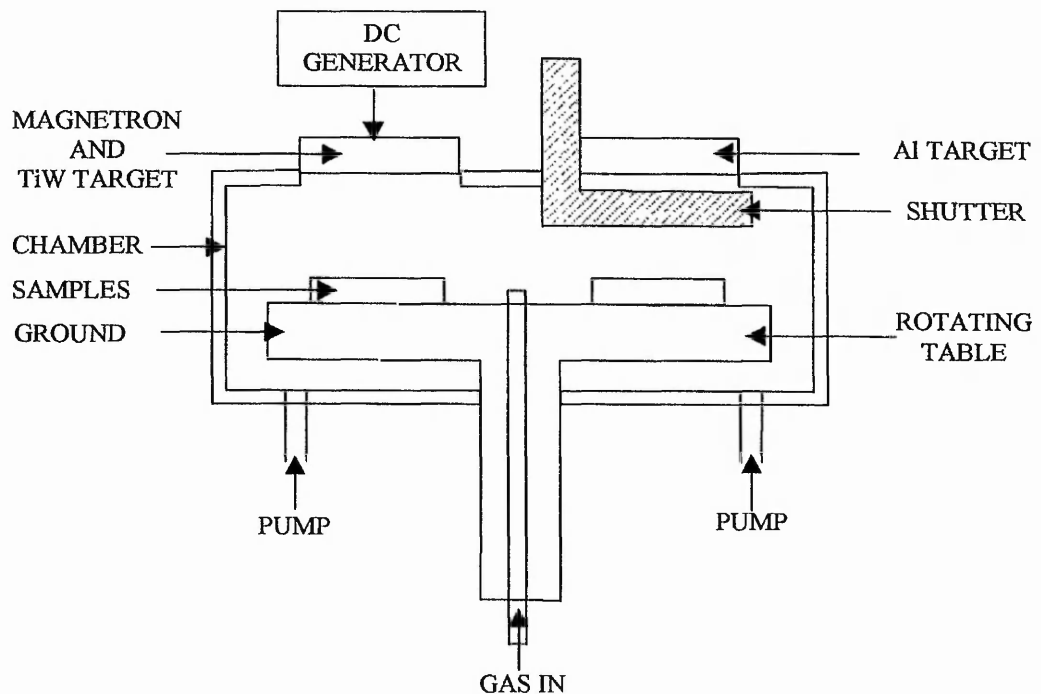


Figure 4.2 DC Magnetron Sputtering System

4.3.3 RF Magnetron Sputtering

A schematic diagram of the rf magnetron sputtering system used in the present work for the deposition of the Y_2O_3 and $ZnS:Mn$ thin films is illustrated in Figure 4.3. The wafer is loaded onto the substrate plate and the vacuum chamber is initially pumped down to very low pressures of the order of 10^{-7} Torr. Ar gas is injected into the chamber and the pressure is increased and maintained in the order of 10^{-3} Torr using a gate valve. An rf power electric field with operating frequency in the range of 13.6 MHz is applied to the magnetron target or bottom electrode. The top electrode is connected to the chamber walls and grounded.

DC Sputter Deposition Rates					
	Rate (Å/min)	Power (Watts)	Pressure (mTorr)	Gas	Flow (sccm)
AL	500	5000	5	Ar	10
TiW	200	2000	5	Ar	10

Reactive Ion Etch Rates						
	Rate (Å/min)	Power (Watts)	Pressure (mTorr)	SiCl ₄ (sccm)	CF ₄ (sccm)	O ₂ (sccm)
AL	200	160	70	40	---	---
TiW	600	120	70	---	40	10

Table 4.1 Al and TiW Deposition and Etch Rates

This system incorporates four different targets although only two are illustrated in Figure 4.3. These permit deposition of different materials without requirement of opening up the chamber. The shutters protect the targets when not in use. As a result of the applied AC signal, the Ar gas turns into a plasma made off positive Ar^+ ions and electrons. Since the electrons are more mobile than the positive ions, the target plate which is an insulator becomes negatively charged and attracts high energy Ar^+ ions which sputter off surface atoms. These are then deposited onto the rotating substrate. A heater is placed behind it to control temperature during deposition.

- Y_2O_3 Process Conditions

3000Å rf magnetron sputtered Y_2O_3 thin films are incorporated as the top and bottom insulator layers in typical LETFEL devices. For deposition of these thin films, the substrate temperature was maintained at 200°C and a deposition rate of 857 Å/hour was achieved. A 75 mm diameter x 4 mm thick solid Y_2O_3 target from Cerac Ltd, was sputtered for 3.5 hours at 120 Watts. The other growth parameters were set to $1 \cdot 10^{-7}$ Torr base pressure, 3×10^{-3} Torr process pressure and 5 sccm Ar flow. The thin film thicknesses were monitored in situ using the interferometric technique detailed elsewhere⁶⁷.

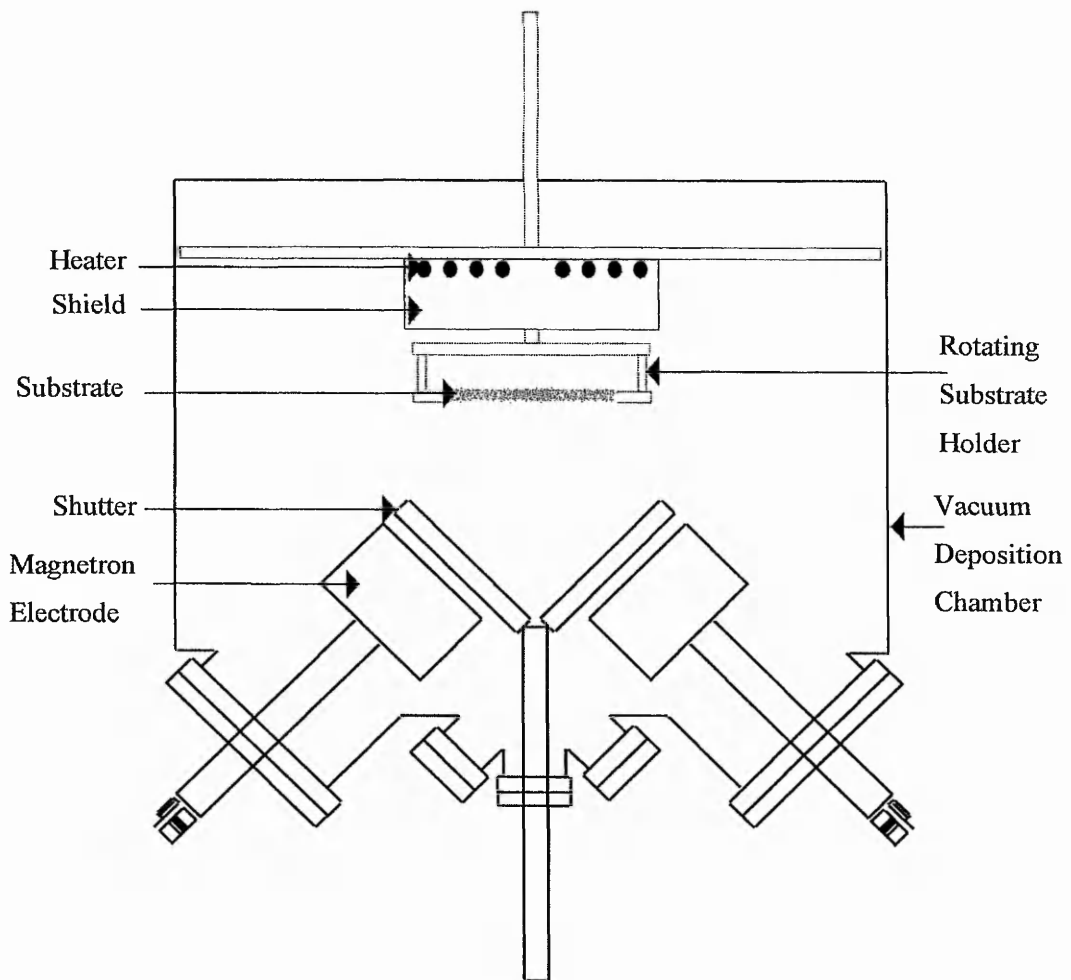


Figure 4.3 rf magnetron sputter deposition system

- ZnS:Mn Process Conditions

The 8000 Å ZnS:Mn thin films incorporated in typical LETFEL devices were sputtered in Ar at 200°C for 3 hours at a deposition rate of 2600 Å/hour. The Ar flow, the base and process pressures as well as the deposition temperature were identical to the Y₂O₃ deposition process. A 0.43 % wt of Mn in ZnS phosphor was cold pressed into a 75 mm diameter powder target for sputtering. The substrate was rotating continuously to ensure high deposition uniformity. A ± 5 % variation in thickness across the wafer was measured for a 100 mm diameter deposited thin film.

A post-annealing process of 1 hour in vacuum at 500°C was applied after deposition of the three films of bottom Y₂O₃, ZnS:Mn and top Y₂O₃.

4.3.4 Plasma Enhanced Chemical Vapour Deposition

Plasma Enhanced Chemical Vapour Deposition represents a method for chemical deposition of thin films at low temperature, normally within the range of 200°C to 300°C. Deposition is produced in a similar manner than in Chemical Vapour Deposition (CVD)⁶⁷ process. The main distinction is that PECVD utilises a plasma to couple electrical energy into the gas promoting chemical reactions.

The PECVD system utilised in this research consists of a parallel-plate electrode chamber as illustrated in Figure 4.4. The samples are placed on the substrate holder which is connected to the bottom electrode. The required gases enter at the center of the chamber which allows uniform spread over the wafer surface. The plasma is created between the top and bottom electrode following the application of an AC voltage. The neutral radicals as well as the plasma itself interact with the sample surface allowing the formation of a deposited layer.

In the present research, SiO₂, Si₃N₄ and SiO_xN_y thin films were deposited by PECVD using a Plasma Technology DP800 system available at the CMF at the RAL in Oxfordshire. The deposition chamber has capability for up to 8 wafers however, to increase uniformity in the thin film deposition a single wafer was loaded at a time. The Si substrate was placed onto a static target maintained at the constant temperature of 300°C. The chamber was initially pumped down to a base pressure of 10 mTorr and subsequently the gases were admitted to

the chamber. The process pressure was set to 300 mTorr and an AC power was applied. Once the thin films are deposited, the rf power is turned off and the vacuum chamber is vented. The wafers are then taken out the chamber and placed on a metal rail which conducts heat away allowing cooling of the substrate. The parameters utilised for deposition of the dielectric thin films are included in Table 4.2.

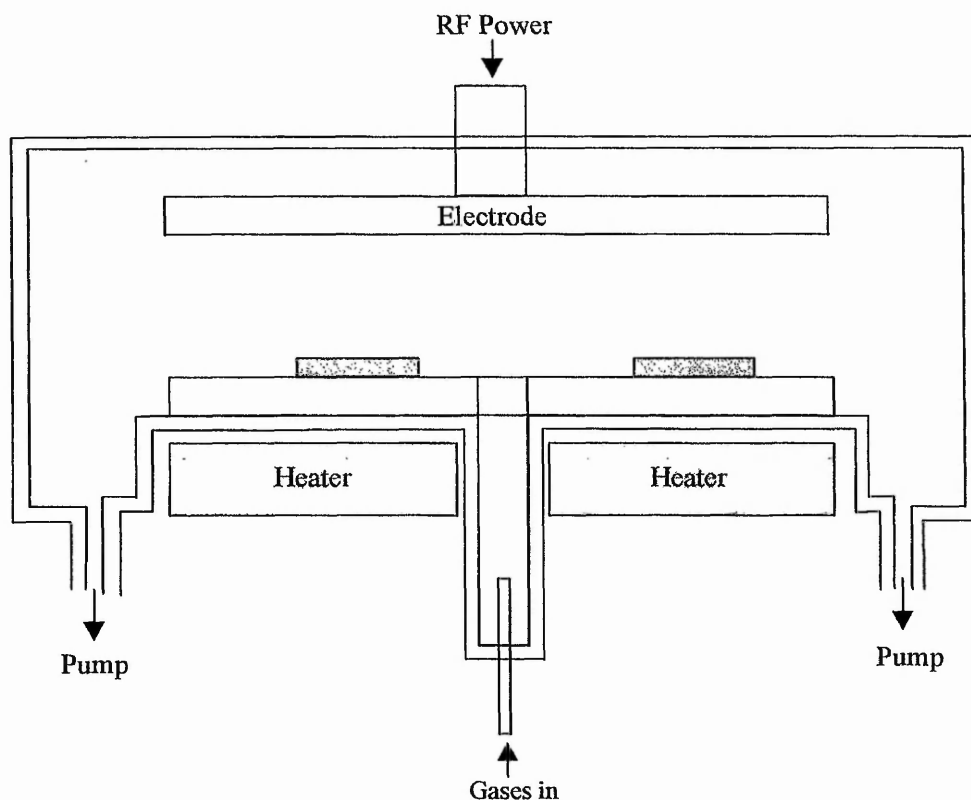


Figure 4.4 PECVD system utilised in the present research

	Si ₃ N ₄	SiO ₂	SiO _x N _y
<i>Gases</i>			
NH ₃ (sccm)	120	----	50
SiH ₄ (sccm)	19	7	15
N ₂ O (sccm)	----	200	160
Pressure (mTorr)	320	300	320
Power (Watts)	13	12	7
Temperature (°C)	300	300	300
Deposition Rate (Å/min)	67	181	180

Table 4.2 PECVD process parameters

4.4 THIN FILM PATTERNING

Thin film patterning⁶⁷ is a critical stage in LETFEL device fabrication since it determines the display geometry, pixel size and the resolution of the display. This provides coating of the thin films with masking materials on the areas where etching is not desired. The usual masking materials for high resolution thin film patterning are photoresists⁶⁸. These are organic polymers whose solubilities in certain solvents vary due to exposure to UV radiation. During the masking process, a photoresist layer is spun onto the thin film to be patterned and then is UV illuminated through a masking plate. This is a glass substrate where the desired pattern has been printed with an opaque material, for instance Cr. After illumination, the photoresist is developed. Since positive photoresists become more soluble in the developing solution in exposed areas and negative photoresists less, positive resists produce a positive image of the original pattern while an inverted image is produced by negative resists. Positive resists also provide higher resolving power than negatives although negative are normally tougher and can be utilised in more rigorous etching conditions.

Photoresists, as a result of their selective solubility with UV light exposure, are suitable masking materials which permit masking of thin films without the use of etching techniques. However, in processes with high temperature requirements, photoresists can be damaged and might need to be substituted by dielectric or metal masks. These materials require a more complex masking process which becomes an etching process itself. Premasking of the dielectric or metal films with photoresist is initially required, followed by patterning of the thin films using etching. In the present work both conventional photoresist and dielectric coatings have been utilised as masking materials and this section includes an overview to the associated technology. The process of dielectric masking can be divided in 6 main steps:

1. Deposition of the dielectric coating onto the thin film
2. Spinning of the photoresist onto the dielectric coating
3. Exposure and development of the photoresist
4. Transfer of the photoresist pattern to the dielectric coating by etching
5. Photoresist removal
6. Transfer of the dielectric coating pattern to the underlying thin film by etching

Each of these steps is explained below in more detail as well as the fabrication technologies involved and process conditions required.

4.4.1 Step 1: Thin Film Deposition

Thin film patterning incorporating dielectric masks begins with the deposition of the dielectric material. In the present research, PECVD SiO₂ has been selected. A 2 μm layer of SiO₂ is deposited for 36 minutes by PECVD using the Plasma Technology DP800 System as detailed in Table 4.2.

4.4.2 Step 2: Photoresist Coating

The second stage in the thin film patterning is the coating of the dielectric thin film with photoresist. In this work, conventional positive photoresist *Dynalith OFPR 800 cps 23*, has been used. The photoresist is spun for 60 s at 5000 rpm onto the SiO₂ layer. Then it is soft baked for 2 minutes using a hot plate at 95°C. The coating is exposed at 350 mJ/cm² for 40 s using a Canon pla-500f mask aligner through a mask plate. This was designed using AutoCad software package and incorporates opaque features in Cr defining the pattern. Subsequently, the resist is developed in an AZ726MIF developer maintained at 21°C, constantly stirring for 90 minutes. The wafer is washed in deionised water and dried with nitrogen gas. Finally, the sample is hardbaked at 130°C for 1 hour.

The resultant photoresist step height is measured using the Tencor P-2 Long Scan profiler and typical thickness values of 1.1 μm ± 0.001 μm were obtained under the detailed conditions. This thickness has been found to be sufficient to accomplish etching of both the underlying SiO₂ and the TiW / Al / TiW thin films.

4.4.3 Step 3: Reactive Ion Etching

Transfer of the photoresist pattern to the dielectric mask has been produced by Reactive Ion Etching⁶⁹ (RIE). RIE combines chemical reactions and physical sputtering as part of the etching mechanism. It is an anisotropic dry technique which replicates the photoresist pattern onto the coated film with high precision in the vertical direction. RIE can also introduce high selectivity values which permit certain amount of overetch to be applied without damaging the pattern design.

Figure 4.5 illustrates a schematic drawing of the Oxford Plasmalab System 90 utilised for RIE, at RAL. The wafer is placed on a substrate plate. The chamber is pumped down to low pressures in the range of 10^{-4} Torr and the required gases are admitted in. A high-frequency (~ 13 MHz) power supply is connected to the substrate plate while the other electrode and the chamber walls are grounded. This results in a glow discharge which produces the reactive etchant or plasma between the two electrodes. The gas plasma results from breaking the bonds of the gas molecules into positive and negative ions, neutral atoms and radicals. The combination of neutral atoms and radicals produces chemical reactions and positive ion sputter on the surface resulting in volatile products. These compounds are diffused into the gas and pumped out by the vacuum system. An asymmetry in the plasma-electrode potential difference is produced since the ratio of target to chamber wall area is quite high. As a result, the substrate turns into the cathode and the chamber walls into the anode. This accelerates positive ions in a direction perpendicular to the substrates with minimal sputtering of the anode.

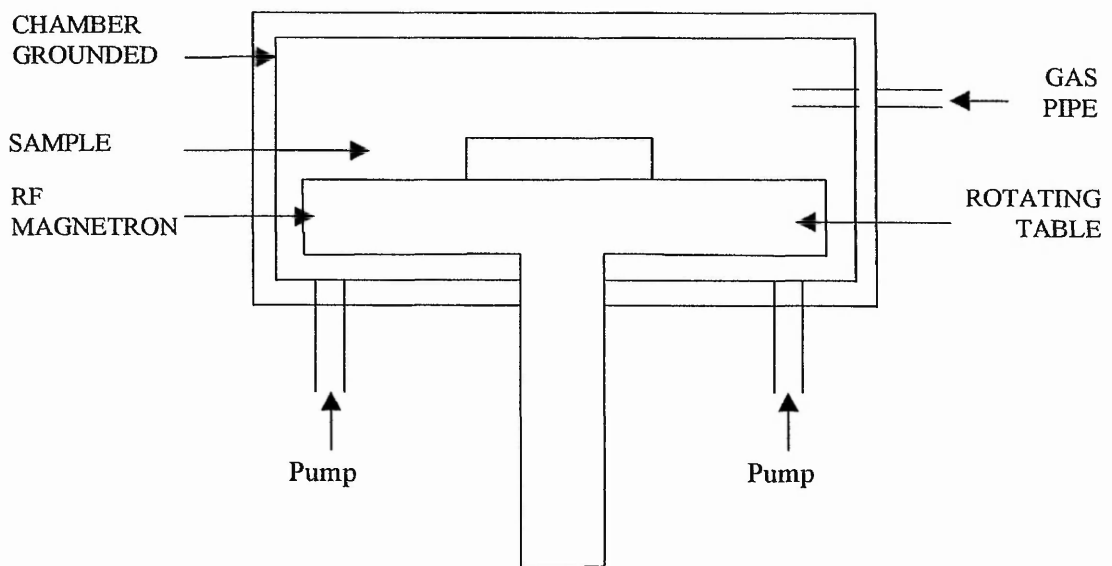


Figure 4.5 System used for the RIE process

- Etching of the Dielectric Mask using RIE

For RIE of SiO₂, 20 sccm of CHF₃ and 2 sccm of O₂ were injected into the chamber while the process pressure was maintained at 100 mTorr. 500 Watts were applied between the electrodes at room temperature. The SiO₂ and photoresist etch rates were determined to be 560 Å/min and 100 Å/min respectively. Under these conditions the aluminium etch-rate was under 5Å/min which generated high selectivity allowing overetching to ensure full patterning of the SiO₂ film. As a result, etching included a 25% overetch which led to a process time of 45 minutes.

- Etching of the TiW/Al/TiW Electrode using RIE

According to Figure 4.1, after RIE of the SiO₂ mask, the TiW / Al / TiW electrode is removed from the aperture locations. This process is accomplished by RIE immediately after etching of the SiO₂ layer, without breaking the vacuum, under the etching conditions detailed in Table 4.1. Although etching of the TiW/Al/TiW electrode is not part of the conventional masking process it is included in this section for this particular fabrication process.

4.4.5 Photoresist Removal

The last step in the thin film patterning is the removal of the unetched photoresist. This process requires high selectivity values between the photoresist and the underlying thin film etch-rates and is generally performed in an O₂ plasma. In the present work, a 35 sccm O₂ flow was injected into the vacuum chamber which was kept at a process pressure of 200 mTorr. Under the application of a 100 Watts power, the gas was turned into a plasma which was maintained for 8 minutes at an etch-rate of 100 Å /min. Full removal of the photoresist was determined by observation through an optical microscope.

4.5 SHAPING THE DEVICE APERTURE USING ION MILLING

4.5.1 Background

Ion milling^{70,71} is an impact and energy transfer sputter etch process where a collimated beam of high energy ions strikes a target and sputters off surface atoms. The ion energy is normally in the 200 eV to 1000 eV range, sufficient to break the forces bonding neighbour atoms, usually in the order of several eV.

The etch-rate depends on the ion beam density, the ion energy and the angle of incidence. These can be independently chosen so that different etch-rates are achieved for a given material. Generally, the etch-rate increases linearly with the ion beam density and at lower rates with the ion energy.

Although high ion beam powers produce high etch-rates, these also introduce high heat levels into the structure. To avoid possible damage, a cooling system is incorporated which conducts heat away from the substrate. However, when etching a substrate with a resist pattern, the maximum temperature limit is the upper temperature tolerated by the resist, around 150 °C. This represents a main limitation of the technique and can be overcome by reducing the ion beam power or by utilising masking materials with higher heat resistance.

Ion milling provides the etching technology with the ability of controlling the etched profile shape. This is achieved by varying the angle of incidence of the ion beam onto the sample.

4.5.2 Equipment

For the present work, thin films have been ion milled using a Veeco 10" Microetch System available at RAL. The milling chamber is shown schematically in Figure 4.6.

The system is evacuated from atmospheric pressure down to the range of 10^{-3} Torr using a mechanical pump. Subsequently, the cryo pump is turned on to reduce system pressure down to approximately 10^{-6} Torr. Ar gas is let into the chamber and an AC voltage is applied between a hot filament cathode emitting electrons and an anode which is the outer chamber wall. The Ar gas turns into a plasma and Ar^+ and electrons are generated as a result of the applied field as in typical sputtering techniques. Since the final ion current density depends

on the density of ions in the source plasma it can be controlled by varying the voltage applied between the hot filament cathode and the anode. A magnetic field is also applied inside the chamber using a solenoid so that the resultant radial electron path is longer, increasing the collision probability with a neutral Ar atom to produce an Ar^+ ion.

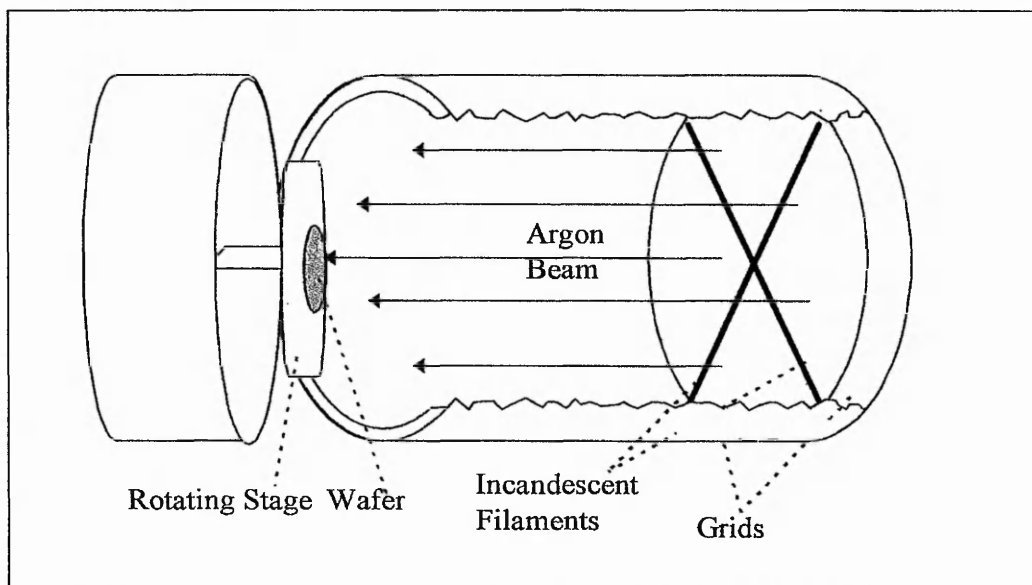


Figure 4.6 Ion Milling System

A collimated Ar^+ beam is extracted by applying a voltage between two metallic grids. The final ion beam energy depends on the strength of the applied voltage and can be varied for each etching process.

To avoid damage of the sample due to charge effects, the ionised beam is charge neutralised by an electron source emitted by a pair of incandescent filaments. These are drawn throughout the ion beam so that current to the substrates due to the positive ions is cancelled by the neutralising electrons.

The beam bombards a 10" diameter water-cooled rotating stage where the wafer is placed. To control the angle of incidence of the ion beam onto the substrate, the stage can be tilted while maintaining the direction of propagation of the beam constant.

A study of the effect of the ion milling conditions on LETFEL materials has been performed and the experimental details and results obtained are included in the following chapter.

4.6 DEVICE CHARACTERISATION

Following fabrication of LETFEL devices, light output properties, particularly the Light Intensity versus Voltage (LV) and the angular distribution, were measured utilising the measurement systems described below.

4.6.1.- Measurement of the Light Intensity versus Voltage Characteristic

The LV characteristic was determined using the systems illustrated in Figure 4.7. A metallic plate holds the wafer with micrometric movement in the horizontal plane and which is connected to a vacuum pump. When the pump is on, the wafer adheres to the plate tightly so that undesired movements are avoided. Additionally, this provides good contact of the Si substrate, which is the bottom electrode of the device, with the plate which is grounded.

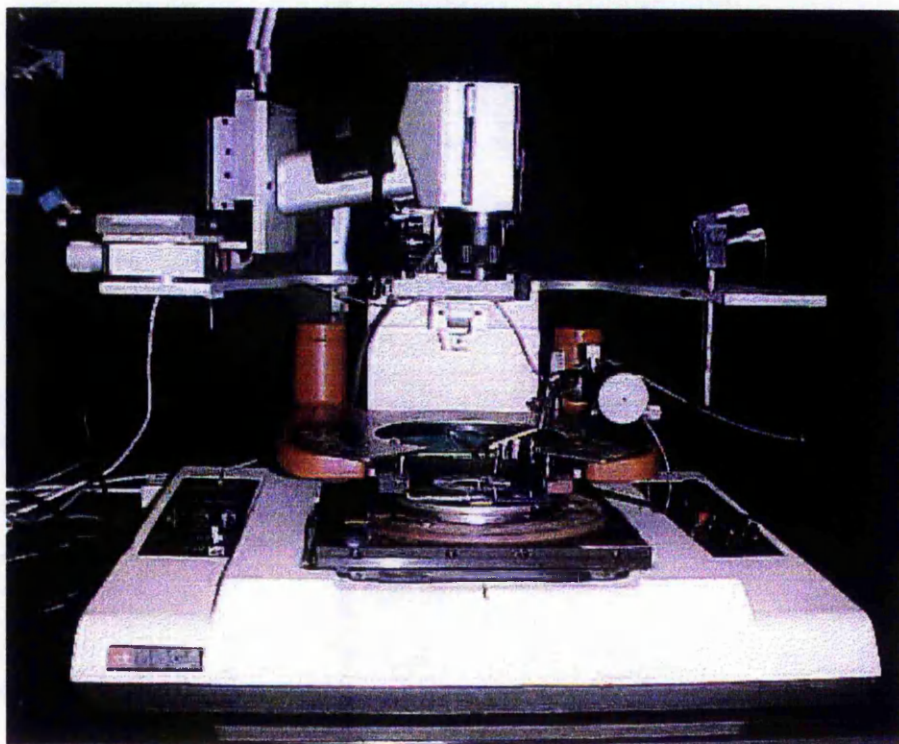


Figure 4.7 LV Measurement System

An Au probe which is connected to an AC high voltage amplifier addresses the top electrode of the device. The probe is attached to the first metallic shelf which provides movement in

the vertical direction. To align the probe with the pixel electrode, a microscope attached on hinges is focused above the wafer. This permits observation of both the wafer and the probe. The metallic plate is moved until the probe coincides onto the pixel electrode. Then the probe is moved downwards. Once the wafer is positioned and probed, the microscope is moved away and the luminance camera is rotated on the horizontal plane until it is above the testing pixel. The AC amplifier is turned on using a 5 kHz sine wave. The voltage is raised up in 8 volts steps every 10 seconds and intensity values are taken for each step. Luminance values are measured in foot Lamberts (fL) using a luminance meter Minolta LS-110 which is positioned at 20 cm away from the wafer with the internal lens system focused on the device surface. The camera provides an acceptance angle of $1/3^\circ$ so only light emitted within this solid angle around the vertical axis is detected. The voltage values are taken from a Tektronix Model TDS 210 oscilloscope. Only virgin devices were measured in a dark ambience and at room temperatures.

4.6.2.- Angular Measurement System

To determine the angular profile, a system as the illustrated in Figure 4.8 was designed and built for this research. Figure 4.9 shows a diagram of the system where the metallic plate, which is the wafer holder, can be rotated on the horizontal plane and the center of rotation has been determined and marked on the plate. Before the wafer is placed in position, the microscope is rotated over the plate and is aligned with the center of rotation. The wafer is then placed onto the plate and is moved until the device to be addressed is aligned with the microscope. This ensures the device is positioned at the center of rotation of the metallic plate. The plate is grounded and connected to a vacuum pump which ensures good contact with the Si substrate of the wafer.

The probe is held by an xyz micrometer movement so that it can be moved above the wafer. Probing of the device is accomplished by observing through the microscope while moving and lowering the probe until contact is made with the wafer at the desired point. The microscope is then moved away and the optical fiber is placed in position. The probe is connected to an AC high voltage amplifier which produces a 5 kHz sine wave signal. The voltage is turned on and progressively increased and maintained at 420 V peak to peak while the emitted intensity is read from the photomultiplier attached to the fiber.

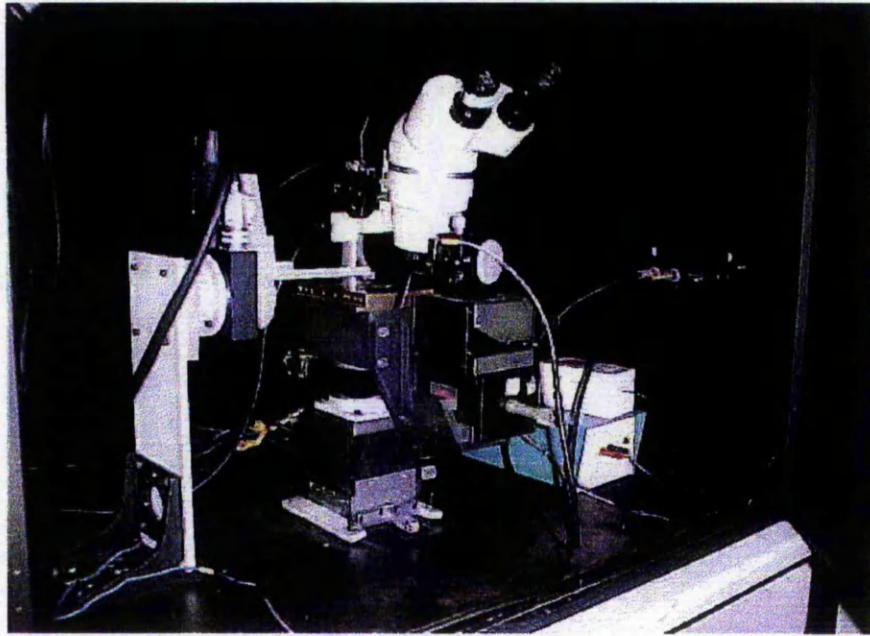


Figure 4.8 Angular Measurement System

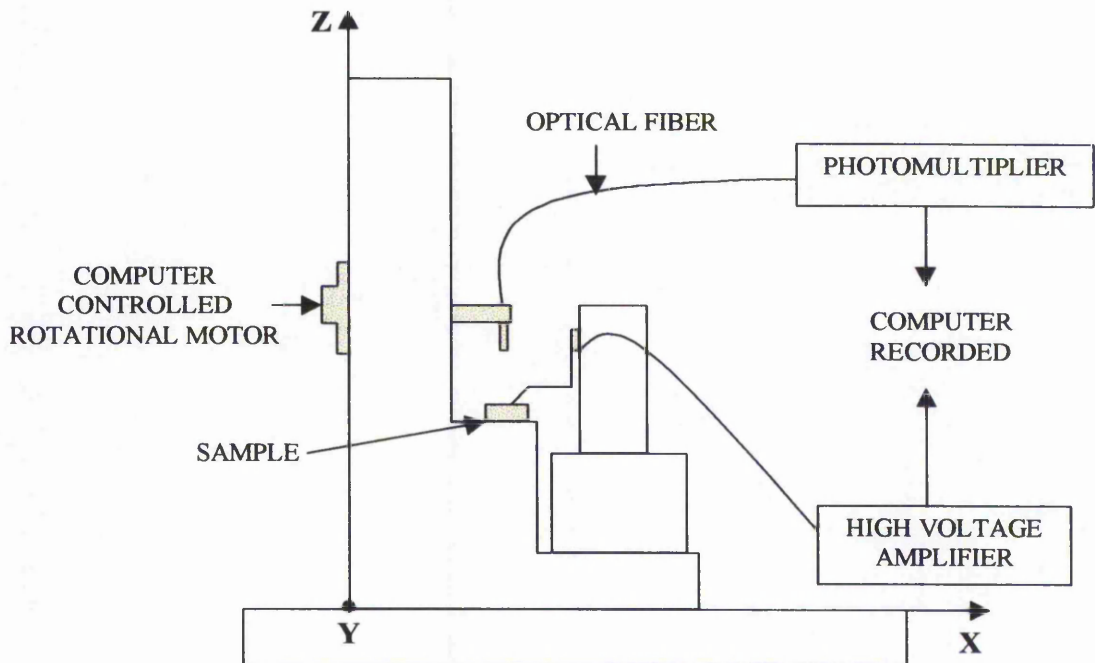


Figure 4.9 Angular measurement system built for the present research

The fiber is held by a metallic arm which can slide in the y direction to adjust the distance between the fiber and the device. Additionally, it can rotate in the xz plane. Rotation is obtained with an external motor which is automated through the use of LabVIEW in progressive 1° steps.

The LabVIEW program is started and the fiber begins rotating while the light intensity values versus the angle are automatically saved. The system was set and calibrated to 0.1 units of intensity corresponding to a brightness of 1.5 fL.

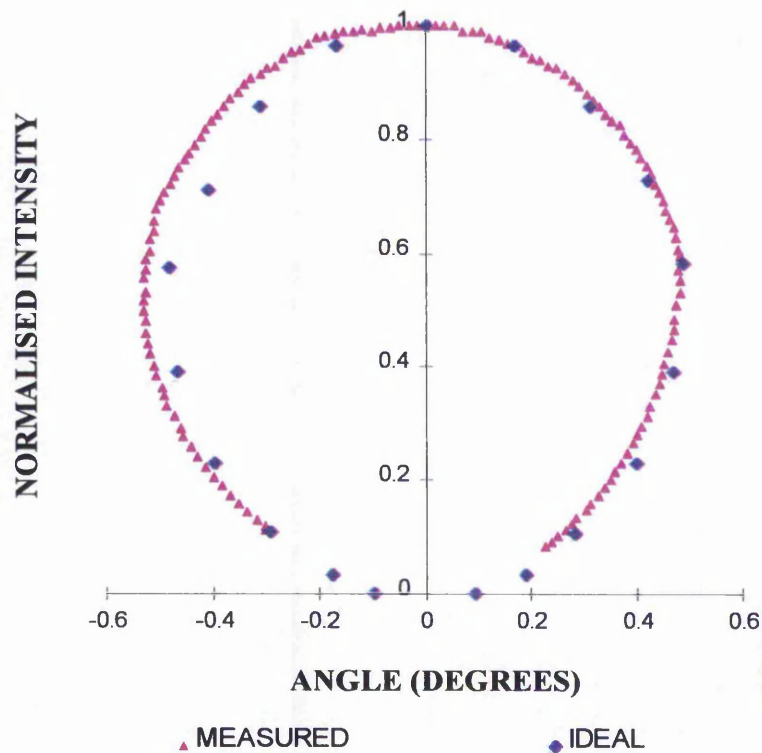


Figure 4.10 Calibration of the Angular Measurement System

To ensure reliability of the measurements, the system was calibrated using a surface mount LED HLMP-Q106 acquired from RS Components UK. The LED angular response was provided and compared to the angular response obtained using the angular measurement system herein developed. As illustrated in Figure 4.10 a maximum 10% difference between the calibration data sheet provided by the company and the measurements performed with the experimental set-up has been measured. This is due to the fact that the data sheet provided by RS Components represents an idealised response from a perfect product while the LED tested has been randomly selected and is subjected to manufacturing tolerances.

4.6.3.- Device Subjected to Test

To enable comparison of the measured properties, a pixel containing a single $3 \cdot 10^{-3} \times 1.6 \text{ mm}^2$ rectangular aperture which divides two identical $1.6 \times 0.2 \text{ mm}^2$ active areas, as the illustrated in Figure 4.10 was tested on all the samples. The pixel can be independently addressed so that either the light output from a single active layer or the combination of both active layers can be determined. Comparison of the light output properties was also facilitated by preventing variations in the device efficiency due to differences in the deposition process among the measured samples. Therefore, the LETFEL thin films were deposited onto a 100 mm Si wafer which was subsequently split into pieces; each sample was then processed at different conditions and the results were compared.

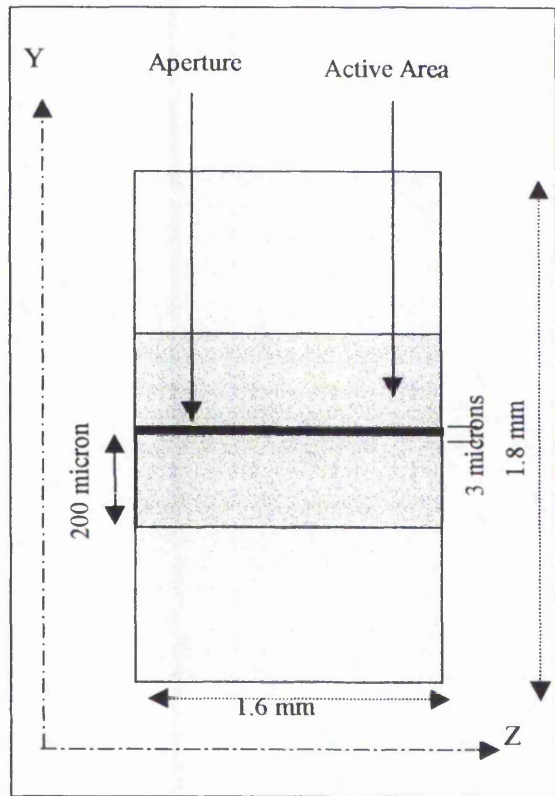


Figure 4.11 Top surface of a test sample

4.7 CONCLUSIONS

This chapter has provided a general overview of the route utilised for the fabrication of LETFEL devices and the equipment required to determine the light output properties. As previously mentioned, ion milling is the sputter etch technique applied to shape the LETFEL device apertures. As a result, a study of the ion milling properties of the EL thin film materials involved has been performed and is presented in the following chapter.

**ION MILLING CHARACTERISTICS OF LETFEL
DEVICES AND ASSOCIATED MATERIALS**

-
- 5.1 Introduction
 - 5.2 Thin Film Preparation
 - 5.3 Ion Milling Characteristics of LETFEL Materials
 - 5.4 The Ion Milled ZnS:Mn Wall Side Profile
 - 5.5 Conclusions
-

5.1 INTRODUCTION

The outcoupling mechanism of LETFEL devices is determined by the device aperture geometry, and its fabrication usually requires etching of the LETFEL thin films. For the mechanisms discussed in Chapter 4, an etch technique which permits controlled shaping of the etched profiles is required and in the present research, ion milling has been selected.

As previously discussed, ion milling is a sputter etch method which incorporates a collimated ion beam as the sputter source. This directional character is a unique property of the technique which permits control of the angle of incidence of the beam upon the substrate^{72,73}. This angle is varied by changing the tilt of the target plate. As a result, for an etched pattern, the angle of the walls with respect to the base of the etched groove can be controlled. Ion milling is also a universal etcher which constitutes an advantage for etching LETFEL devices since a reactive etch for Y_2O_3 is still elusive. The main disadvantage of the technique is that conventional resist patterns can be damaged due to heat generation for typical beam powers. Consequently, an alternative material is required as the ion-milling mask. This adds a new fabrication step and consequently slightly complicates the LETFEL device fabrication route.

Presented in this chapter is a study of the ion milling properties of LETFEL devices and associated materials. Identified are the ion milling etch rates of $ZnS:Mn$, Y_2O_3 , Si_3N_4 , SiO_2 , and SiO_xN_y thin films. The etch rate determines the rate at which thickness is removed from a given material. To define the etch rate the process conditions which are the angle of beam incidence, the ion beam current density, the acceleration voltage and the process time need to be specified.

The ion beam current density is a measure of the number of ion particles striking the substrate per unit area. This is expressed in miliamperes per square centimeters (mA/cm^2) which is the electrical current density generated by the beam of positively charged ions striking on the surface. A current density of $1 mA/cm^2$ corresponds to $6.25 \cdot 10^{15}$ single charged ions striking a square centimeter of surface per second.

The acceleration voltage determines the ion beam energy which is the energy of the ions impinging on the substrates being etched. This is expressed in terms of electron Volts (eV). For example a setting of 500 V on the accelerating voltage gives an ion beam energy of 500 eV. An Ar ion with an energy of 500 eV has a speed of $5.4 \cdot 10^6$ cm/sec.

The angle of beam incidence is defined as the angle between the normal to the substrate plate and the direction of the ion beam. As an example, a vertical angle of incidence corresponds to an angle of incidence of 0° .

The ion milling time determines the duration of the process. This depends on the thickness to be etched and the materials etch rate. Ion milling for long periods of time can introduce damage to the etched thin films due to heat generation. In the present research, ion milling was performed in a 5 minutes on 5 minutes off basis which was determined to avoid damage to the thin films.

Simulations presented in this thesis are in agreement with the experiments and explain the origin of the profile shapes. Additionally, LETFEL device aperture shapes have been obtained by varying the ion milling parameters.

5.2 THIN FILM PREPARATION

For the study of ion milling characteristics single thin films of the required materials were prepared. Preparation includes the deposition of these thin films into 100 mm diameter Si substrates and in particular cases additional photolithography.

Deposition was performed according to the process conditions detailed in Chapter 3. 8000 Å ZnS:Mn and 3000 Å Y_2O_3 thin films were rf magnetron sputtered onto Si, and SiO_2 , Si_3N_4 and SiO_xN_y were deposited by PECVD. The deposited thicknesses of SiO_2 , Si_3N_4 and SiO_xN_y were measured also by means of an interferometric technique using a Nanometrics 210 Film Thickness System.

The ZnS:Mn thin film was masked with a sacrificial layer of SiO_2 to enable definition of a step in the thin film when ion milled. In ZnS:Mn the step profile shape is important for outcoupling purposes and masking enables the effect of different ion milling conditions on the shape to be determined.

Masking of ZnS:Mn was accomplished using PECVD SiO_2 since as previously discussed, conventional photoresist is not suitable as an ion milling masking material. According to the masking route involving dielectrics detailed in Chapter 4, a 2 μm SiO_2 film was deposited onto the ZnS:Mn film and subsequently masked with conventional photoresist. The photoresist pattern was transferred to the SiO_2 layer using RIE under process conditions

previously detailed. Since the ZnS:Mn etch-rate under the selected conditions is low ($<10 \text{ \AA}/\text{min}$), RIE provides high selectivity values ($>56:1$) which permit overetching of the SiO_2 film ensuring full transfer of the photoresist pattern. As a result and although the estimated time was 36 minutes, the process time was extended to 45 minutes which corresponds to the estimated time plus its 25%. The remaining photoresist was finally stripped in an O_2 plasma.

The main aim of this study is the calibration of the ion milling characteristics of LETFEL materials in order to enable shaping of the device aperture. Therefore, all the materials were grown as single thin films following an identical deposition process to the conventionally utilised in the fabrication of LETFEL devices at the NTU as presented in Chapter 4.

5.3 ION MILLING CHARACTERISTICS OF LETFEL MATERIALS

Ion milling characteristics of LETFEL device materials have been determined for four different parameters: the etching time, the Ar^+ beam angle of incidence, the acceleration voltage and the beam current.

Single samples of each material were simultaneously loaded in the Veeco Microetch System work chamber which was closed and pumped down to a base pressure of $6 \cdot 10^{-6}$ Torr. Subsequently Ar gas was injected in the discharge chamber and the pressure was raised and maintained at $2.4 \cdot 10^{-4}$ Torr using the foreline valve. An Ar plasma was initiated via the application of an AC voltage between the heated cathode and the anode of the discharge chamber. The Ar^+ ions of the plasma were emitted as a collimated beam through the two molybdenum grids to which an accelerating DC voltage of 500 V was applied. The beam current density was set to $0.5 \text{ mA}/\text{cm}^2$. Ion milling was undertaken at a series of angles of incidence and for different lengths of time, maintaining all the other parameters constant.

5.3.1 Ion Milling versus the Time

A series of ion milling processes were performed under the conditions previously detailed, at an angle of incidence of 0° and at different etching times within the range of 5 to 28 minutes.

The maximum etching time was limited by the duration supported by each material thickness without sputtering through.

After ion milling, the ZnS:Mn thin films coated with SiO₂ were subjected to RIE to accomplish complete removal of the mask. Under the applied RIE conditions detailed in Chapter 4, the ZnS:Mn etch-rate is below 10 Å/minute which allows over-etching of the SiO₂ film to ensure complete removal of the thin film. This enables measure of the ZnS:Mn etched step height using the Tencor P-2 Long Scan Profiler.

The remaining thin film thicknesses were measured before and after ion milling using the Nanometrics 210 Film Thickness System and the etch rate was determined. Figure 5.1 illustrates the ion milling rates versus the etching time.

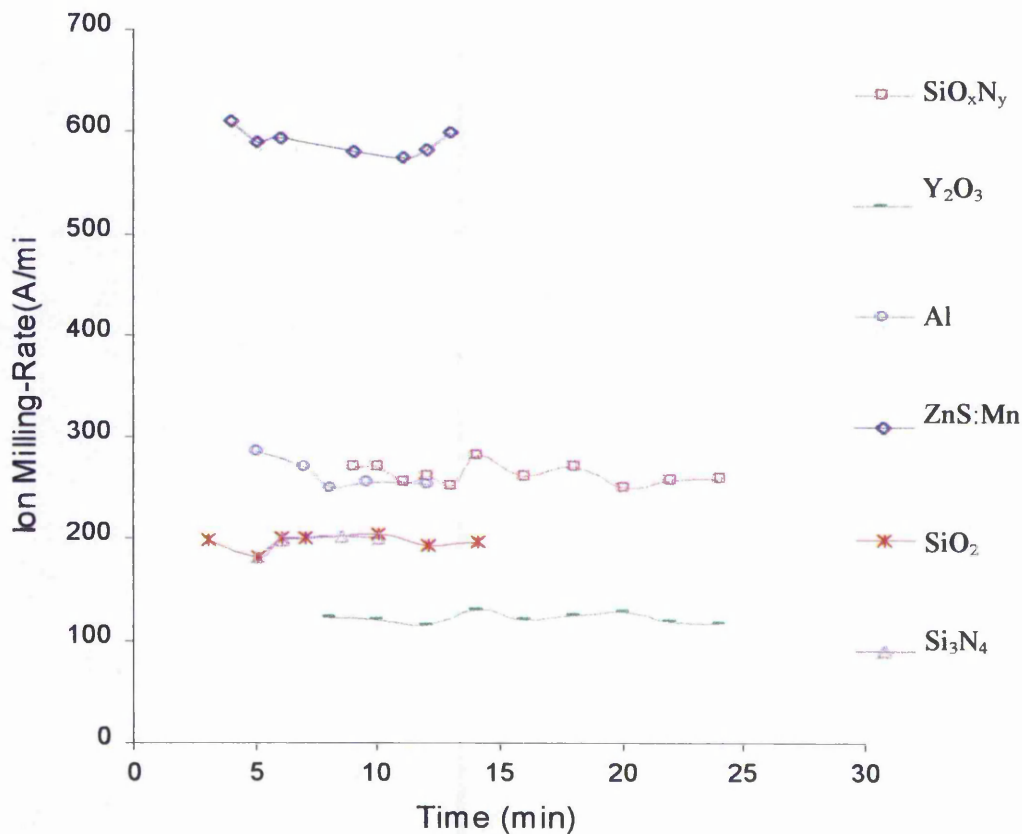


Figure 5.1 Ion milling rates versus time of the thin film materials indicated

Although no trend of etch-rate increment or decrement with time is shown, slight variations in the etch-rate values due to measurement uncertainties can be observed. As a result, averaged etch-rates have been determined for each material and these are included in Table 5.1. From all the materials studied, ZnS:Mn, the active thin film, and Y₂O₃, the insulator material, show the highest and lowest etch-rates respectively.

	ZnS:Mn	Y ₂ O ₃	SiO ₂	Si ₃ N ₄	SiO _x N _y
IM Rates (Å/min)	586	121	198	191	262

Table 5.1 Averaged ion milling rates of LETFEL materials

This, added to the observed etch-rate constancy with time, provides very high etch-rate selectivity between these two LETFEL device neighbour layers which contributes to a higher control of the aperture profile definition.

5.3.2 Ion Milling versus the Angle of Incidence

Ion milling characteristics versus the ion beam angle of incidence were determined for two different acceleration voltages: 500 V at a beam current of 0.5 mA/cm² and 400 V at a beam current of 0.450 mA/cm². A series of processes were carried out for 10 min and the angle of incidence of the Ar beam was varied from 0° to 90° while all the other parameters were maintained invariant and set as above. The thin film thicknesses were measured both before and after ion milling. The etch rates of all the materials versus the ion beam angle of incidence were calculated at the two stated voltages and are illustrated in Figures 5.2 a and 5.3. Notice that the angle has been measured with respect to the normal to the film surface. It can be observed that the etch-rate values vary in a similar manner with the angle of incidence for all the studied materials: an etch-rate maximum is always observed at intermediate angles. This behaviour is mainly related to two different factors: the dependence of the Ar⁺ beam density with the angle of incidence and the direction of the momentum of the incoming Ar⁺ particle. As a result, the total etch-rate, E_T(φ), can be expressed as:

$$E_T(\phi) = E_1(\phi) * E_2(\phi) \quad 5.1$$

where $E_1(\phi)$ represents the effect of the variation of the Ar^+ density with the angle and $E_2(\phi)$ the effect of the direction of the momentum of the Ar^+ beam on the etch-rate.

The Ar density bombarding a flat surface varies with the angle of incidence as:

$$A(\phi) = A_0 \cos(\phi) \quad 5.2$$

where ϕ is the angle of incidence measured respect to the normal to the surface, $A(\phi)$ represents the Ar density for an angle of incidence and A_0 is the Ar density at normal incidence. Assuming that the etch-rate is directly dependent on the Ar density we can state:

$$E_1(\phi) \approx E_0 \cos(\phi) \quad 5.3$$

where ϕ is the angle of incidence and E_0 the etch-rate at normal incidence. $E_2(\phi)$ can be calculated if $E_T(\phi)$ is divided by $E_1(\phi)$ and it represents the dependence of the etch-rate with the angle of incidence, independently of the beam density variation with the angle. This relation is illustrated in Figure 5.2 b.

The Ar^+ beam momentum can be generally split into two components: the tangential component, parallel to the surface being etched, and the perpendicular component. Assume for low incident angles, there is a small contribution of the tangential component. As a result, most of the impact energy is directed perpendicular to the surface and a smaller amount provides an initial momentum towards the outside of the surface. For higher incident angles, the tangential component of the momentum increases. As a result, the probability of a particle escaping from the surface becomes larger and consequently the etch-rate is strongly enhanced. Notice that this dependence with the angle varies slightly with the material. This behaviour is presumably due to inherent properties of the etched materials since the sputter yield depends on the crystallographic orientation⁷⁴.

As illustrated in Figure 5.3, a similar behaviour has been demonstrated when the ion milling acceleration voltage is reduced to 400 V and the beam current is set to 0.450 mA/cm². As expected, the etch-rate values are lower than those obtained at 500 V and 0.5 mA/cm² since the impact energy and the Ar^+ flow have been reduced. Nevertheless, the etch-rate maxima correspond to the same angles of incidence when compared with the values shown in Figure 5.2 a. Consequently, it can be stated that a change in the acceleration voltage and beam current modify the material etch-rates but does not change the angle for maximum etch-rate

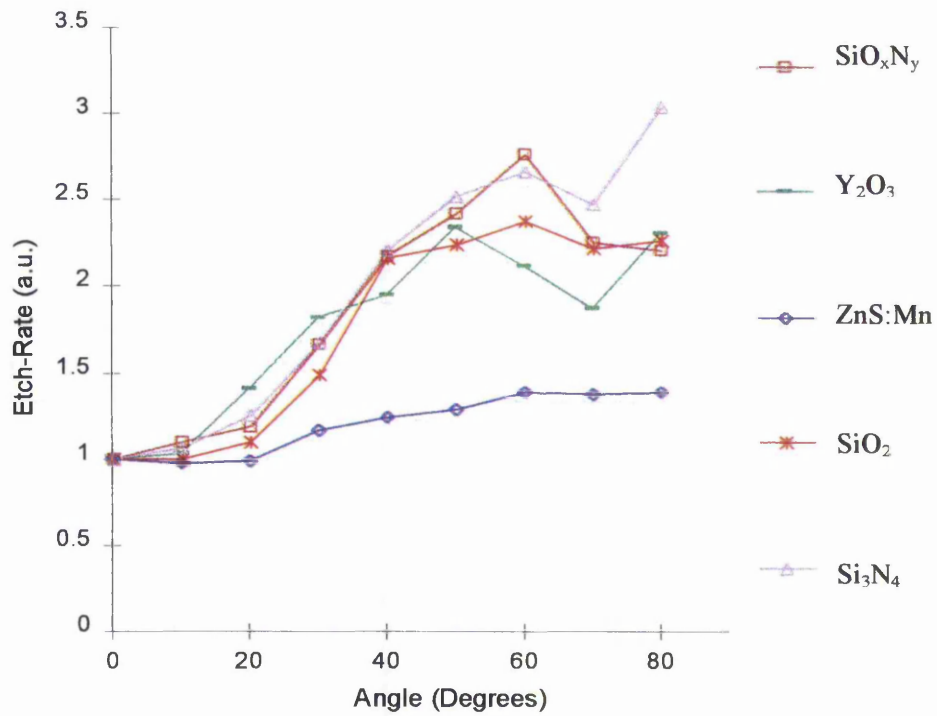
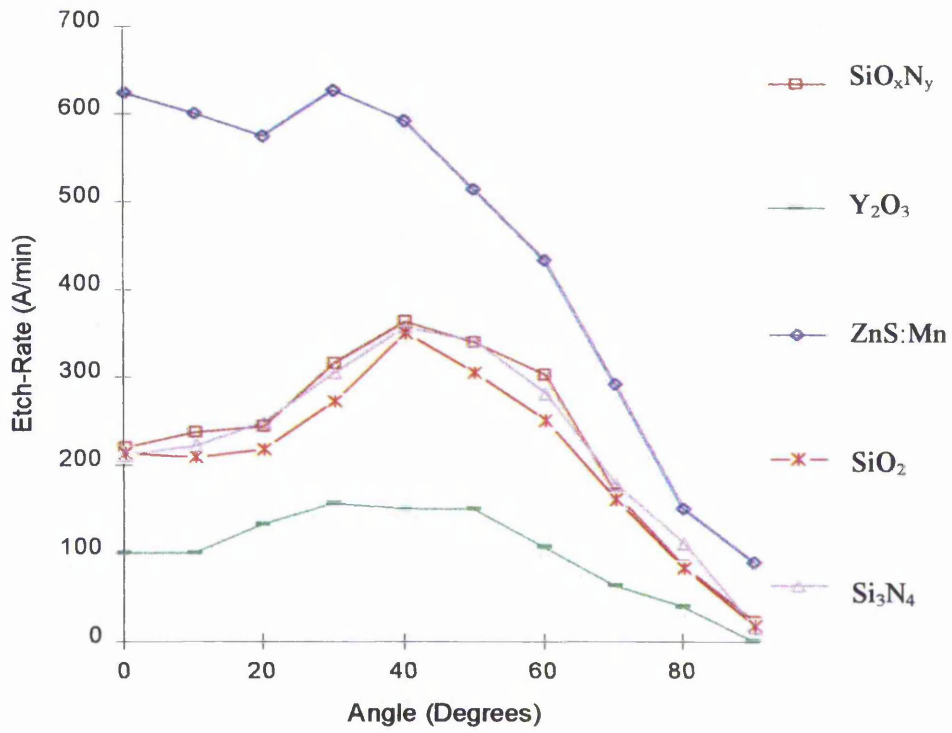


Figure 5.2 a) Ion milling rate versus the angle of incidence for an acceleration voltage of 500 Volts and a beam current of 0.500 mA/cm² **b)** Dependence of the ion milling-rate with the angle of incidence, independently of the beam density variation with the angle

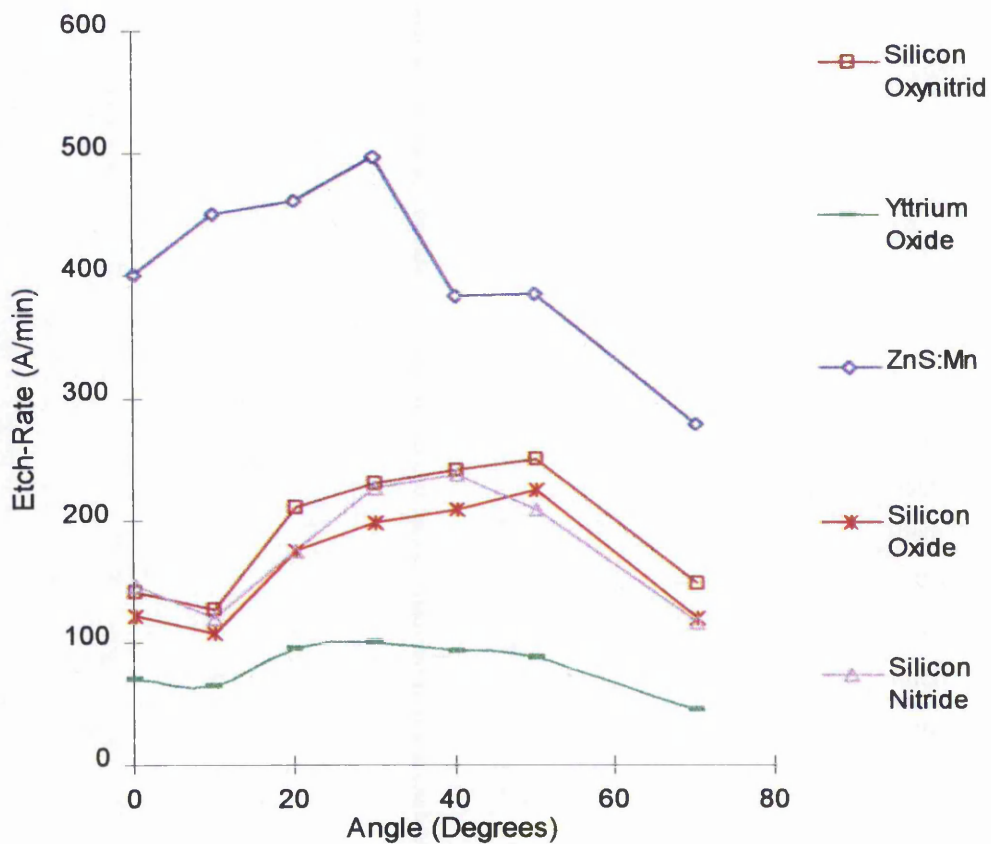


Figure 5.3 Ion milling-rate versus the angle of incidence at an acceleration voltage of 400 Volts and a beam current of 0.450mA/c²

5.4 THE ION MILLED ZNS:MN WALL SIDE PROFILE

The ZnS:Mn wall angle at the aperture regions has a remarkable importance in the outcoupling mechanism of LETFEL devices when light, which is mainly propagated within the phosphor, is outcoupled through an abrupt end. For an ion milled pattern, the angle of the abrupt end with respect to the base of the etched groove can be controlled by choice of the angle of beam incidence and rotation of the substrate. In this work, this unique feature of ion milling has been utilised. Both experimental observation and theoretical modelling of the effect of the angle of incidence onto the ZnS:Mn etched profile have been performed.

5.4.1 Experimental Ion Milled Profiles

Figure 5.4 shows an 8000 Å rf magnetron sputtered ZnS:Mn thin film coated with 2 μm of SiO₂ deposited by PECVD. The SiO₂ film was masked with conventional photoresist and patterned by RIE.

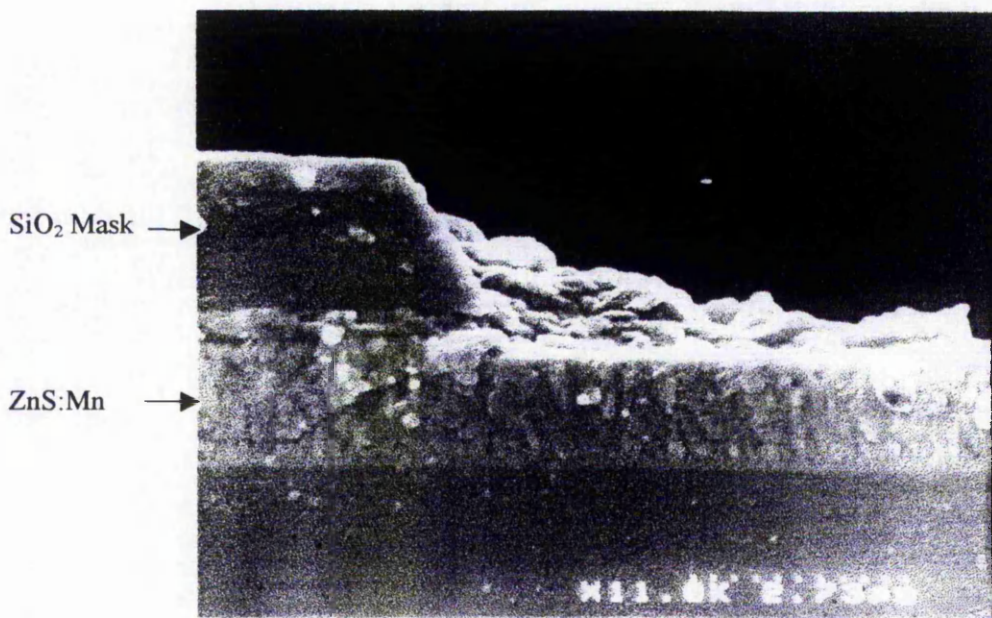


Figure 5.4 SiO₂ mask on ZnS:Mn thin film before ion milling

A 60° wall angle can be observed on the SiO₂ film as a result of the RIE process and this is considered the initial geometry for all the processed samples before ion milling.

SEM pictures of ion milled ZnS:Mn cross sections were taken for angles of incidence of 0°, 10°, 30° and 50° as shown in Figure 5.5. Figures 5.5 a and b show a straight profile at an angle of 70° and 89° with the device surface. However, Figures 5.5 c and d, show curved profiles whose curvature radius increases with the beam angle of incidence. To understand the effect of the beam angle of the wall profile, modelling of the milling process was performed and is detailed in the following section.

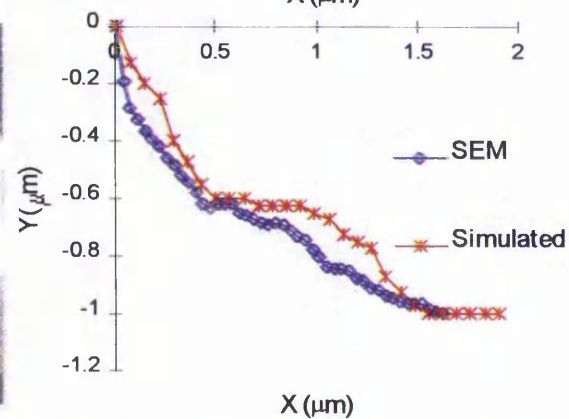
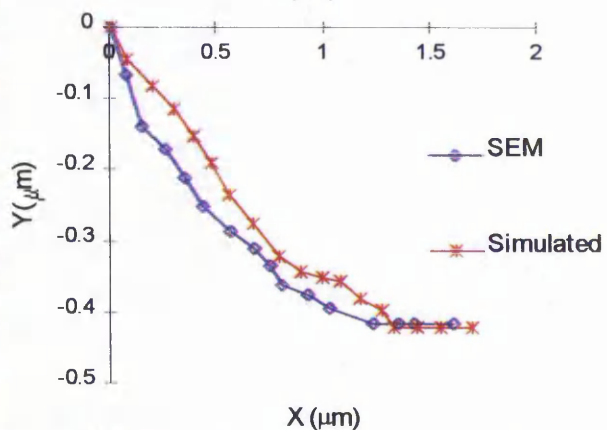
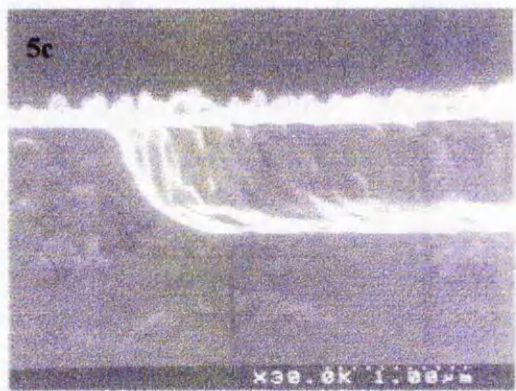
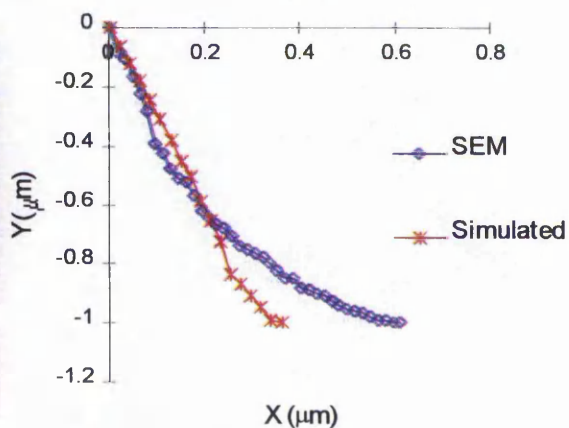
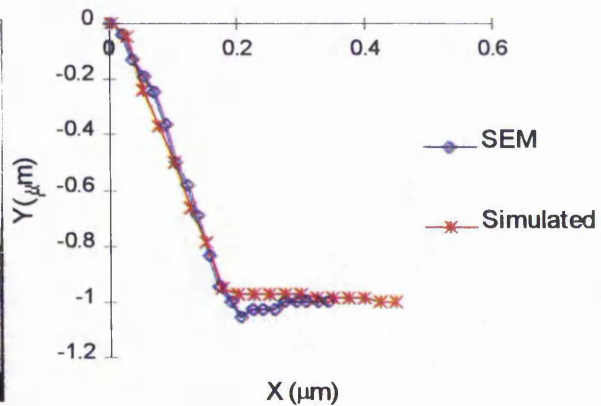
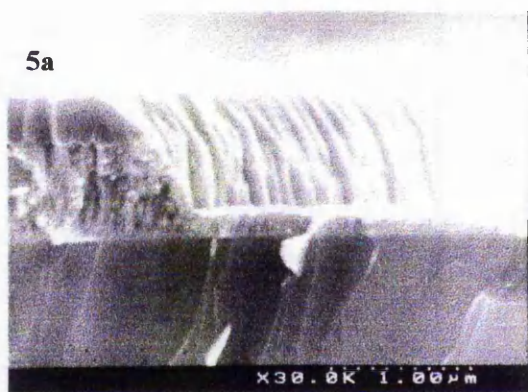


Figure 5.5 Comparison among fabricated and simulated ZnS:Mn profiles ion milled at the following angles of incidence: a) 0° b) 10° c) 30° d) 50°

5.4.2 Modelling of the Ion Milled Profiles

The ZnS:Mn wall profile versus the ion beam angle of incidence was modelled using the Silvaco's Virtual Wafer Fab (VWF) Framework Athena Elite Software. The main aim of the simulation was to obtain some understanding in the effect on the wall profile of varying the beam angle of incidence. To perform the calculations, the etch rate values of the involved materials were required and these were extracted from the experimental data contained in Figure 5.5. The SiO₂ mask profile from Figure 5.4 was assumed to be the starting point for all the simulations performed.

5.4.3 Comparison between the Experimental and the Modelled Profiles

Modelling has been accomplished according to two different orders of approximation. The first order took into account the difference in etch rate between the ZnS:Mn thin film and the SiO₂ mask. This provided simulated profiles in good approximation with the experimental results for beam angles of incidence lower than 30° as illustrated in Figure 5.5 a. This shows the comparison between first order modelling and experiments for a ZnS:Mn thin film ion milled at an angle of incidence of 10°.

The first order approximation is no longer valid to predict the profiles generated from angles of incidence higher than 30°. The simulation needs to incorporate the blocking effect introduced by the ion milling mask to ions reaching the ZnS:Mn thin film at high angles of incidence. Since the target plate is rotating, this effect generates a shadow on the ZnS:Mn film when the mask pattern is on the side of the incoming beam while the ions follow a free path when the mask pattern is opposite to the beam. In the present simulations however, a fixed target plate has been assumed where the mask pattern is opposite to the incoming beam. As a result, the shadow is permanently generated on the ZnS:Mn thin films which leads to lower effective etch-rates on the etched walls.

The shadow is strongly dependent on the mask geometry. The mask wall angle determines the minimum incidence angle required for shadow generation while the mask height determines the dimensions of the shadow. The higher the provided mask the wider the etched profile. In the present research, the SiO₂ mask is 2 µm high and forms a 60° angle with the surface. This mask partially stops the ion beam incoming at higher angles of incidence than 30° from reaching the ZnS:Mn thin film.

During ion milling the mask is constantly removed from the sample which leaves free access to more incoming ions to reach ZnS:Mn areas which were initially blocked. As a result, different sections of the ZnS:Mn wall undertake etching for different lengths of time which leads to a curved profile. Figures 5.5 c-d illustrates agreement among experimental profiles and second approximation modelling of ZnS:Mn samples which undertook ion milling at 30°, 50° and 60°.

Higher orders of approximation could be introduced in the modelling such as the rotation of the target plate or the difference in etch-rate for different sections of the same thin film depending on the profile angle. These are expected to provide simulated profiles closer to the experimental results. However, according to the performed simulations we can state that the two main effects which contribute to the formation of the observed ZnS:Mn profiles are:

- the difference between the ZnS:Mn and the SiO₂ etch-rates, which explains the straight profile obtained for incident angles lower than 30 °.
- the mask shadow generated on the ZnS:Mn film which accounts for the curved profile obtained for greater angles.

5.5 CONCLUSIONS

In this chapter ion milling has been experimentally demonstrated to be a successful technique to etch the LETFEL thin films. The ion milling rates have been found to be constant with respect to the etching time however, these have been observed to vary with the ion beam angle of incidence for all the studied materials. Particularly, a maximum rate is observed for intermediate angles. Etch-rates have been calculated for two different beam acceleration voltages; a drop in the etch-rate occurs for the lowest and the etch-rate maximum remains constant for all the materials. It has also been observed that different ion beam angles generate different ZnS:Mn profiles. Simulations support that these profiles depend on the masking material versus the ion milling-rate as well as on the masking shadow effect. The etch-rates determined from these experiments have been utilised to etch and shape the device aperture. The applied conditions are specified in the following chapter.

**EXPERIMENTAL DETERMINATION OF THE
LIGHT OUTPUT PROPERTIES OF LETFEL
DEVICES**

-
- 6.1 Introduction
 - 6.2 Experimental Determination of the light output properties of the conventional non-etched LETFEL device
 - 6.3 Fabrication parametres and experimental determination of the light output properties of etched LETFEL devices
 - 6.4 Fabrication parameters and experimental determination of the light output properties of etched LETFEL devices
 - 6.5 Conclusions: Comaprison of the light output properties of the fabricated devices
-

6.1 INTRODUCTION

In Chapter 3, a theoretical study of conventional non-etched LETFEL devices predicted poor outcoupling efficiency resulting in values lower than 4 % of the generated light. In this chapter, experimental data is presented which additionally demonstrates inadequate angular emission profiles. These experimental results in addition to the theoretical study of Chapter 3 reveal the need for a more efficient outcoupling mechanism to be incorporated in LETFEL devices.

Also included in Chapter 3 was a theoretical study of two novel mechanisms, the etched aperture and the surface emitting edge emitter, which demonstrate the ability to produce more advantageous light output properties. Fabrication of these structures is required to demonstrate feasibility of the fabrication process and veracity of the theoretical results.

In the present chapter, the particular fabrication parameters required to generate etched and surface emitting edge emitter LETFEL devices are investigated. Fabrication of the novel devices was accomplished following the fabrication route established in Chapter 4. The process parameters were determined according to the following criteria:

1. Device fabrication for various ion milling times and the ion milling angles of incidence.
2. Inspection of the resultant aperture geometries through Scanning Electromicroscope (SEM) observations.

The resultant light output characteristics were assessed according to the following criteria:

3. Measurement of the light intensity versus voltage characteristic (LV): The light emitted perpendicular to the surface versus the applied voltage was measured for various processed samples. Note that only relative light intensity values are presented given in arbitrary units which can be related to the brightness value in fL by multiplying it by a factor of $\times 10$. Absolute measurements have not been illustrated since the latter depend on multiple phenomena within the device which are out of control in the current work. Relative values are suitable for the present research since the major intention is to establish comparison among the fabricated apertures. Identical samples were utilised for the fabrication of the aperture geometries which allows comparison among the output properties.

4. Measurement of the angular distribution: This measurement establishes the divergence behaviour of light outside the device which has a significant importance in the coupling power into HMD and EP applications. It also allows comparison among outcoupling efficiency values of different devices. This is accomplished by integration and normalisation of the angular distribution, and further multiplication by the relative intensity determined from the LV characteristic.

6.2 EXPERIMENTAL DETERMINATION OF THE LIGHT OUTPUT PROPERTIES OF THE CONVENTIONAL NON-ETCHED LETFEL DEVICE

Figure 6.1 presents a typical cross section of a conventional non-etched LETFEL device aperture, which illustrates the bending effect of the underlying microstructures on the thin film layers. $3\ \mu\text{m}$ wide and $1.5\ \mu\text{m}$ high microstructures are utilised. The electrode is removed at the aperture region using a $3\ \mu\text{m}$ aperture opening on the SiO_2 mask. As illustrated in the figure, this results in partial overlapping of the electrode layers onto the sides of the micromirrored aperture producing blocking of any light emission along these regions.

The associated LV characteristic was experimentally determined, as illustrated in Figure 6.2 a, using the measurement system detailed in Chapter 4. As previously mentioned, this measurement provides exclusive information of the light emerging perpendicular to the device surface. Thus, to determine the intensity outcoupled in a wider emission angle, the angular profile was examined from -60° to $+60^\circ$ as illustrated in Figure 6.2 b. The angular profile corresponds to a symmetrical distribution where the light intensity reaches a minimum in the direction perpendicular to the device surface and increases monotonically up to $\pm 50^\circ$. The obtained high emission angles are inefficient for HMD and EP purposes since these require narrow acceptance angles, beyond which emission can be considered to be lost.

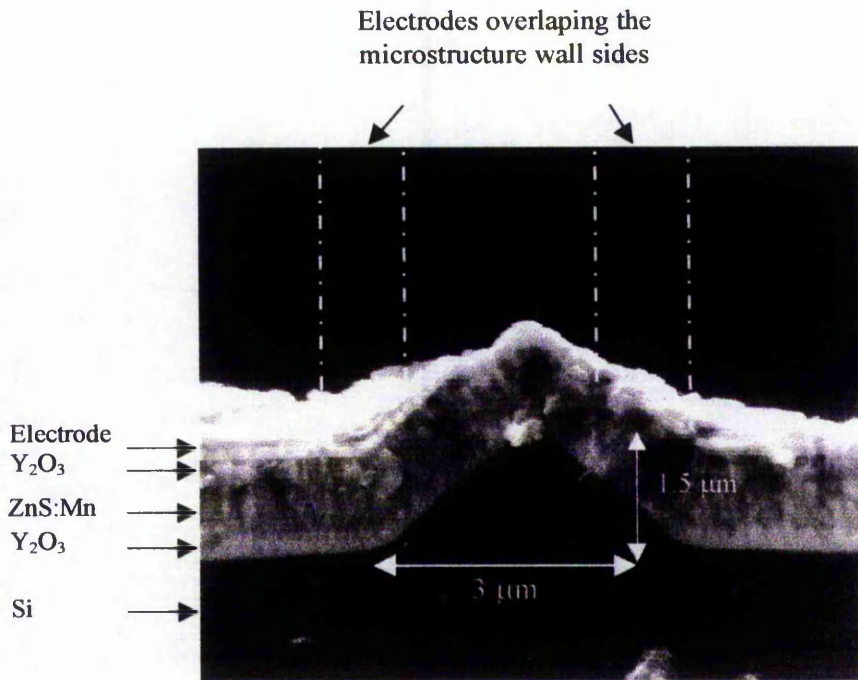


Figure 6.1 SEM illustration of a conventional non-etched LETFEL device aperture cross-section

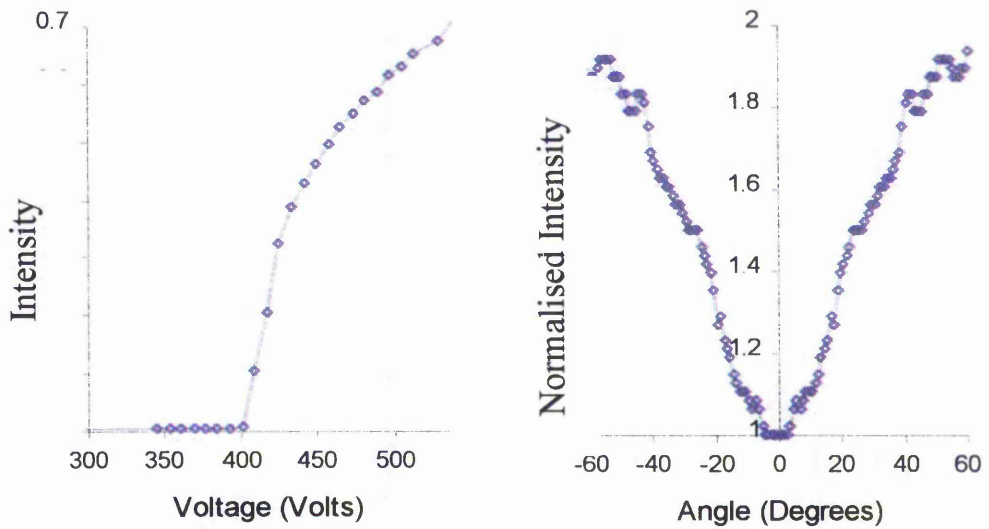


Figure 6.2
 a) LV Ch: Voltage (Volts) conventional not
 experimentally determined b) An Angle (Degree)

The coupling efficiency, τ_α , within an acceptance angle, α can be defined as the percentage of light outcoupled within a particular angle α , versus the total outcoupled light. It can be represented as $\tau_\alpha = \sigma_\alpha / \sigma_T$, where σ_α and σ_T are the intensity outcoupled within an angle α , and the total outcoupled intensity respectively. τ_α can be determined from numerical integration of the angular distribution within the acceptance angle limits.

For the particular case of HMD and EP applications which require acceptance angles within the range of $\alpha \sim 30^\circ$ and $\alpha \sim 6^\circ$ respectively, the coupling ratios have been determined from the angular profile illustrated in Figure 6.2 b to be $\tau_{\text{HMD}} = 40\%$ and $\tau_{\text{EP}} = 7\%$. This demonstrates a high percentage of losses beyond the acceptance angle, $>50\%$ and $>90\%$, respectively. As a result, improvements of the light output properties of conventional non-etched LETFEL devices are essential for coupling enhancement. Thus, according to the presented experimental results, fabrication of an outcoupling mechanism which reduces the angular profile width and attains maximum intensity values at perpendicular angles to the device surface is the main goal of the present chapter.

The process parameters leading to the fabrication of the two novel outcoupling mechanisms previously proposed are detailed in sections 6.3 & 6.4.

6.3 FABRICATION PARAMETERS AND EXPERIMENTAL DETERMINATION OF THE LIGHT OUTPUT PROPERTIES OF ETCHED LETFEL DEVICES

Etched LETFEL devices were introduced in Chapter 3 as an alternative outcoupling mechanism to conventional non-etched LETFEL devices. Although simple in concept, the fabrication process involved is complicated and has inherent limitations as will be discussed further on in this section.

6.3.1 Fabrication Route

To determine the process parameters required for fabrication of etched LETFEL devices, multiple fabrication attempts were performed which included different ion milling times and angles of incidence.

The ion milling time required to etch the LETFEL outcoupling aperture was initially estimated to be 36 minutes from the LETFEL thin film ion milling-rates presented in Chapter 5. The data included in that chapter was calibrated versus the angle of incidence. Since etched-LETFEL apertures incorporate microstructures which curve the thin films, different areas of the aperture undergo ion milling at different angles of incidence. As a result, the estimated time had to be altered. As a result, various processes were performed from 36 minutes up to 70 minutes. The effect of the angle of incidence was also studied using ion milling angles from 0° to 40° for a temporal length of 36 minutes.

The width of the apertures in the SiO_2 mask was observed to play an important role in the definition of the aperture geometry. Small widths impede total removal of materials overlying the aperture walls and the micromirror sides. Thus, the wider the aperture width the better the aperture geometry definition.

From the preliminary experiments, the following conditions were selected to fabricate the etched LETFEL aperture: ion milling time of 60 minutes, angle of incidence of 20° and a $7\ \mu\text{m}$ aperture width. The geometry obtained is illustrated in Figure 6.3. A safe horizontal distance of $2\ \mu\text{m}$ between the SiO_2 mask and the nearest micromirror bottom corner is provided which permits removal of materials through the entire aperture region. Although almost complete removal of the thin films has been achieved, nonuniformity of the etched thin films along the aperture due to the curved profile is still apparent. A small thickness of Y_2O_3 is remaining on the micromirror bottom corners which can affect the angular profile of the light emitted from the edge. Increase of the milling time is not an adequate solution since deformation of the microstructure shape on the top uncoated regions will occur. This would again produce undesired effects on the angular distribution of the reflected light. The use of wider aperture widths would provide better aperture definitions however, it would also lead to significant loss of display resolution.

As a result of these experiments it may be concluded that the process herein proposed for fabrication of etched LETFEL devices provides adequate aperture geometries for light outcoupling, but lacks of an optimised outcome. Hence, a proposal for future work is the establishment of a chemical etching recipe for Y_2O_3 and its incorporation in the fabrication route or use of an alternative dielectric such as SiO_xN_y which can be chemically etched. Furthermore, high selectivities between the LETFEL thin film etch-rates and SiO_2 are desired to avoid damage of the SiO_2 microstructure as a result of potential overetch.

6.3.2 Study of the Light Output Properties

The LV characteristic resultant from the etched LETFEL device is illustrated in Figure 6.4 a. An enhancement by a factor of 2.1 is obtained at a driving voltage of 500 V when compared with the conventional non-etched LETFEL intensity.

In order to verify that this enhancement corresponds to an increase in the outcoupling efficiency and not to a variation of the device performance due to thermal side effects induced by ion milling, an additional experiment was undertaken. Figure 6.5 illustrates the LV characteristics for an annealed device which has been ion milled at the standard conditions but which has been prevented from etching via the deposition of an un-patterned SiO₂ layer overlying the whole structure. The similarity between the conventional and annealed LV characteristics demonstrates that thermal side effects are not responsible for outcoupling enhancement.

The angular profile is illustrated in Figure 6.4 b. This shows redistribution of the outcoupled light towards narrower angles of view when compared with the conventional non-etched angular profile previously illustrated in Figure 6.2 b. A maximum in the intensity values is obtained at 0°, which is the direction perpendicular to the device surface. Decay in the intensity values occurs for higher angles.

A gaussian distribution with a characteristic width of 80° is illustrated in Figure 6.6 which fits the experimental angular divergence. Comparison of this profile with the theoretical angular profile presented in Chapter 3 is also illustrated. The latter provides a 24° characteristic width and was theoretically determined to be emitted from a LETFEL edge emitter. From the disparity of these results, it may be concluded that although leading to enhancement of the angular distribution, irregularities in the etched LETFEL aperture still introduce perturbations of the angular divergence of the light emitted through the LETFEL edge.

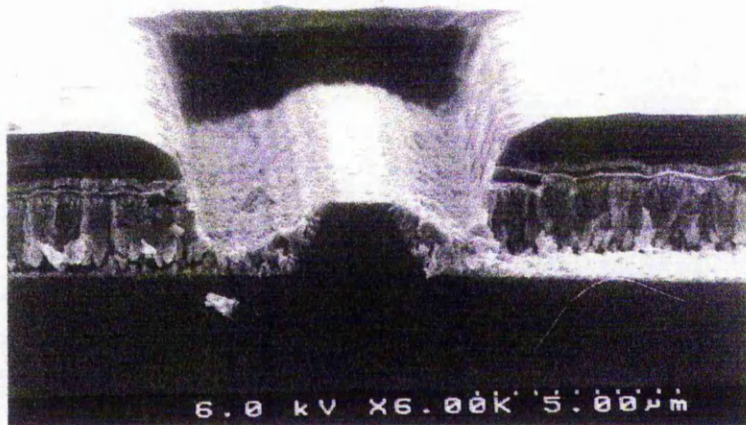


Figure 6.3 SEM illustration of an etched LETFEL device aperture cross section. A thin layer of Y_2O_3 overlies the bottom corners of the micromirror structure which may alter the expected angular profile.

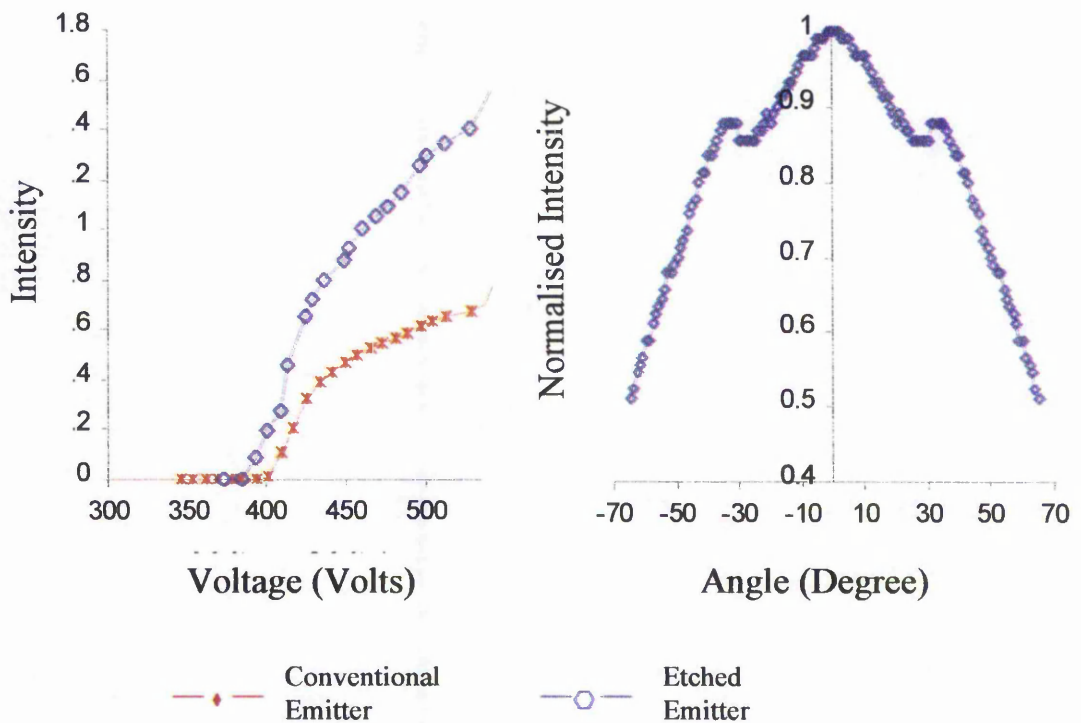


Figure 6.4 Light output characteristics of etched LETFEL devices a) Experimental LV Characteristic b) Experimental angular distribution

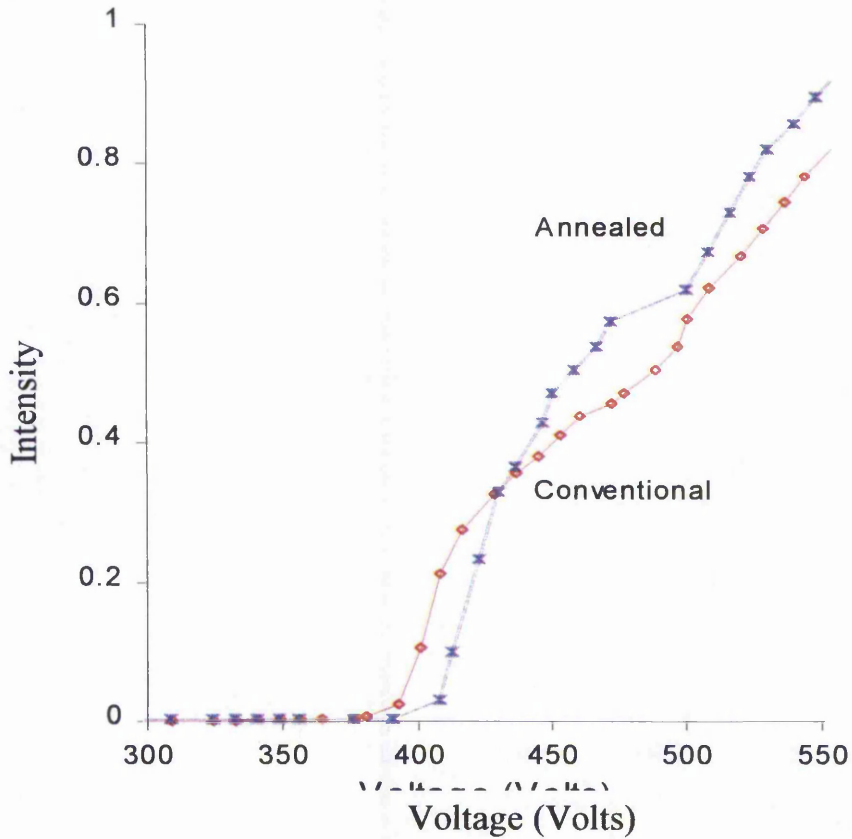


Figure 6.5 Comparison of the LV Characteristic of a conventional device and a device which was ion milled at the standard conditions but which was prevented from etching via the deposition of an un-patterned SiO₂ layer.

As before, numerical integration of the experimental angular profile provides the ratio, τ_{α} , within a particular angle, α , so that $\tau_{\text{HMD}} = 52\%$ and $\tau_{\text{EP}} = 12\%$. The amount of light redistributed within the acceptance angle of HMD and EP applications has been enhanced by 12 % and 5 % respectively.

Comparison of both, etched and conventional non-etched LETFEL angular profiles demonstrates the former to be a better optical source for HMD and EP applications. Further enhancement of the outcoupling efficiency is proposed with the incorporation of high reflective micromirrors. The current structures are made of SiO₂, with a refractive index of 1.45. As a result the reflectivity is low (<20% of the incident light) and a high percentage of the light is coupled within the micromirror.

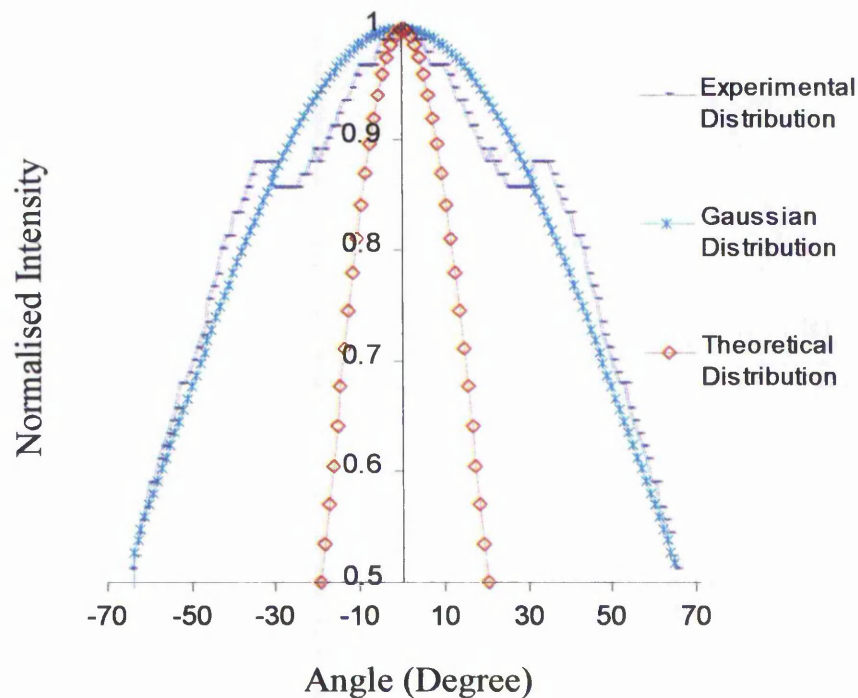


Figure 6.6 Comparison among the angular profile experimentally determined from an etched LETFEL device and the theoretical profile calculated from an abrupt open end

6.4 FABRICATION PARAMETERS AND EXPERIMENTAL DETERMINATION OF THE LIGHT OUTPUT PROPERTIES OF SURFACE EMITTING EDGE EMITTER LETFEL DEVICES

Surface emitting edge emitters constitute the second alternative outcoupling mechanism proposed in this research. As discussed in Chapter 3, these incorporate SiO₂ microstructures at the aperture regions which curve the LETFEL waveguide transforming the laterally waveguided light into surface emission. From the theoretical modelling presented in Chapter 3, these devices are expected to produce light outputs with a divergence behaviour following a gaussian distribution with a characteristic width of 24°, centered at the same angle as the microstructure wall side angle.

6.4.1 Fabrication Route

The ideal surface emitting edge emitter requires vertical wall sided microstructures which introduce a 90° tilt on the thin films. However, this research exclusively presents 45° wall sided microstructures which allow comparison of the light output properties with etched and conventional non-etched LETFEL device outputs.

As a result of multiple process attempts, fabrication of a surface emitting edge emitter was demonstrated to require small aperture widths. Successful aperture geometries were obtained when 2 μm apertures were etched in the SiO₂ mask and aligned with the 3 μm underlying microstructures.

Ion milling was performed on identical samples. This allowed comparison of the effect of the etching parameters on the aperture shape. The milling time was varied from 36 minutes to 70 minutes, and the angles of incidence from 0° to 40°.

SEM observations of the fabricated samples permitted assessment of the optimum process conditions. Figure 6.7 illustrates SEM pictures of aperture cross sections associated with samples ion milled for 38 minutes at the following angles of incidence: 0°, 20° and 40°. Comparison of these pictures demonstrates the effect of the angle of incidence on the aperture shape. Notice that both the top Y₂O₃ and the ZnS:Mn films have been removed from the aperture regions in all the processed samples. However, while ion milling at 0° and 40° generate a rough tapered edge, ion milling at 20° provides a well defined straight edge, tilted at 45° due to the micromirror wall side angle. Ion milling at broader angles of incidence results in less efficient processes which require longer fabrication times, due to the dependance of the ion milling rate on the angle of incidence. As a result, fabrication of surface emitting edge emitters will benefit from the ion milling capability of selecting the beam angle of incidence, and 20° appears to be the optimum angle.

Figure 6.8 illustrates a SEM image of an aperture cross section incorporating an edge emitter tilted at 45° along the microstructure wall side. This sample was ion milled for 60 minutes, at an angle of incidence of 20°, an acceleration voltage of 500 V, and a beam current of 0.5 mA/cm². Notice that the initial shape of the microstructure has been deformed as a result of the etching process however, this does not interfere with the light output properties.

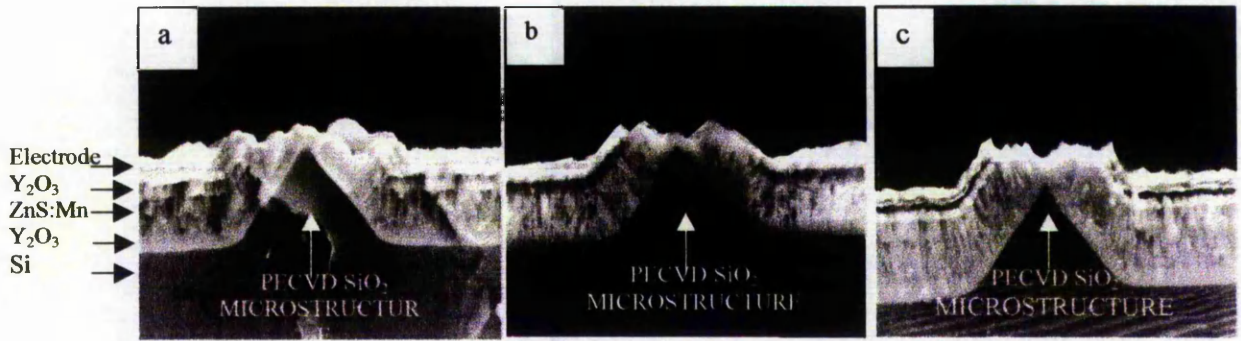


Figure 6.7 SEM illustrations of LETFEL aperture cross-sections ion milled for 36 minutes at different angles of incidence a) 0°, b) 20°, c) 40°

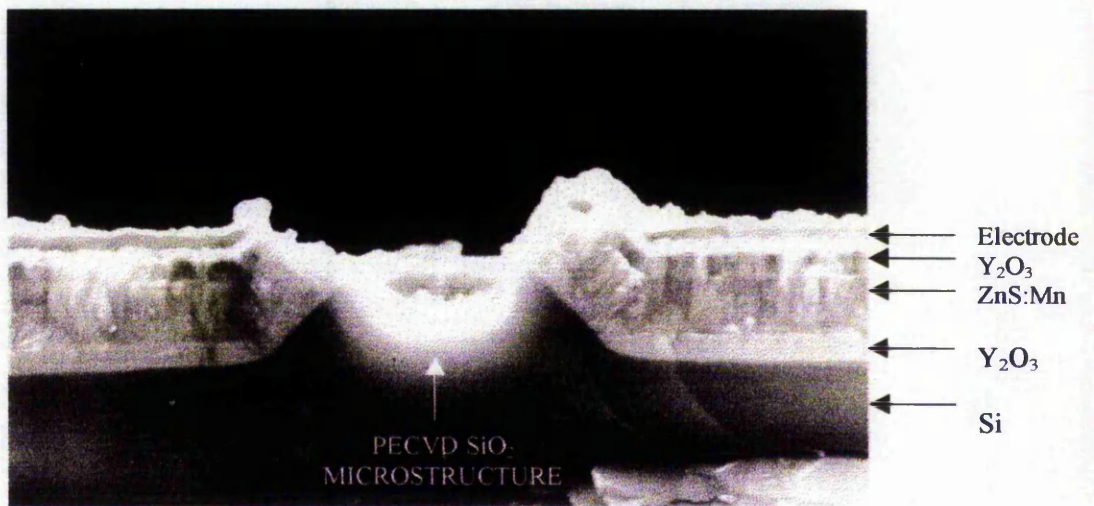


Figure 6.8 SEM illustration of a surface emitting edge emitter LETFEL aperture ion milled for 60 minutes and at 20°

6.4.2 Study of the Light Output Properties

Fig 6.9 a illustrates the LV characteristics corresponding to the surface emitting edge emitter LETFEL device. Comparison of this result with the conventional non-etched LV demonstrates a $\times 4.16$ enhancement of the top surface emission at an applied voltage of 500 Volts.

The angular distribution of the light output has also been determined and is illustrated in Figure 6.9 b which shows a minimum at 0° and two maxima at $\pm 40^\circ$. In Figure 6.10, this profile has been compared to the superimposition of two Gaussian profiles as the

theoretically determined in Chapter 3, centred at $\pm 40^\circ$. A good fit is observed. The deviation from the theoretical results observed for angles lower than 20° is assumed to be due to reflections of the light profile emitted from one side of the aperture onto the opposite side. The agreement between experimental and theoretical data demonstrate the veracity of the theoretical results presented in Chapter 3.

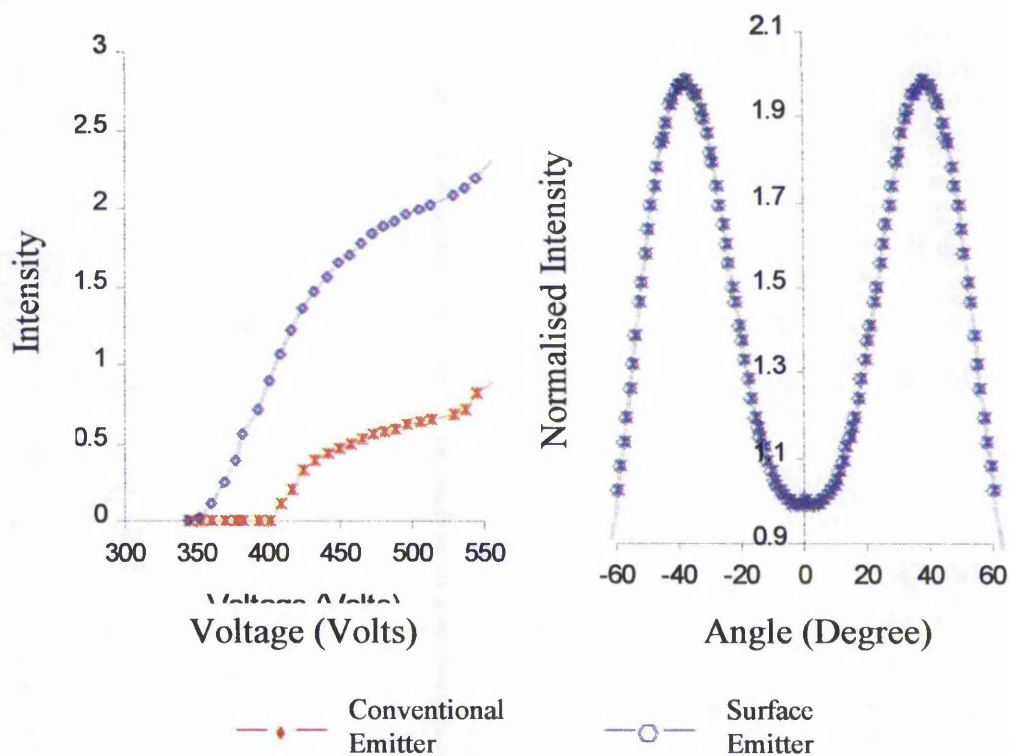


Figure 6.9 Light output characteristics of surface emitting edge emitter LETFEL devices a) Experimental LV Characteristic b) Experimental angular distribution

Surface emitting edge emitter LETFEL devices provide the capability to orient the maximum of emission direction by adequate selection of the microstructure geometry. Particularly, a Gaussian distribution centered along the direction perpendicular to the device surface would optimise the coupling efficiency for HMD and EP applications. This is proposed as future work and is expected to be achieved by substituting the 45° wall sided triangular cross section microstructures with vertical cross sections.

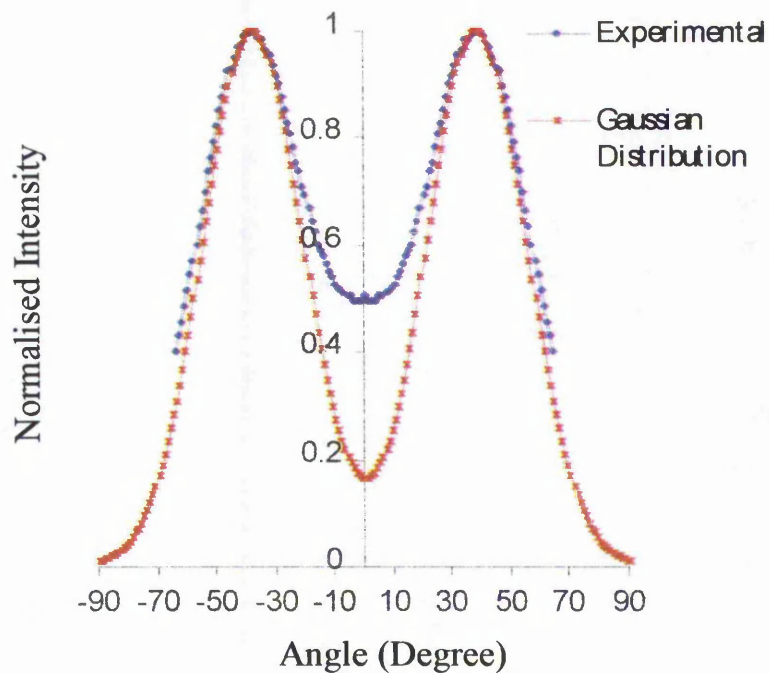


Figure 6.10 Comparison of the angular distribution experimentally measured from surface emitting edge emitters and the theoretical results obtained for an abrupt open end in Chapter 3

Numerical integration of the experimental angular distribution has been performed which demonstrates an enhancement by a $\times 3$ of the total outcoupling efficiency of the surface emitting edge emitter compared with the conventional non etched structure.

As before, numerical integration of the experimental angular profile provides the ratio, τ_{α} , within a particular angle, α , so that $\tau_{\text{HMD}} = 41\%$ and $\tau_{\text{EP}} = 7\%$. As a result, the amount of light redistributed within the acceptance angle of HMDs and EP has not been enhanced in comparison with the conventional non-etched device. This is due to the 45° microstructure wall side utilised for the present experiments.

The incorporation of a 90° microstructure was incorporated, enhancement of the the coupling efficiency for HMDs and EP is expected to reach 93% and 30% of the emitted light. Fabrication of these structures is currently being investigated.

6.5 CONCLUSIONS: COMPARISON OF THE LIGHT OUTPUT PROPERTIES OF THE FABRICATED DEVICES

The choice of the outcoupling mechanism to be used clearly depends upon the coupling efficiency required. The conventional non-etched LETFEL device has shown theoretical coupling efficiencies of 40 % and 7 % of the emitted light for HMD and EP applications respectively. Additionally, the outcoupling efficiency according to the theoretical calculations presented in Chapter 3 was demonstrated to be approximately 4% of the light reaching the device apertures.

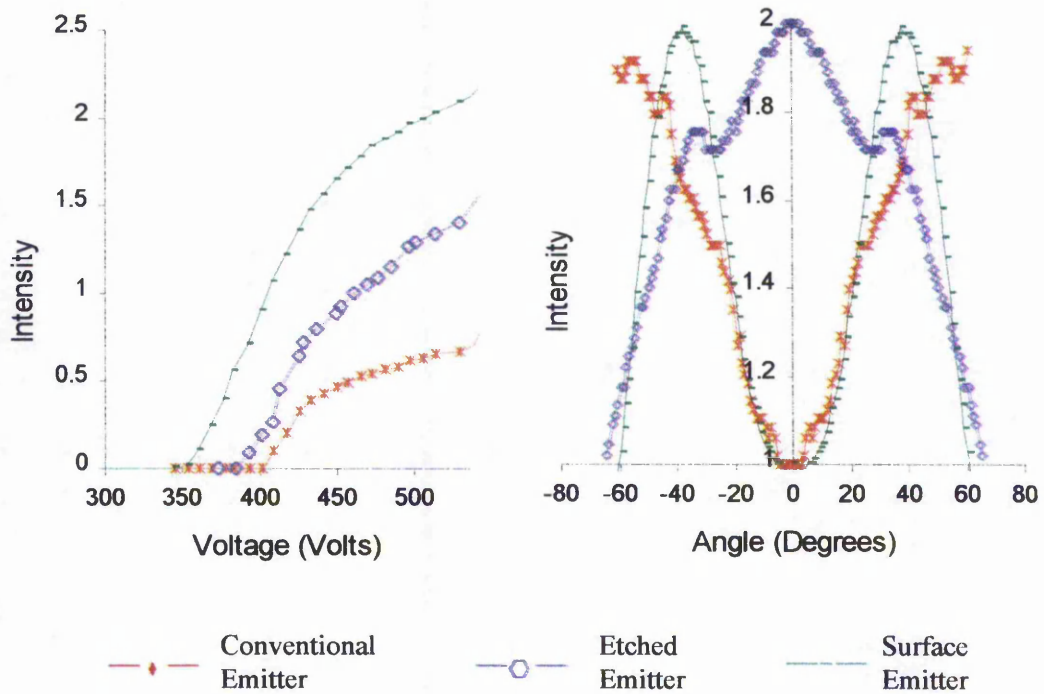


Figure 6.10 Light output characteristics of conventional non-etched, etched and surface emitting edge emitter LETFEL devices a) LV b) Angular Distribution

As previously shown in this chapter, the etched and surface emitting edge emitter LETFEL devices have improved the outcoupling efficiency in a factor of 2.1 and 4.16 when compared with conventional non-etched LETFEL devices. This is evident in Figure 6.10 a which illustrates a comparison of the LV characteristics.

Apart from the enhancement in outcoupling efficiency, an improvement of the angular distribution has also been achieved with the used of the etched emitter as illustrated in Figure 6.10 b. This leads to an increase of 12% and 5% of the coupling efficiency for HMDs and EP respectively. Contrary to this result, the 45° surface emitter has not shown enhancement of the coupling efficiency. This is due to the similarity between the surface emitter and the conventional angular profiles, as illustrated in Figure 6.10 b. However, the surface emitter angular profile has demonstrated agreement with the theoretical profiles emitted through an abrupt open end presented in Chapter 3.

Finally, 90° surface emitters are currently being developed and are proposed to enhance the coupling efficiency into HMDs and EP up to 93% and 30% respectively of the emitted light. Table 6.1 summarises data on the coupling power related to the various measured and predicted angular distributions.

	Conventional Non-Etched	Etched Aperture	Surface Emitting Edge Emitter at 45°	Surface Emitting Edge Emitter at 90°
HMD (<30°)	~42%	~52%	~42%	~93%
EP (<6°)	~7%	~12%	~7%	~30%

Table 6.1 Coupling efficiency into HMDs and EP applications expected for the angular distributions measured from various outcoupling mechanisms

CONCLUSIONS AND FUTURE WORK

-
- 7.1 Introduction
 - 7.2 Achievements
 - 7.3 Future Work
-

7.1 INTRODUCTION

The main aim of this research was to investigate the optical outcoupling mechanism of LETFEL devices. Specifically, the design and manufacture of a novel mechanism which enhances the outcoupling efficiency and provides narrow angular profiles was required. LETFEL devices are intended to be used as light sources for head mounted displays and electrophotographic printing. Both HMD and EP provide small acceptance angles, $<30^\circ$ and $<6^\circ$ respectively, which leads to the requirement of narrow angular profiles. During this work, theoretical modelling as well as experimental work was performed leading to the understanding of the outcoupling process in LETFEL devices.

7.1.1 Theoretical Modelling of the Outcoupling Mechanism

Theoretical modelling of the character of the transmission of light within the LETFEL device was performed following a two step process:

1. Modal propagation theory was applied to the LETFEL device
2. A study of the effect of surface roughness on the propagation was undertaken to determine the radiation losses during transmission.

Comparison of the radiation losses obtained from theoretical results with previously published experimental led to a significant conclusion: the internally generated light couples principally to the fundamental mode and travels as such with low attenuation along the waveguide.

From this result the optical outcoupling mechanism of conventional non-etched LETFEL devices was theoretically analysed. This study was performed assuming that light outcoupling is a result of energy transfer from guided to radiation modes due to the surface roughness and waveguide bend at the aperture regions. The light coupled into radiation modes has been considered to be lost to the outside of the waveguide and therefore to contribute to the outcoupled light. This study demonstrated low outcoupling efficiencies within the range of 4% of the internally generated light. Additionally, broad angular profiles were experimentally measured. As a result, it can be concluded that the light output properties of conventional non-etched LETFEL devices can be improved with the incorporation of a novel outcoupling mechanism.

Two alternative outcoupling mechanisms were proposed, the etched aperture and the surface emitting edge emitter. These can be classified as abrupt open end outcouplers since both incorporate an abrupt open end launching the guided light to the outside.

A model of the outcoupling process through an abrupt open end has been accomplished. This study provided a Gaussian angular divergence with a characteristic width of 24° .

7.1.2 Fabrication of the Novel Outcoupling Mechanisms

Fabrication of the two novel mechanisms was performed. This required the definition of a new fabrication route for LETFEL devices which differs from the traditional route in an additional process responsible for the etch of the aperture. Etching was performed using ion milling, a sputter etch technique which utilises a collimated beam as the sputter source. Prior to fabrication of complete devices, a study of the milling characteristics of the LETFEL thin films was performed. This provided etch-rate values and the effect of the milling angle of incidence on the etched walls of ZnS:Mn. Subsequently, ion milling was applied to the LETFEL device which led to the aperture shapes required.

The output properties obtained from the fabricated devices were measured, including the light intensity versus voltage characteristic and the angular distribution. The angular measurement system was designed and calibrated as part of this work. Identical test features were utilised to allow comparison of the results. Both, the etched aperture and the surface emitting edge emitter have demonstrated enhancement of the outcoupling efficiency in a factor of $2.1 \times$ and $4.16 \times$ respectively, as well as reduction of the angular profile.

To conclude this thesis, there follows a discussion of the achievements and the possible improvements in the outcoupling mechanism in LETFEL devices.

7.2 ACHIEVEMENTS

The achievements of this work can be summarised as below:

1. Theoretical determination of light transmission in LETFEL waveguides
2. Modelling of the light outcoupling in LETFEL devices
3. Characterisation of the ion milling properties of LETFEL thin films
4. Proposition of an optimised route for the fabrication of etched LETFEL devices
5. Fabrication of LETFEL devices incorporating etched apertures and surface emitting edge emitters
6. Evaluation of the output properties of etched LETFEL devices
7. Comparison of the theoretical and experimental results

1. Theoretical determination of the transmission in LETFEL waveguides

Maxwell equations have been solved for the particular boundary conditions of the LETFEL waveguide. Four guided modes have been determined to propagate within the structure. The attenuation undertaken from each guided mode due to conversion into radiation modes as a result of surface roughness was additionally calculated. The attenuation coefficients of the fundamental mode is $\alpha=0.0039\text{dB}\mu\text{m}^{-1}$ which fits the attenuation coefficient experimentally determined in previous research, $\alpha^{\text{exp}}=0.004\text{dB}\mu\text{m}^{-1}$. Furthermore, the attenuation coefficients associated to the higher order modes are, $\alpha_1=0.0555\text{dB}\mu\text{m}^{-1}$, $\alpha_2=0.0649\text{dB}\mu\text{m}^{-1}$ and $\alpha_3=0.1477\text{dB}\mu\text{m}^{-1}$, for the modes 1, 2 and 3 respectively. These are significantly higher than the attenuation undertaken by the fundamental mode. As the light internally generated is assumed to couple into the four radiation modes with diverse coupling efficiencies amplitudes, the experimental attenuation coefficient is expected to be a combination of the attenuation coefficients theoretically determined. Since the experimental attenuation coefficient fits the fundamental mode attenuation coefficient it can be concluded that the internally generated light couples principally into the fundamental mode and propagates as such along the waveguide.

2. Modelling of the light outcoupling in LETFEL devices

The outcoupling efficiency of conventional non-etched LETFEL devices has been theoretically calculated from modal theory. Scattering due to surface roughness and waveguide bends have been assumed to be responsible for the outcoupling mechanisms in this type of devices. Assuming that the internally generated light couples into the fundamental mode, the scattering and bend radiation losses at the device aperture were calculated. According to these results, only 4% of the light reaching the apertures is emitted out of the device. To enhance the outcoupling efficiency of LETFEL devices two alternative mechanisms were proposed, the etched aperture and the surface emitting edge emitter. Both incorporate open abrupt ends which outcouple the waveguided light to the outside. However, the conversion mechanism from lateral to top surface emission differs. The former utilises the reflection of a micromirror structure while the latter curved the LETFEL waveguide before light has been outcoupled. From theoretical modelling, narrow gaussian profiles with a characteristic width of 24° were determined.

3. Characterisation of the ion milling properties of LETFEL thin films

A study of the ion milling properties of LETFEL devices and associated materials has been undertaken. The ion milling characteristics of ZnS:Mn, Y_2O_3 , Si_3N_4 , SiO_2 , SiO_xN_y and Al versus various process conditions were identified, since all of these materials are present in LETFEL devices. Ion milling has been experimentally demonstrated to be a successful technique to shape the LETFEL device aperture. Ion milling rates have been observed to vary with the ion beam angle of incidence for all the studied materials. Particularly a maximum rate is shown for intermediate angles. It has also been observed that different ion beam angles generate different ZnS:Mn profiles. Simulations support that these profiles depend on the ion milling rate of the masking material as well as on the masking shadow effect. Etch-rates have been calculated for two different beam currents; a drop in the etch-rate occurs for the lowest Ar^+ flux and the etch-rate maximum are the same for all the material. Additionally, the ion milling rates have been found to be constant with respect to the etching time.

4. Proposition of an optimised route for the fabrication of etched LETFEL devices

The etched structure requires removal of the LETFEL materials at the outcoupling aperture. As a result, new fabrication steps have been introduced in the detailed route. A thin film of SiO₂ is grown onto the conventional LETFEL film stack with non-etched electrodes. The structure is subsequently coated using photoresist and aligned to the micromirror structures deposited onto the Si substrate. Both the SiO₂ mask and the triple layer electrodes are etched by RIE in order to open the apertures at the micromirror positions. The remaining photoresist is subsequently stripped in calibrated O₂ plasma. The samples are finally ion milled using the SiO₂ film as a sacrificial mask.

5. Fabrication of LETFEL devices incorporating etched apertures and surface emitting edge emitters

The process parameters utilised in the fabrication of etched LETFEL devices have been determined and the optimised ion milling parameters were obtained as follows: 60 minutes, 500 V, 0.5 mA cm⁻², and 2.4·10⁻⁴ Torr and an Ar⁺ beam angle of incidence of 20°. Etched apertures require large aperture widths of the order of ~10 µm however, surface emitting edge emitters were found to be advantageous with aperture widths < 2 µm. SEM illustrations of the device aperture for both etched apertures and surface emitting edge emitters are provided which demonstrate the success of the fabrication route.

6. Evaluation of the output properties of etched LETFEL devices

Etched LETFEL devices have demonstrated to improve the device light output characteristics. A 4.1× enhancement in the surface emitting edge emitter total outcoupling efficiency has been measured when compared with the conventional non-etched technique. The angular profile provides a Gaussian distribution emitted at an angle which depends on the underlying microstructure wall angle. This is a more adequate profile when compared with the conventional non-etched angular properties, for HMDs and EP. Broader angular distributions and lower enhancement of the outcoupling efficiency has been observed from the etched apertures. This is proposed to

be due to transmission losses within the SiO₂ microstructures and potential blocking of the emitted light by the aperture walls.

7. Comparison of the theoretical and experimental results

The theoretical results of the angular profile of an abrupt open end with the experimental data have been found to be in close agreement. This supports the assumption of the coupling of the generated light into the fundamental mode.

7.3 FUTURE WORK

The investigation presented in this thesis is part of the research project into LETFEL devices developed at The Nottingham Trent University, with the specific aim of enhancement of the device brightness for HMD and EP applications. The future work proposed for further improvement of the LETFEL device output properties is:

1. The development of vertical microstructures for surface emitting edge emitters.
2. The incorporation of a planar microlens array onto the device surface. Narrowing of the angular profile is expected if an adequate focal length and distance from the source is selected.

7.3.1 Development of Vertical Microstructures

The fabrication of vertical surface emitting etched emitters requires the fabrication of microstructures with vertical walls. The development of vertical walls is limited by the photoresist side wall angle which is usually lower than 90°. As a result, the process might require the use of very thin (~3000Å) metal sacrificial masks with vertical angles and very high process powers which direct the plasma ions perpendicular to the film surface.

7.3.2 Development of Microlens Array

The incorporation of microlens arrays on LETFEL structures is expected to further reduce the angular divergence of LETFEL devices. The incorporation of these structures requires investigation which involves the following processes:

1. Modelling of the microlens features: Calculation of the focal lengths originated for different microlens heights and base diameters
2. Design of a microlens mask: The design of a mask which leads to the fabrication of a surface emitting edge emitter LETFEL device and to the deposition of overlying photolithographic lenses
3. Callibration of the microlens fabrication process: Callibration of the microlens fabrication process on glass and on a LETFEL device using the designed mask Testing of the light output properties including brightness versus voltage characteristics and angular distributions
4. Comparison of the light output emitted from devices with and without microlenses will provide the effect of the microlens array on the light output properties of LETFEL devices

The design of the microlens mask has been succesfully accomplished. Also the fabrication of microlenses on glass substrates with various heights and diameters has been performed.

REFERENCES

- 1 F Braun, *Wied. Ann., Vol. 60, 1897*
- 2 I Ohta et al., "Electronic Display Devices", *Wiley, 1990*
- 3 A Silzars, "The New Displays: Technologies, Markets, Applications", *SPIE SC06, 2000*
- 4 L Oxawa, "Cathodoluminescence, Theory and Applications", *VCH, Weinheim, 1990*
- 5 M Kykta, "Phosphor Requirements for FEDs and CRTs", *Information Display, Official Monthly Publication of the Society for Information Display, Vol. 15, No. 11, pp. 24-27, November 1999*
- 6 T Saito, "A Study of the Virtual Screen Image of Flat-Faced CRTs", *Journal of the SID, Vol. 7, No. 3, pp. 177-182, 1999*
- 7 P R Wilshaw and M Huang, "An Overview of Field Emission Display Technology", *Proceedings of the EID, 1997*
- 8 R A Tuck et al., "Printable Field Emitting Materials for Large-Area, Low-Cost Field Emission Displays", *Proceedings of the EID, 1997*
- 9 G Hopple and C Curtin, "FED Life and Reliability", *Information Display, Official Monthly Publication of the SID, , Vol. 16, No. 4/5, pp. 34-37, April 2000*
- 10 L F Weber, "The Promise of Plasma Displays for HDTV", *Proceedings of the SID, Vol. 31, pp. 402-405, 2000*
- 11 T J Nelson and J R Wullert, "Electronic Information Display Technologies", *World Scientific, 1997*
- 12 P J Dean et al., "Electroluminescence", *Springer-Verlag, New York, 1977*
- 13 S Bhaskaran et al., "An Investigation of Electron Ejection Mechanism at the Insulator-Phosphor Interface in ZnS:Mn ACTFEL Devices", *Proceedings of the SID, pp. 133-136, 1994*
- 14 W E Howard, "Thin Film Electroluminescent Displays", *J. of Lum., Vol. 24/25, pp. 832-842, 1981*

- 15 K Ohmi et al., "Improvement in Aging Characteristics by Zn Doping of Electron-Beam Evaporated SrS:Ce Thin Film Electroluminescent Devices", *Jpn.J. Appl. Phys.*, Vol. 36, pp. L33-L36, 1997
- 16 H Yoshida et al., "Fast-Switching LCD with Multi-domain Vertical Alignment Driven by an Oblique Electric Field", *Proceedings of the SID*, Vol.31., pp.334-337, 2000
- 17 A V Dotsenko et al., "Phosphor Handbook", *CRC Press*, 1998
- 18 C Chinnock, "If Microdisplays are the Answer, What is the Question?", *Information Display, Official Monthly Publication of the SID*, Vol. 15, No. 7, pp. 10-14, July 1999
- 19 F J Kahn, "Projection Display Technologies for the New Millenium", *Proceedings of the SPIE*, 2000
- 20 C Behlmer, "Electronic Cinema is Inevitable", *Information Display, Official Monthly Publication of the Society for Information Display*, Vol. 15, No. 2, pp 18-20, 1999
- 21 S S Grigsby and B H Tsou, "Visual Processing and Partial Overlap Head Mounted Displays", *Journal of the SID*, Vol. 2, No. 2, pp. 69-73, 1994
- 22 T Holzel, "Are Head-Mounted Displays Going Anywhere?", *Information Display, Official Monthly Publication of the SID*, Vol. 15, No. 10, pp. 16-18, October 1999
- 23 C N King, "Active Matrix EL Displays for HMD Applications", *IEEE International Conference on Consumer Electronics*, pp. 264-265, June 1996
- 24 L Arbuthnot et al., "0.7-inch 1280x1024 Active Matrix Electroluminescent Display using a 12 μm Pixel Structure", *Proceedings of the SPIE Conference on Helmet and Head Mounted Displays III*, Vol. 3362, pp. 326-333, 1998
- 25 M Aguilera and B Aitchison, "Fabricating High Resolution AMEL Flat Panel Displays", *Sol. Stat. Technol.*, pp. 109-113, November 1996
- 26 L B Schein, "Electro-Photography and Development Physcis", *Laplacian Press*, 1992
- 27 S Galan Perez, "Tecnologia de Impresion LED", *Dealer World*, pp 199-208, July/August 1996
- 28 G Destriau, " Recherches sur les Scintillations des Sulfures de Zinc aux Rayons α ", *J. Chem. Phys.*, Vol. 33, No. 587, 1936
- 29 D Khang, *Appl. Phys. Lett.*, Vol. 13, No. 210, 1968

- 30 T Inoguchi et al., "Stable High-Brightness Thin Film Electroluminescent Panels", *Proceedings of the SID*, pp. 84-85, 1974
- 31 R Mach and G O Muller, "Physical Concepts of High-Field, Thin Film Electroluminescent Devices", *Phys.Stat. Sol. (a)*, Vol. 69, No 11, 1982
- 32 R Mach and G O Mueller, "Physics and Technology of Thin Film Electroluminescent Displays", *Semicond. Sci. Technol.*, Vol.6, pp 305-323, 1990
- 33 P Bailey et al., "Trailing Edge Light Emission from ZnS:Mn and ZnS:Tb, F III in a Thick Dielectric Electroluminescent Display", *J. Appl. Phys.*, Vol.81, No.2, pp. 931-936, 1997
- 34 R H Horng et al., "An Electroluminescent Device Using Multi-Barrier Y_2O_3 Layers Incorporated in ZnS:Mn Phosphor Layer", *Mater. Chem. and Phys.*, Vol. 51, pp. 11-14, 1997
- 35 D H Smith, "Modelling AC Thin Film Electroluminescent Devices", *J. Lumin.*, Vol. 23, pp. 209-235, 1981
- 36 P M Alt et al., "Experimental Results on the Stability of AC Thin Film Electroluminescent Devices", *J. Appl. Phys.*, Vol. 53, No. 7, pp. 5186-5199, 1982
- 37 Y A Ono, "Electroluminescent Displays", *World Scientific*, 1993
- 38 G O Muller, "Basics of Electron-Impact-Excited Luminescence Devices", *Phys. Stat. Sol. (a)*, Vol. 81, pp. 597-608, 1984
- 39 A Onton and V Marelo, "Advances in Image Pickup and Display, Vol.5, No137, p 160, 1982
- 40 R Tornqvist, "Manganese Concentration Dependent Saturation in ZnS:Mn Thin Film Electroluminescent Devices", *J. Appl. Phys. Vol. 54, No. 7, pp. 4110-4117, 1983*
- 41 R Mach et al., "Efficiency of ZnS:Mn Electroluminescent Devices", *Proceedings of the 5th International Workshop on Electroluminescence*, pp. 161-169, 1990
- 42 G O Muller, "On the Efficiency of Thin Film Electroluminescent Devices", *Phys. Stat. Sol. (a)*, Vol. 139, pp. 263-269, 1993
- 43 K.K. Zoltan, D. Leksell, P.R. Malmberg, "TFEL edge emitter array for optical image applications", *Proceedings of the SID*, pp. 270-272, 1986
- 44 I P Mc Clean et al., "Analysis of ZnS:Mn ACTFEL Devices Exhibiting Memory Through Donor Centre Capture and Emission Processes", *Proceedings of the SID*, Vol. 24, pp. 885-858, 1993

- 45 C B Thomas and W M Cranton, "High Efficiency ZnS:Mn AC Thin Film Electroluminescent Device Structure", *Appl. Phys. Lett.*, Vol. 63, pp.1-3, 1993
- 46 R Stevens et al., "Enhancing the Brightness of Thin Film Electroluminescent Displays by Improving the Emission Process", *Electr. Dev. Lett.*, Vol. 15, No. 3, pp. 97-99, 1994
- 47 " Guiding Light in Electroluminescent Devices", UK Patent Application GB, 2 296 378, A, 1996
- 48 W M Cranton et al., "Improving the Efficiency of Thin Film Electroluminescent Displays", *Proceedings of the IEE Display Technology Conference*, pp. 7/1-7/6, 1995
- 49 M Born, "Principles of Optics", *Pergamon Press*, 1980
- 50 D Marcuse, "Theory of Dielectric Optical Waveguides", *Academic Press*, 1991
- 51 D Marcuse, "Mode Conversion Caused by Surface Imperfections of a Dielectric Slab Waveguide", *The Bell Syst. Techn. J.*, Vol 48, pp. 3187-3215, 1969
- 52 C R Pollock, "Fundamentals of Optoelectronics", *Irwin*, 1995
- 53 P K Tien, "Light Waves in Thin Films and Integrated Optics", *Appl. Optics*, Vol. 10, No. 11, pp. 2395-2413, 1971
- 54 D Marcuse, "Radiation Losses of Dielectric Waveguides in Terms of the Power Spectrum of the Wall Distortion Function", *The Bell Syst. Techn. J.*, Vol. 48, pp. 3233-3242, 1969
- 55 P Beckmann and A Spizzichino, "The Scattering of Electromagnetic Waves from Rough Surfaces", *Pergamon Press*, 1963
- 56 J A Ogilvy, "Theory of Wave Scattering from Random Rough Surfaces", *Adam Hilger*, 1991
- 57 T Tamir, "Integrated Optics", *Springer-Verlag*, 1975
- 58 E A J Marcatili, "Bends in Optical Dielectric Guides", *The Bell Syst. Techn. J.*, Vol. 48, pp. 2103-2132, 1969
- 59 D Marcuse and R M Derosier, "Mode Conversion Caused by Diameter Changes of a Round Dielectric Waveguide", *The Bell Syst. Techn. J.*, Vol. 48, pp.3217-3232, 1969
- 60 E A J Marcatili and S E Miller, "Improved Relations Describing Directional Control in Electromagnetic Wave Guidance", *The Bell Syst. Techn. J.*, Vol. 48, pp. 2161-2188, 1969

- 61 S E Miller, "Directional Control in Light-Wave Guidance", *The Bell Syst. Techn. J.*, Vol. 43, pp. 1727-1739, 1964
- 62 S E Miller, "Directional Control in Light-Wave Guidance", *The Bell Syst. Techn. J.*, Vol. 43, pp. 1727-1739, 1964
- 63 G Humpsperger, "Integrated Optics Theory and Technology", *Springer-Verlag*, 1985
- 64 C R Pollock, "Fundamentals of Optoelectronics", *Irwin*, 1995
- 65 E Hecht, "Optics", *Alison-Wesley*, 1987
- 66 R Stevens et al, "Etching of AC Thin Film Electroluminescent Devices", *IEEE Transactions on Semiconductor Manufacturing*. Vol. 9, No. 2, pp 241-248, 1996
- 67 W Cranton, "Growth and Characterisation of ZnS:Mn Based Laterally Emitting Thin Film Electroluminescent Device Structures", *PhD Thesis, Bradford University*, 1994
- 68 J L Vossen and W Kern, "Thin Film Processes", *Academic Press*, 1991
- 69 S M Sze, "VLSI Technology", *Mc Graw Hill*, 1988
- 70 W Kern and C A Deckert, "Thin Film Processes", pp. 408
- 71 B A Heath and T M Mayer, "VLSI Electronics: Microstructure Science", *Academic Press*, Vol. 8, Chapter 12, 1984
- 72 H R Kayfman and R S Tobinson, "Operation of Broad-Beam Sources", *Commonwealth Scient. Coop., Alexandra, Virginia*, 1987
- 73 X Xu, "Focused Ion Beam Induced Deposition and Ion Milling as a Function of Angle of Ion Incidence", *J. Vac. Sci. Techn. (B)*, Vol. 10, No. 6, pp. 2675-2680, 1992
- 74 I Takeuchi et al. "Ion Milling Damage and Regrowth of Oxide Substrates Studied by Ion Channeling and Atomic Force Microscopy", *Appl. Phys. Lett.*, Vol. 70, No. 23, pp. 3098-3100, 1997
- 75 R E Lee, "Microfabrication by ion-beam etching", *J. Vac. Sci. Techn.*, Vol. 16, No. 2, pp. 164-170, 1979
- 76 E A Mastio, "The Effects of KrF Pulsed Laser and Thermal Annealing on the Crystallinity and Surface Morphology of Radiofrequency Magnetron Sputtered ZnS:Mn Thin Films Deposited on Silicon", *J. Appl. Phys.*, Vol. 86, No. 5, pp. 2562-2570, 1999